Spring 5-15-2018

Novel Sensing Mechanisms for Chemical and Bio-sensing Using Whispering Gallery Mode Microresonators

He Huang
Washington University in St. Louis

WASHINGTON UNIVERSITY IN ST. LOUIS

School of Engineering and Applied Science

Department of Electrical and Systems Engineering

Dissertation Examination Committee:
Lan Yang, Chair
Shantanu Chakrabartty
Rajan Chakrabarty
Ulugbek Kamilov
Matthew Lew

Novel Sensing Mechanisms for Chemical and Bio-sensing Using Whispering Gallery Mode Microresonators

by

He Huang

A dissertation presented to
The Graduate School
of Washington University in
partial fulfillment of the
requirements for the degree
of Doctor of Philosophy

May 2018
St. Louis, Missouri

Table of Contents

List of Figures

List of Tables

Acknowledgments

Reflecting through these years of study at Washington University in St. Louis, it is impossible to fully express my gratitude to all my friends and coworkers in just a few words. I am here today because of their generous support.

First and foremost, I would like to thank Dr. Lan Yang for her exceptional mentorship. She allowed great freedom for students in choosing their projects, and everyone could pursue what interested him the most. At the same time, a project that one pursues may or may not work as expected, and I am truly grateful for her patience and continued support even when the progress was slow. I will never forget her wisdom and steady guidance. It was my pleasure to work under her mentorship.

I would like to thank all the current and former lab members for their assistance and fruitful discussions: Weijian Chen, Guangming Zhao, Linhua Xu, Xiangyi Xu, Yihang Li, Changqing Wang, Dr. Xuefeng Jiang, Dr. Abraham Qavi, Dr. Sahin Kaya Ozdemir, Dr. Huzeyfe Yilmaz, Dr. Bo Peng, Dr. Faraz Monifi, and Dr. Jiangang Zhu. Special thanks to Guangming and Weijian for their continued friendship ever since I came to St. Louis.

We had many visiting scholars in our lab and I would like to thank them for bringing in fresh ideas. Special thanks to Prof. Fang Bo for collaboration and Prof. Jing Zhang for helpful discussions throughout the years.

Many of my projects were done in collaboration with other research groups, and the works presented in this dissertation would not have been possible without them. I would like to thank Saahil Sheth, Era Jain, and Prof. Sylviya P. Zustiak for their contribution in the hydrogel sensing

project. I would like to thank Alexander Cocking, Corey Janisch, and Prof. Zhiwen Liu for their assistance in building the Raman spectrometer.

Many thanks to my friends here in St. Louis and in Toronto. They made my life much more enjoyable outside the lab.

Finally, I would like to thank my parents. They always motivated me to achieve more and stood by me during my most difficult times. Without their love and support, I could not have been here today.

Steven He Huang

Washington University in St. Louis

May 2018

ABSTRACT OF THE DISSERTATION

Novel Sensing Mechanisms for Chemical and Bio-sensing Using Whispering Gallery Mode Microresonators

by

He Huang

School of Engineering and Applied Science

Department of Electrical and Systems Engineering

Washington University in St. Louis, 2018

Professor Lan Yang, Chair

Due to their ultra-high quality factor and small mode volume, whispering gallery mode (WGM) microresonators have proven to have exceptional sensing capabilities, with single particle level sensitivity to virions, proteins, and nucleic acids. Current sensing mechanisms rely on measuring the changes in the transmission spectrum of the resonator upon adsorption of the analyte on the surface of the resonator, appearing as either shift, splitting, or broadening of the resonance mode, all of which measure the polarizability of adsorbed analytes. In this dissertation, we present two new sensing mechanisms for WGM microresonators: the measurement of a dynamic chemical reaction around the resonator, exemplified by the polymerization of hydrogel, and the Raman spectroscopy of molecules on the surface of WGM microresonator through WGM-based surface-enhanced Raman scattering. Further, an on-going work on sensing using mesoporous silica micro-bottle resonator is described in the last chapter.

Our work on the measurement of gelation of polyacrylamide hydrogel using WGM resonators is the first report of using WGM resonators to continuously monitor a chemical reaction (*i.e.* gelation*) in situ*. The results from WGM sensing is compared with rheology, a well-established

technique for hydrogel characterization. From the similarities and differences in the measured results from WGM and rheology, we suggest that whereas rheology measures the viscoelastic properties of the hydrogel, WGM resonators measure the hydrogel density indirectly through its refractive index. The two techniques provide data that complement each other, which can be used to study the gelation reaction in more details.

Raman spectroscopy is a powerful technique for molecular fingerprinting, but the weak Raman signal often requires enhancement from techniques such as surface-enhanced Raman scattering (SERS). Conventionally, metallic nanostructures are used for SERS, but recently there has been increasing interest in the enhancement of Raman scattering from dielectric substrates due to their improved stability and biocompatibility compared with metallic substrates. The combination of WGM resonator and Raman spectroscopy can be a promising sensing platform with both high sensitivity and specificity. Here, we demonstrate the enhanced Raman scattering from rhodamine 6G molecules coated on silica microspheres, excited through WGMs. A total Raman enhancement factor of 1.4×10^4 is observed.

Chapter 1: Overview

This chapter provides a brief overview of this dissertation. Section 1.1 explains the motivation behind the research described in this dissertation. Section 1.2 is an outline of each subsequent chapter. The introduction to Whispering Gallery Mode (WGM) resonators is provided in Chapter 2.

1.1 Motivation

Whispering gallery mode resonators have been demonstrated as excellent sensors for chemicals and bio-molecules. Starting from the detection of protein adsorption on microsphere resonators,[1] recent demonstrations of detecting single virus,[2] single protein,[3] single nucleic acid,[4] and even single atomic ion[5] using these resonators have stirred much attention in using them for various applications such as environmental monitoring, point-of-care testing, drug screening, as well as basic life science research in protein folding and membrane biophysics.[6] Most of the studies so far focused on decreasing the detection limit for single entities (i.e. particle, protein, ion) by shrinking the mode volume or creating an electromagnetic hotspot using plasmonic nanoparticles. These are, for sure, important questions to be addressed and represent a push for the ultimate detection limit using WGM resonators. However, there are other important questions to be answered as well. For example, how can we make the WGM resonator more sensitive not to single particles but to bulk refractive index changes? How do we eliminate the contribution from environment due to temperature and pressure drift? How do we not only detect the presence of something but also find out what it is that we have detected? The work presented in this dissertation attempts to address some of these questions and explores sensing mechanisms for WGM resonators that are different from those studied so far.

1.2 Chapter Outline

Chapter 2 is a brief introduction to the theory of WGM resonance. Important resonator parameters such as quality factor and mode volume are discussed. Different geometries of WGM resonators are introduced, with focus on microsphere, microtoroid, and micro-bottles. Sensing modalities using these resonators, including mode shift, mode splitting, and mode broadening, are described.

Chapter 3 describes the measurement of hydrogel gelation using micro-bottle WGM resonators. This represents one of the first works in which a dynamic chemical reaction was measured *in situ* using WGM resonators. The measured results from WGM resonance are compared with viscoelastic measurement of the hydrogel using rheology. We have noted that while both WGM resonance and rheology can be used to characterize the gelation of polyacrylamide hydrogel, there is some noted difference in the two, attributed to the different physical parameter that is being measured by the two techniques. This work was done in collaboration with Saahil Sheth, Era Jain, and Prof. Silviya Zustiak from Saint Louis University.

Chapter 4 describes the use of WGM resonator for Raman spectroscopy. Although droplet-based Raman spectroscopy[7] and enhancement of Raman scattering using dielectric microspheres[8] have been studied in the past, this is the first work that considers Raman enhancement in combination with resonators and techniques used for WGM resonator sensors. Specifically, we studied the Raman enhancement for rhodamine 6G molecules coated on the surface of the resonator and identified the Raman enhancement factor to be 1.4×10^4. This enhancement factor was compared with theoretical calculations, with good agreement between the two. This work was done in

collaboration with Corey Janisch, Alexander Cocking, and Prof. Zhiwen Liu from the Pennsylvania State University.

Chapter 5 consists of two parts. The first section describes an on-going work on mesoporous silica micro-bottle resonator for sensing applications. Such resonator is promising for sensing small molecules dissolved in solutions due to the high surface area of the mesoporous silica material. Fabrication and optical characterization of the mesoporous silica WGM resonator, as well as preliminary results on its use in sensing application is presented. In the second part, I conclude this dissertation by presenting my views on the prospects of sensing using WGM resonator in general.

Chapter 2: Whispering Gallery Mode Microresonator

This chapter provides a general introduction to whispering gallery mode (WGM) resonators. Section 2.1 introduces the concept of WGM resonance and parameters used to characterize WGM resonators. The WGM resonator by itself is not useful without optically interacting with its surrounding, and section 2.2 describes the coupling of light in and out of WGM resonators. Section 2.3 describes different geometries of WGM resonators, their unique features and fabrication for each geometry. The focus is placed on microspheres, microtoroids, and micro-bottles, which are used for experiments described in the subsequent chapters in this dissertation. Finally in section 2.4, different sensing modalities of WGM resonators are introduced: mode shift, mode splitting, and mode broadening.

2.1. Whispering Gallery Mode Resonance

Whispering gallery mode resonance, also called morphology-dependent resonance, represents a type of optical resonance in which light is confined in a spherical or circular structure by continuous total internal reflection. The ray optics representation, presented in **Figure 2.1(a)**, gives an intuitive representation of the WGM resonance. Let us consider 2-D WGM resonance, or WGM resonance in an infinite cylinder with refractive index $n>1$ and radius R surrounded by air with $n=1$. In the ray optics description, light is confined within the infinite cylinder by reflecting internally from its boundary along its circumference. Regardless of the wavelength of light, the ray of light eventually reflects back to the starting position. In order to consider resonance effect, we need to use some concepts from wave optics, in that light will have constructive interference when it makes a round trip and adds back to itself with phase shift

equal to integral multiples of 2π. Another way to state this resonance condition is that the round-trip path of light must be an integral multiple of wavelength, or $2\pi n_{eff} R = m\lambda$. Note that here $\lambda = \frac{c}{f}$ denotes the wavelength of light in free space, and $1 < n_{eff} < n$ is the effective refractive index for a WGM. At this "special" resonance condition, we can observe interesting phenomena such as dip (peak) in the transmission (reflection) spectrum, buildup of optical field within the WGM resonator, enhancement of spontaneous emission due to Purcell effect, and various non-linear optical phenomena such as lasing, frequency mixing, and optomechanical oscillation. It is these phenomena that occur on resonance that has motivated researcher to study WGM resonance for more than one hundred years now, starting from the work by Gustav Mie on the light scattering from spherical particles.[9]

Ray optics, however, is in general not an accurate description of wave phenomena such as resonance and only works in providing an intuitive picture of light propagation. For instance, the parameter n_{eff} from the previous paragraph cannot be defined by considering only ray optics, as it is in fact a weighted average of the refractive index of the resonator and its surrounding medium, arising from the presence of optical field outside the resonator. To gain the full picture of WGM resonance, light must be treated as electromagnetic waves and the Maxwell's equations solved for the resonator. This can be done analytically for spheres and cylinders, or through numerical methods for toroids and other structures. Such a solution is presented in **Figure 2.1(b)**. An important observation from this solution of field distribution is the presence of optical field just outside of the resonator, called the evanescent field. **Figure 2.2** further illustrates this by presenting the radial distribution of electric field in a WGM resonator. As it is evident from this figure, a small but significant portion of the optical field, or energy, resides outside the physical boundary of the resonator. This evanescent field is very important for sensing applications, since

it is this field that interact with particles and molecules in the surrounding medium. Another clear observation from **Figure 2.1(b)** is the presence of nodes and anti-nodes in the field distribution. This arises from the eigenmode being represented as a standing wave mode instead of travelling wave mode, the difference between the two becoming important for the discussion of mode-splitting in WGM resonators.

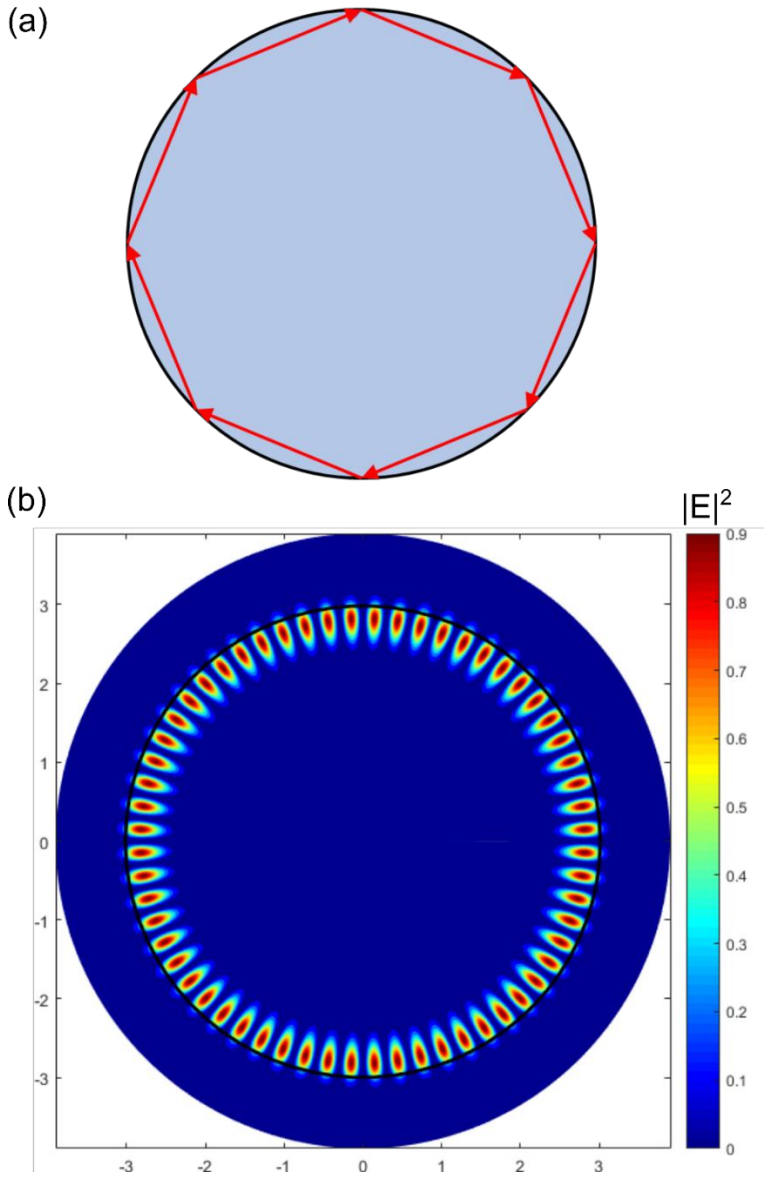

Figure 2.1. Illustration of Whispering Gallery Mode resonance. (a) Ray optics representation. (b) Electromagnetic wave representation. The black circle indicates the physical boundary of the resonator. Note that in this representation the WGM resonance is represented as a light intensity distribution in a standing wave mode instead of a travelling wave mode.

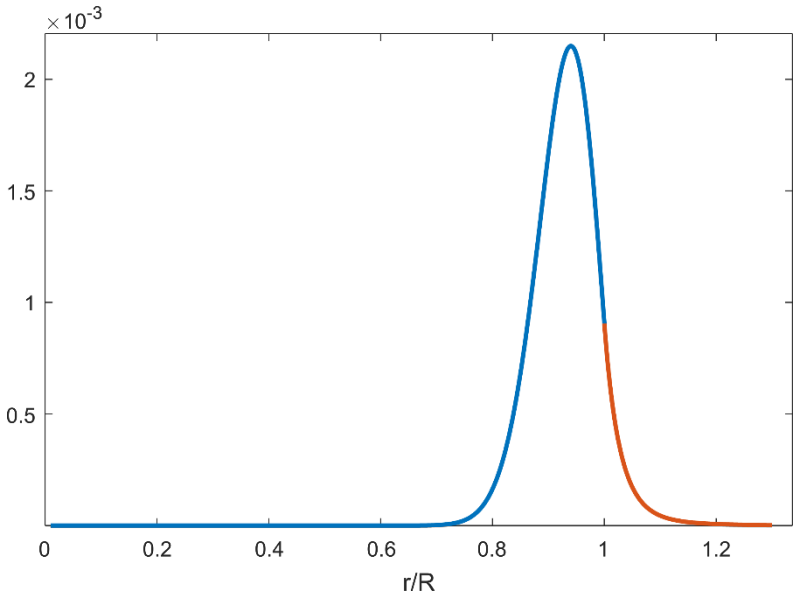

Figure 2.2. Radial distribution of light intensity ($|E|^2$) in a typical WGM resonance. Blue curve indicates the part of the field within the resonator, while red curve indicates the part outside the resonator as evanescent field.

2.1.1. Quality Factor

WGM micro-resonators are excellent sensing devices because of their ability to confine light for a long period of time in a small volume, leading to increased light-matter interaction. The first part of this, related to the loss of the resonator, is characterized by quality (Q) factor. The Q factor is defined as the energy stored in the resonator divided by the energy dissipated per optical cycle, or equivalently as

$$Q = \tau\omega_0 \tag{2.1}$$

where τ is the photo lifetime (or energy damping time constant) and ω_0 is the frequency of oscillating optical field in radians per second. This definition allows for time-domain measurement by observing cavity ring-down. More often, Q factor is measured spectrally, as

$$Q = \frac{\omega_0}{\Delta\omega} = \frac{\lambda_0}{\Delta\lambda} \tag{2.2}$$

where λ_0 is the resonance wavelength and $\Delta\omega$ and $\Delta\lambda$ are the full width at half maximum (FWHM) of the resonance in frequency and wavelength, respectively.

There are several loss mechanisms for a WGM microresonator. The final Q factor of the resonator is determined by

$$Q^{-1} = Q_{rad}^{-1} + Q_{ss}^{-1} + Q_{mat}^{-1} + Q_{ex}^{-1} \tag{2.3}$$

where Q_{rad}^{-1} is the radiation loss due to the curvature of the WGM resonator, Q_{ss}^{-1} is the surface scattering losses from any surface contaminants or inhomogeneities, Q_{mat}^{-1} is the material losses due to absorption or scattering, and Q_{ex}^{-1} is the coupling loss to external waveguide.[10] Out of these losses, $Q_0^{-1} = Q_{rad}^{-1} + Q_{ss}^{-1} + Q_{mat}^{-1}$ is a property intrinsic to the resonator (that is unrelated to the coupling to an external waveguide) and is called the intrinsic Q factor of the resonator. Q_{rad}^{-1} arises since the continuous total internal reflection from resonator is perturbed by the curvature of the resonator. Such loss becomes significant for small resonators with diameter $\frac{D}{\lambda} < 15$, but it vanishes exponentially with increasing resonator size and is insignificant for relatively large resonators.[10] Q_{ss}^{-1} is dependent on the fabrication process and can be decreased by improving the fabrication to decrease surface roughness. Ultimately, the Q factor is limited by Q_{mat}^{-1}. For a silica microsphere operating at 633nm band, Q factor of $Q = 0.8 \pm 0.1 \times 10^{10}$ has been demonstrated, limited by the material absorption.[10]

2.1.2. Mode Volume

The second property of a resonator important for light-matter interaction is its mode volume. Although WGM microresonators have ultrahigh Q factors, achieving such high Q factor is not

very difficult nor as useful if we do not limit the size of the resonant cavity. It is the relatively high Q-factors of WGM microresonator compared to other microresonators of similar sizes that make WGM microresonators useful for many applications. Mode volume is defined as

$$V = \int \frac{\epsilon(\boldsymbol{r})|\boldsymbol{E}(\boldsymbol{r})|^2}{\max(\epsilon(\boldsymbol{r})|\boldsymbol{E}(\boldsymbol{r})|^2)} d\boldsymbol{r}^3 \quad (2.4)$$

The mode volume is essentially an effective volume the mode occupies if the energy density was homogeneous and equal to the maximum energy density of the original mode. Typical mode volume for microsphere and microtoroids are tens to hundreds of μm^3, depending on the size of the resonator. The smaller the mode volume, the more tightly light is confined spatially and the greater the intensity of the confined light. This, in turn, affects cavity parameters such as Purcell factor and threshold of Raman laser. [11,12]

2.2. Coupling to Microresonators

A resonator does not function by itself; light must be coupled to the resonator for it to be functional, and the efficiency of light coupling can be just as important as the properties of the resonators. For a textbook example of Fabry-Perot (FP) cavity, one usually considers one mirror of the FP cavity to be partially transparent and coupling to the FP cavity is performed in free-space through this mirror. However, free-space coupling to WGM resonance is in general very inefficient. According to the coupled mode theory, for efficient coupling of light from one waveguide to another (in this case, the resonator), one needs to have both spatial overlap between the two modes as well as phase matching between the two modes.[13] A free space beam cannot be coupled efficiently since it fails to fulfill the second condition; the effective index of the WGM is always larger than one, while that of a free space beam is equal to one, so phase matching cannot be achieved. For efficient excitation, WGMs must be coupled through the

evanescent field of a dielectric waveguide or a prism, which has effective index larger than one. Common coupler devices include tapered fiber coupler, prism coupler, and angle polished fiber coupler.

2.2.1. Coupling Schemes

The most efficient method of coupling to WGM resonators involve using an adiabatically tapered fiber as a waveguide, and bringing it close to the resonator, as shown in **Figure 2.3(a)**. When a standard single mode fiber is adiabatically thinned to several μm, the waveguide mode in the fiber begins to be air-cladded, with a portion of light leaked out in the surrounding air much like the evanescent field of a WGM resonator. The tapering is typically done by pulling the fiber while heating it with a flame[14] or a CO_2 laser.[15] When the tapered fiber is close enough to the WGM resonator so that the optical modes of the two overlap, the spatial overlap condition is satisfied. Phase matching condition is satisfied by fine-tuning the diameter of the fiber-taper; this changes the propagation constant of the waveguide mode and can be matched to that of the WGM. Fiber-taper couplers are ideal for silica-based WGM resonators since both the fiber and the resonator are made of silica and their refractive indices are very close. In addition, since single-mode fiber is used, fiber-taper couplers offer an ideal single mode to single mode coupling. A coupling ideality of 99.97% has been reported, defined as the ratio of power coupled to the desired mode divided by power coupled or lost to all modes.[16] Although fiber-taper couplers offer ideal coupling, they are very fragile mechanically and the air-cladded fiber-taper is prone to contamination.

Prism coupling involves placing the microsphere on top of a prism and creating a total internal reflection (TIR) spot there using free-space beam as input from below, as shown in **Figure 2.3(b)**. The WGM resonator, typically a microsphere, is brought sufficiently close to the prism so

that evanescent field from TIR at the prism surface overlaps with the evanescent field of the WGM. Phase matching is achieved by changing the angle of the input beam that creates the TIR spot. Since the angle of the input beam can be changed easily with free space optics, this coupler can be easily adjusted for efficient coupling. Prism couplers also have the advantage of being able to excite all microspheres within the beam spot, thus particularly suited for parallel imaging/sensing of multiple microspheres simultaneously. In particular, total internal reflection fluorescence microscope (TIRF-M) essentially behaves as a prism coupler and can be a convenient way to excite WGMs in microspheres placed on a glass coverslip.[17] One problem with the prism coupler is that the output power from the resonators cannot be collected efficiently; although the output power does go into the prism, it is coupled to a large number of modes, not all of which can be collected.[16,18]

Finally, angle polished fiber coupling involves polishing the end of a single-mode fiber at a specific angle, and having the light propagating in the fiber undergo a total internal reflection at this angled fiber end, as shown in **Figure 2.3(c)**.[19,20] The evanescent field of the TIR spot from the fiber end is used to excite the WGMs, and thus this is essentially an optical fiber implementation of the prism coupler. The WGM resonator is placed in proximity to the angled fiber end, so that the TIR evanescent field overlaps with the field from the WGM. Phase matching is achieved through polishing the fiber end at a specific angle, with the requirement $\Phi = \arctan(\frac{n_{resonator}}{n_{fiber}})$, where Φ is the required angle and $n_{resonator}$ and n_{fiber} are the effective indices of the WGM and the propagating mode in the fiber, respectively.[20] Since the angle of the fiber end must be known *a priori* and it cannot be changed during the experiment, this coupling scheme is quite inflexible. However, using optical fiber instead of free space beam for input does

simplify the experiment, and angle polished fiber coupler is a more robust coupler structure compared with the fragile fiber taper coupler.

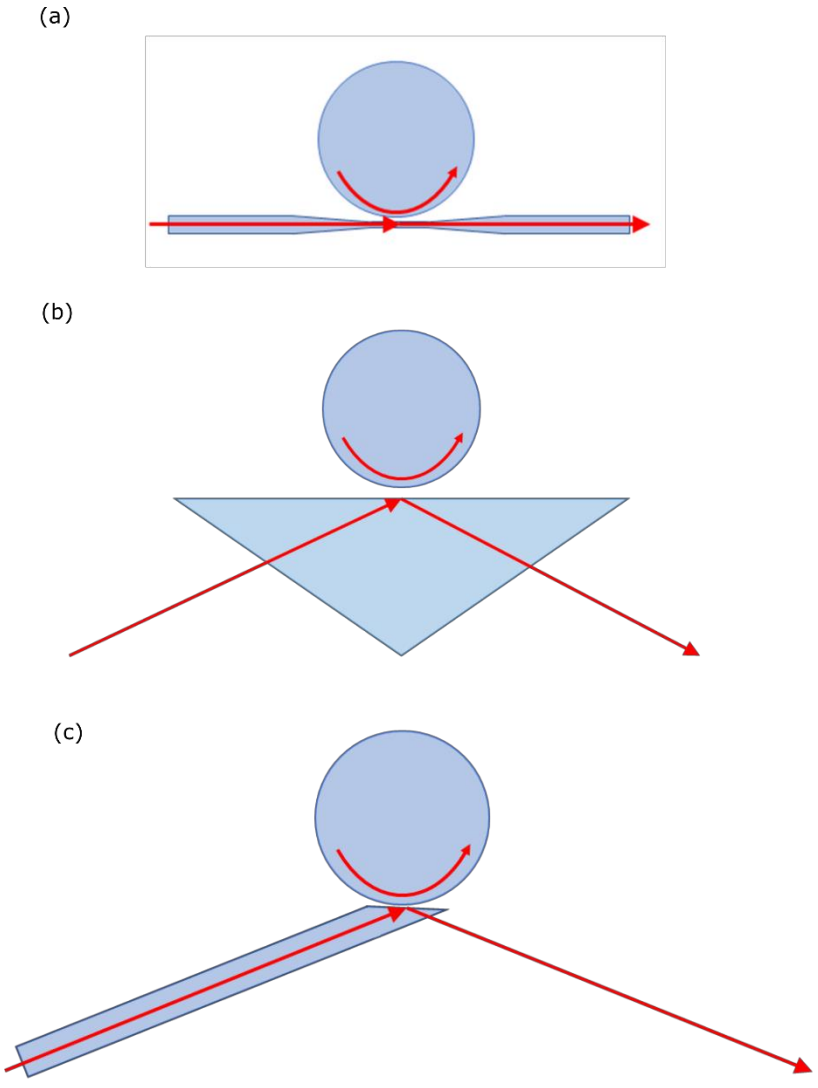

Figure 2.3. Coupling schemes used for WGM resonators. (a) Fiber-taper coupling. (b) Prism coupling. (c) Angle-polished fiber coupling.

2.2.2. Coupling Equation

Let us consider the ideal case of fiber-taper coupling to a microsphere, where one waveguide mode is coupled to one WGM without loss or coupling to any other modes. In this case, the fields involved in the waveguide-resonator system can be represented as in **Figure 2.4**. A_0 is the normalized amplitude of optical field in the WGM resonator, B_{in} is the normalized amplitude of the input light and B_{out} is the normalized amplitude of the output light. Here we use the slowly varying envelope approximation and consider the amplitudes A_0, B_{in}, and B_{out} to vary much slower than the frequency of the optical field. Also, we assume that the Q factor of the resonator is high enough that when off-resonance, $B_{out} \approx B_{in}$. Then, the field inside the cavity can be described as[21]

$$\frac{dA_0}{dt} = -(i\Delta\omega + \delta_0 + \delta_c)A_0 + i\left(\frac{2\delta_c}{\tau_0}\right)^{\frac{1}{2}} B_{in} \tag{2.5}$$

$$B_{out} = B_{in} + i(2\tau_0\delta_0)^{\frac{1}{2}}A_0 \tag{2.6}$$

where $\Delta\omega = \omega - \omega_0$ is the frequency detuning from resonance frequency ω_0, $\delta_0 = \frac{\omega}{2Q_0}$ is the resonator's intrinsic loss, $\delta_c = \frac{\omega}{2Q_c}$ is the coupling loss to the waveguide, and $\tau_0 = \frac{n_s L}{c}$ is the roundtrip time for the mode travelling in the resonator. At steady state, the intensity transmittance through the resonator-coupled waveguide can be expressed as

$$(B_{out})^2 = (B_{in})^2\left(1 - \frac{4\delta_c\delta_0}{(\delta_0+\delta_c)^2+(\Delta\omega)^2}\right) \tag{2.7}$$

Thus spectrally, the WGM resonance appears as a Lorentzian dip with FWHM linewidth of $\delta_{total} = \delta_0 + \delta_c$.

Further, the depth of this resonance dip depends on δ_0 and δ_c. The fractional depth of the resonance dip can be expressed as[21]

$$K = \frac{4Q_0Q_c}{(Q_0+Q_c)^2} \tag{2.8}$$

When $Q_0 = Q_c$, the transmission is zero and this condition is called critical coupling. At critical coupling, all optical power from the input waveguide is coupled into the resonator and is dissipated in the resonator through its intrinsic loss such as radiative loss and material loss. At critical coupling, the intracavity power is also maximized. The zero-detuning, critical coupling intracavity power can be expressed as

$$|A_0|^2 = \frac{1}{2\delta_0\tau_0} \tag{2.9}$$

For a typical microsphere resonator, there is significant power buildup inside the resonator since light is making many round trips before it is lost.

When $Q_0 < Q_c$ the coupling regime is called under coupling, and when $Q_0 > Q_c$, the coupling regime is called over coupling. In practice, typically the resonator's Q_0 is fixed, and Q_c is varied by changing the relative position of the resonator with respect to the fiber-taper. The further away the resonator is from the fiber, the smaller the coupling loss and the greater the Q_c.

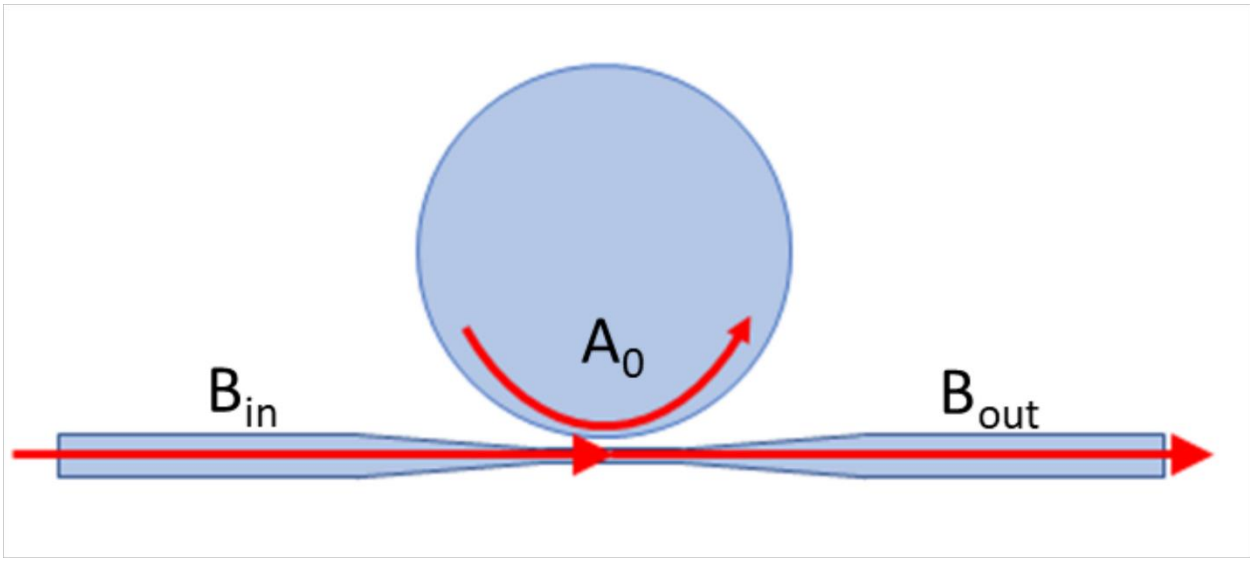

Figure 2.4. Schematic of optical coupling between resonator and waveguide.

2.3. Resonator Geometries

2.3.1. Microsphere

Microspheres are one of the most studied geometries of WGM resonators. They are certainly the ones that were studied the earliest, [22–24] as there is an abundance of spherical, dielectric structures in nature in the form of liquid droplets of aerosol particles. Liquid droplets have extremely smooth surface from surface tension, and this results in a very high Q factor for the WGMs. However, these liquid droplets tend to be rather volatile, prone to deformation, and simply difficult to handle. Much greater interest in research in WGM developed with the introduction of silica microspheres,[25] typically fabricated by melting the end of a silica rod (such as optical fiber) with a CO_2 laser, as shown in **Figure 2.5(a)**. Such reflow process creates a smooth surface from surface tension just like liquid droplets, but with the added advantage of being able to preserve the shape after the resonator cools down. In air, the Q factor of such microsphere can be as high as 0.8×10^{10}.[10] When used for sensing applications in water, however, typical Q factor is

around 10^5 to 10^6. [2,3,1,5] Silica microspheres can also be fabricated on a wafer, using a method similar to the fabrication of microtoroids, to be discussed in the next sub-section. Such microsphere is shown in **Figure 2.5(c)**. On-chip microspheres can be made quite small (to 10 μm diameter), while still maintaining rigid mechanical support in the form of a silicon pillar, which is important for stable coupling to fiber-taper couplers.

Another type of microspheres is unsupported microspheres made of polymers such as polystyrene or glasses such as $BaTiO_3$, shown in **Figure 2.5(b)**. Unlike silica microspheres that are fabricated at the tip of an optical fiber, these microspheres are often fabricated by wet-chemical synthesis in solution,[26,27] and thus are not attached to a stem or a pillar. This method of fabrication can create a very large number of microspheres at once, but the Q-factor tends to be lower than silica microspheres made from fiber tip and is typically limited to about 10^6.[18,28] Also, the handling of the microsphere and its precise positioning for coupling can be cumbersome. Controlled coupling of polystyrene microspheres to a prism coupler has been demonstrated by using optical tweezer [18] or another layer of polymer on the prism, index-matched to water, to act as a spacer layer.[28]

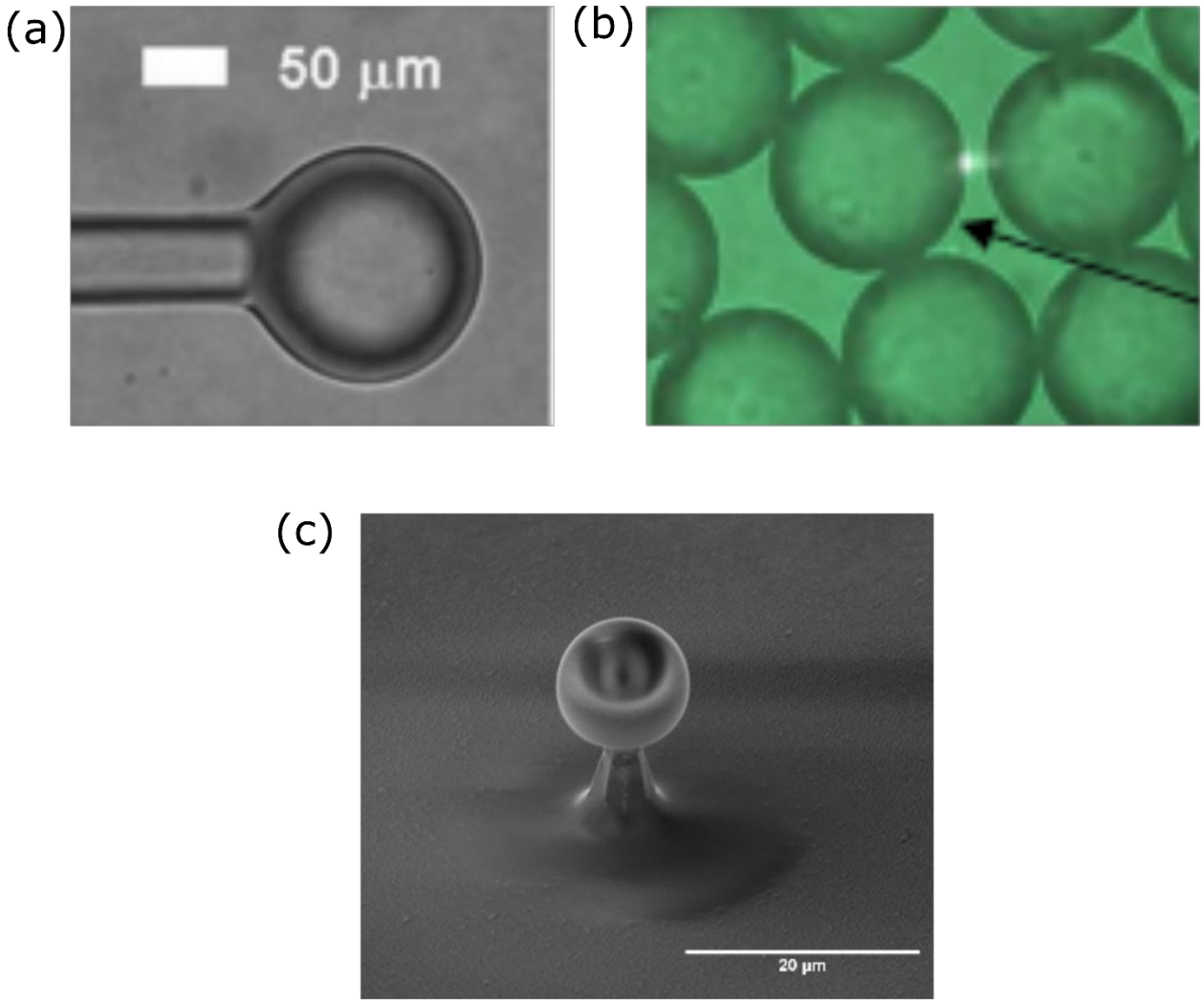

Figure 2.5. Microsphere resonators. (a) Microsphere fabricated at fiber tip. Reprinted from Ref. 2. (b) Polystyrene microspheres in water. Reprinted from Ref. 28. (c) An on-chip microsphere, fabricated with photolithography.

2.3.2. Microtoroid

A microtoroid resonator consists of a silica torus on a silicon pillar fabricated on a silicon wafer, shown in **Figure 2.6**. The fabrication of a microtoroid involves four steps.[29] First, a photo-resist disk is defined on a silicon wafer with thermal oxide using photolithography. Second, this disk

pattern is transferred to the thermal oxide layer using hydrofluoric acid (HF) etching. Third, xenon difluoride (XeF_2) is used for an isotropic, selective etching of silicon. This forms a silica disk on top of a round silicon pillar. Finally, a CO_2 laser is used to heat the silica disk, causing the silica at the edge to melt. Due to surface tension, the silica disk shrinks at the edge, forming a toroidal structure. A microtoroid resonator fabricated this way can achieve Q factor as high as 10^8. [29]

Note that the xenon difluoride etching can be replaced by other silicon etching, such as HNA and KOH.[30] In particular, I have found KOH etching at 45 wt% in water and 60°C to be a convenient alternative to XeF_2 etching. KOH is an anisotropic etch and this results in the pillar having a hexagonal shape. However, after CO_2 laser reflow, KOH etching results in resonators with similar Q-factor to XeF_2 etching, and the KOH etching can be completed much faster.

For silicon pillar supported microspheres fabricated using this method, the silicon pillar is etched until there is only a very small area of contact between the silicon pillar and the silica disk. This suppresses the cooling of the silica disk through the silicon pillar during CO_2 laser reflow. As the result, the entire disk is molten, forming a microsphere on top of the silicon pillar.[30,31] Such microspheres can be made to have smaller diameters compared with that of a toroid, and can be advantageous for applications where a small mode volume is important.

Microtoroids are often compared with microspheres as an alternate geometry for ultra-high Q resonator. Like the microsphere, reflow using CO_2 laser creates a very smooth surface, resulting in the microtoroid having a much higher Q factor than the microdisk before the reflow. Microtoroids, however, have several advantages over stem-supported microspheres. Microtoroids are fabricated on-chip using lithography, and this allows for an easier integration

with other wafer-based technologies and more precise control of device geometry. In particular, in microtoroids, the minor diameter of the torus can be changed independently of the major diameter. This allows for the suppression of many modes that are present in microspheres and is advantageous for applications such as single-mode lasing.[29] In addition, due to the small minor diameter of the torus, optical modes are more tightly confined in a microtoroid compared with a microsphere, resulting in the mode volume of a microtoroid being smaller than a microsphere of equal major diameter by up to a factor of 5.[32]

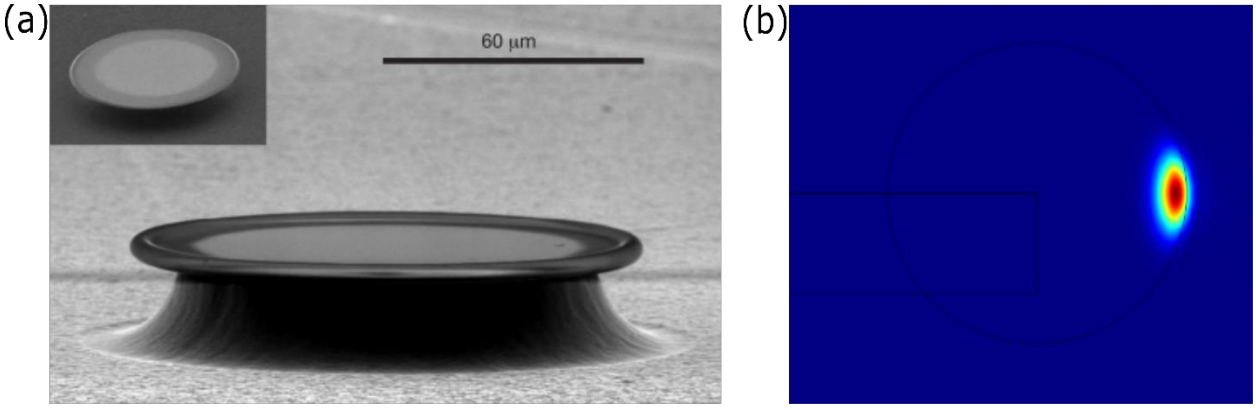

Figure 2.6. Microtoroid resonators. (a) SEM micrograph of a microtoroid. Reprinted from Ref. 29. (b) COMSOL simulation showing the cross-sectional mode distribution of a WGM in microtoroid.

2.3.3. Micro-Bottle

A bottle microresonator is essentially a cylindrical WGM resonator, in which the cylinder diameter varies along the axial direction, as shown in **Figure 2.7**. Typically made from standard optical fiber, it consists of a thick portion of silica fiber sandwiched by two thin portions of silica

fiber.[33–36] Its fabrication involves two steps. First, a section of tapered optical fiber is created by pulling the fiber while heating with flame, filament or CO_2 laser. The diameter of the first tapering determines the diameter of the final bottle resonator. Then, two microtapers are created by further heating two sections of the taper while slightly stretching, forming a bulge in the middle. This second tapering determines the change in the diameter of the resonator in the axial direction.

A bottle microresonator created this way can be considered as a prolate microsphere (and in this sense, a microtoroid is an oblate microsphere). For a bottle microresonator and a microsphere with the same diameter, the bottle microresonator has a smaller curvature in the axial direction. As the result, the optical modes are confined more broadly in the axial direction and this allows the bottle microresonator to support more axial modes. These modes have nodes and antinodes in the axial direction. In particular, the optical field is strong at the two ends known as the caustics, which can be used for sensing application (refer to **Figure 2.7(a)**). The Q factor for a bottle microresonator can exceed 10^8.[35] The free spectral range of a bottle microresonator is typically smaller than other WGM microresonators with similar diameter due to its numerous axial modes. This can be an advantage when tuning the resonance wavelength across a wide range is a challenge.

Bottle resonators can also be created using polymers (such as photoresist) by dispensing a droplet of photoresist onto an optical fiber as shown in **Figure 2.7(b)**.[37] However such resonator tends to have much lower Q factor due to material losses in the polymer ($Q \approx 10^4$).[37]

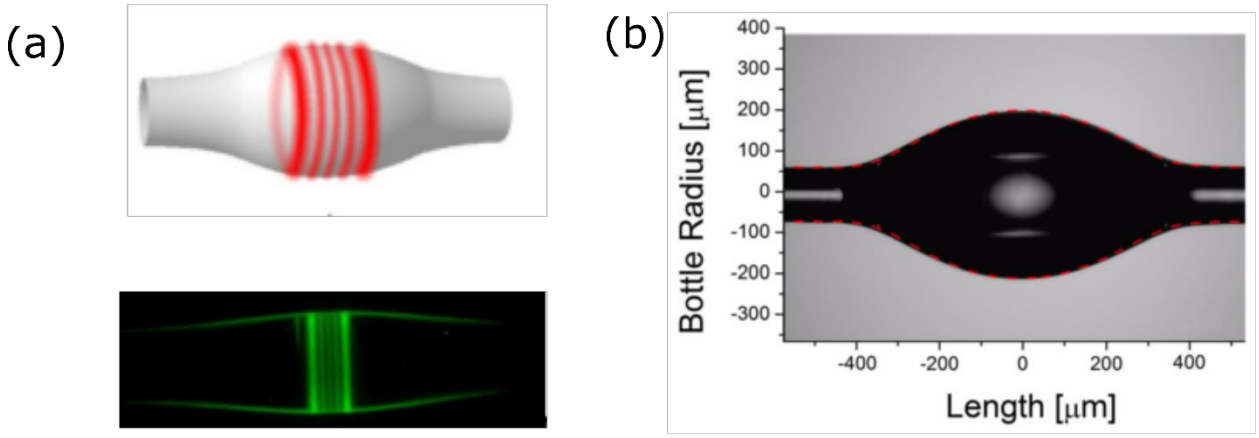

Figure 2.7. Micro-bottle resonators. (a) Top: schematic drawing of a silica micro-bottle resonator made from tapering optical fiber, showing the structure of WGM resonance. Bottom: micrograph of an actual bottle resonator supporting WGM. The green light comes from the fluorescence of doped erbium ions and corresponds to a particular WGM. Reprinted from Ref. 35. (b) Micrograph of an SU-8 bottle resonator. Reprinted from Ref. 37.

2.3.4. Other Geometries

There are many other geometries of WGM microresonator that are interesting, but a full description for all the different geometries are out of the scope of this dissertation, and only a brief description will be provided for the rest.

Microrings, although not mentioned above, are a popular WGM geometry for sensing applications (**Figure 2.8(a)**). These resonators are fabricated together with the coupling waveguide monolithically on the same wafer.[38–40] The use of pre-fabricated waveguide provides much stability for sensing application. In addition, an array of resonator can be easily fabricated, allowing for multiplexed sensing. The Q factors for these resonators, however, are rather low, generally on the order of 10^4.

Micro-capillary[41,42] and micro-bubble resonators[43] represent a type of resonator with hollow center, and only a thin wall of silica is used to support the WGM (**Figure 2.8(b)** and **Figure 2.8(c)**). This allows for the introduction of liquids and gases inside, which can be made to interact with the WGM through its evanescent field. This provides a convenient way of introducing the samples to the resonator, especially since the fiber-taper can be coupled from outside the capillary, not immersed in the solution.

Recently, micro-disk resonators (**Figure 8(d)**) have been receiving increased attentions due to improvement in fabrication techniques.[44–46] Made into wedge shapes, these resonators have Q factor exceeding $Q = 10^8$, comparable with the microtoroid resonators. Due to the lack of reflow, which is rather uncontrolled, the WGMs in these micro-disk resonators can be controlled much better spectrally, allowing for the possibility of dispersion engineering, with applications in frequency-comb generation. These resonators have not been used for sensing applications yet, to the best of my knowledge.

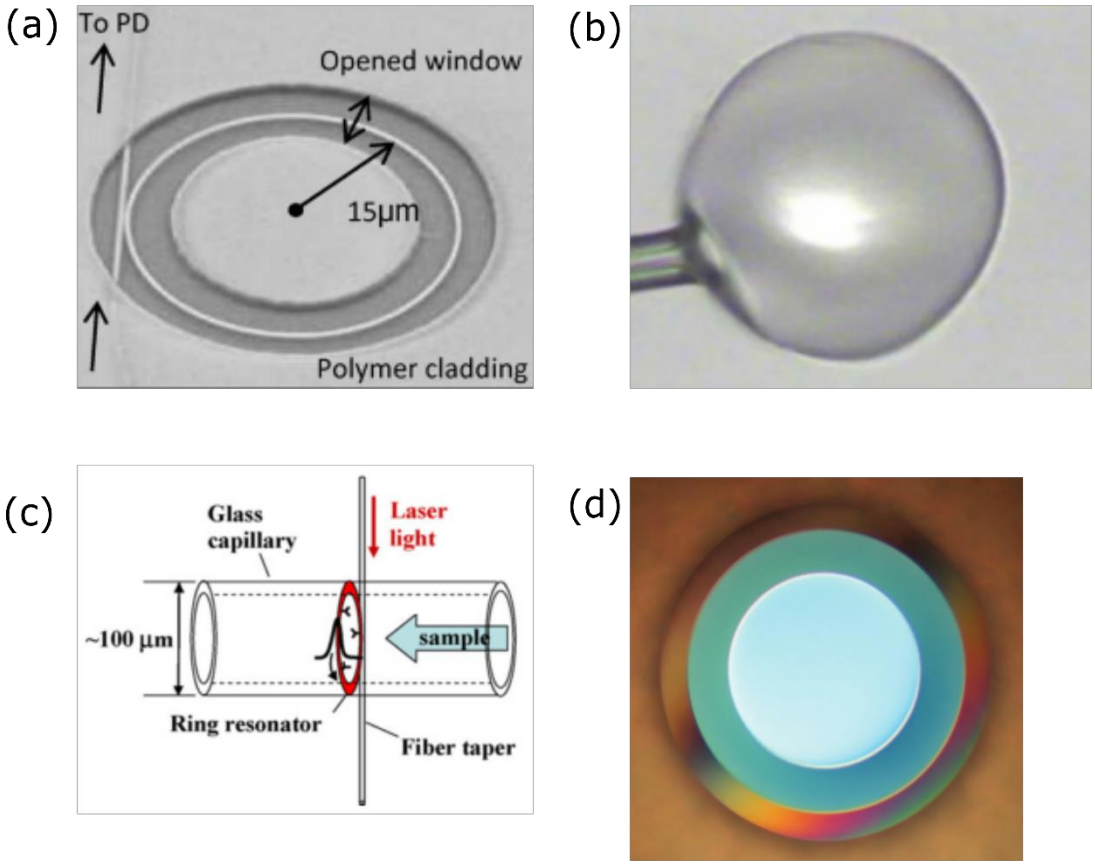

Figure 2.8. Other geometries of WGM resonators. (a) Microring resonator. Reprinted from Ref. 39. (b) 300 μm diameter microbubble resonator. Reprinted from Ref. 43. (c) Capillary resonator. Reprinted from Ref. 42. (d) 1mm diameter microdisk resonator. Reprinted from Ref. 44.

2.4. WGM Resonators in Sensing

Sensing using WGM resonator is typically done by monitoring the transmission through a WGM resonator and observing its change in transmission spectrum as the analyte is introduced to the resonator. The change in the transmission spectrum, in general, can be quite complex due to changes in coupling, contamination of fiber taper, and other noises that are not directly related to the analyte of interest. To simplify data extraction, three sensing modalities have been identified, each corresponding to a different kind of change in the transmission spectrum. These are mode

shift, mode splitting, and mode broadening. The change in the resonance spectrum in each case is presented in **Figure 2.9**. In general, when an analyte is introduced to the resonator, all of these three changes are present in the transmission spectrum. However, the degree of visibility of mode shift, splitting, and broadening depends on the type of analyte (bulk refractive index, single particle, single layer, etc.), the size and Q-factor of the resonator, and the coupling scheme, and each of these sensing modalities has proven to be effective under certain experimental conditions.

2.4.1. Mode Shift

Mode shift is the most commonly used sensing modality, as it is almost always observed. When an analyte of interest adsorbs onto the surface of a resonator, it interacts with the WGM in the resonator, resulting in an increase in its overall effective index and an increase in resonance wavelength. For a point-like distortion such as single molecule and single nanoparticle, the shift in the WGM resonance upon introduction of the analyte can be expressed as:[2,47]

$$\frac{\delta\omega_0}{\omega_0} = \frac{-\alpha_{ex}|\boldsymbol{E}_0(\boldsymbol{r_i})|^2}{2\int \epsilon_r(\boldsymbol{r})|\boldsymbol{E_0}(\boldsymbol{r})|^2 dV} \tag{2.10}$$

where $\frac{\delta\omega_0}{\omega_0}$ is the fractional shift in resonance frequency, α_{ex} is the excess polarizability of the analyte (nanoparticle or protein), $\epsilon_r(\boldsymbol{r})$ is the permittivity of the resonator, and $\boldsymbol{E_0}(\boldsymbol{r})$ is the electric field distribution of a WGM. $\boldsymbol{r_i}$ denotes the position of the analyte molecule/particle. The numerator corresponds to the energy required to polarize the analyte, while the denominator corresponds to the energy in the original resonator. From this expression, we see that the resonance shift depends on field strength at the position of the analyte; the shift is maximized if the analyte is adsorbed at the field maximum on the surface of the resonator. Also, the

denominator is related to the mode volume; the smaller the mode volume, the greater the resonance shift. Using this principle, one method of increasing the resonance shift upon single biomolecule binding is to use the plasmonic hotspot from a hybrid plasmonic-photonic WGM resonator structure. [3–5]

For the adsorption of single particles and single molecules, the resonance shift depends on the position of the molecule. However, if these molecules form a uniform layer on the resonator or result in bulk refractive index change for the medium around the resonator, such position dependence is no longer present. For microspheres, the shift in resonance upon a small bulk refractive index change of the surrounding Δn_m can be approximated as:[48,49]

$$\frac{\Delta k}{k_0} = -S_{pol} \frac{n_m \Delta n_m}{(n_s^2 - n_m^2)^{\frac{3}{2}}} \frac{1}{k_0 R} \tag{2.11}$$

where k_0 is the resonance wavenumber, n_s and n_m are the refractive indices of the microsphere and the medium surrounding the microsphere, respectively. $S_{pol} = 1$ for TE polarization, and $S_{pol} = 2 - \left(\frac{n_m}{n_s}\right)^2$ for TM polarization. Upon the adsorption of a uniform layer with thickness $t \ll \lambda$, the resonance shift can be approximated as:[48,49]

$$\frac{\Delta k}{k_0} = -S_{pol} \frac{2 n_m \Delta n_m}{(n_s^2 - n_m^2)} \frac{t}{R} \tag{2.12}$$

Note that this applies only to small refractive change $\Delta n_m \ll n_s - n_m$. In case where a dense layer is formed with $n_{ads} \approx n_s$, the resonance shift is better characterized by:[10,48]

$$\frac{\Delta k}{k_0} = \frac{\mathrm{t}}{R} \frac{n_s^2 - 1}{n_{ads}^2 - 1} \tag{2.13}$$

For $n_s = n_{ads}$, this expression reduces to $\frac{\Delta k}{k_0} = \frac{t}{R}$.

Although mode shift is a popularly used sensing modality to detect different types of analyte such as bulk refractive index change, monolayer adsorption, and single-particle/single-molecule perturbation, one largest problem with mode shift is its sensitivity to background drift that arises from ambient temperature and pressure changes. One way to separate the signal due to the binding of biomolecules from that due to temperature and pressure drift is to look for step changes due to single-molecule events.[2,4,5] Another method is looking for changes in mode splitting and mode broadening instead of mode shift, as discussed in the following.

2.4.2. Mode Splitting

Mode splitting technique relies on the measurement of scatterer induced coupling between the clockwise and counterclockwise propagating WGM, and works the best for sensing nanoparticles on the order of 10-100 nm. [50] To explain this phenomenon, first note that in an ideal, scatterer-free WGM resonator, resonance modes always come in pairs. These are the clockwise propagating modes and counterclockwise propagating modes. Since these two modes have the same field distribution but just opposite directions, their resonance wavelengths are the same. However, when there is a scatterer on the resonator, a part of the light scattered from the clockwise mode is scattered into the counterclockwise mode and vice versa. This creates a coupling between the two modes. Due to this coupling, the degeneracy between the two modes are lifted; the eigenmodes are no longer described by a pair of traveling modes, but instead by a pair of standing wave modes. In the transmission spectrum, what originally appeared as one Lorentzian dip splits into two. These two modes are characterized by their relative splitting (δ) and their linewidths (γ_1 and γ_2), as shown in **Figure 2.9 (b)**.

When there is a single scatterer on the resonator, the polarizability (α) of this particle can be found from δ, γ_1, and γ_2 as: [50]

$$\alpha = -\frac{3\lambda^2}{8\pi^2}\frac{\Gamma_R}{g} \tag{2.14}$$

$$\Gamma_R = \pi|\gamma_1 - \gamma_2| \tag{2.15}$$

$$g = \pi\delta \tag{2.16}$$

When there are multiple particles, the situation is more complex, but the particle's polarizability can be found by comparing the spectrum before and after the single-particle event[51] or by analyzing the statistics of mode-splitting changes due to many particles.[52] An advantage of the mode-splitting technique over mode shift is its ability to perform self-referenced detection, as the two split modes serve as a reference to each other. As the result, mode-splitting is not influenced by thermal or pressure fluctuation induced changes that are present in mode shift. In addition, the mode-splitting technique allows for the determination of particle size in real time.

A drawback of the mode-splitting technique is its rather limited applicability in areas other than detection and sizing of nanoparticles. Since mode-splitting is a technique based on particle scattering, it is intrinsically insensitive to uniform changes in refractive index, such as those due to the change in the bulk refractive index of the medium surrounding the resonator or the formation of a uniform layer around the resonator. In addition, resolvability of mode-splitting depends on the size and Q-factor of the resonator and can become an issue in aqueous environment, in which the size of the resonator needs to be larger to prevent radiation loss and the Q-factor tends to be lower due to absorption loss in water. Although mode-splitting has been

demonstrated in water for sensing applications,[53,54] the range of resonator size and particle size with which this is possible is more limited than having the resonator in the air.

2.4.3. Mode Broadening

A WGM resonance's linewidth change can be used for the detection of an analyte, and this is often called the mode broadening technique. Losses due to the analyte can be absorption losses and scattering losses. Analyte detection through absorption loss is, of course, limited to only ones that absorb at the probe wavelength, while detection through scattering losses is limited to nanoparticles. Another mechanism that results in apparent mode broadening is from unresolved mode-splitting, which experimentally is indistinguishable from mode broadening.[55] When nanoparticles with no optical absorption are used as the analyte, in the small particle and low Q resonator limit, the mode broadening is dominated by the scattering loss from the nanoparticle and is quadratically related to the particle polarizability. On the other hand, in the limit of large particle and high Q resonator, the mode broadening is dominated by underlying unresolved mode splitting and becomes linearly related to the particle polarizability.[55] Such mode broadening principle has been applied to detect 70 nm radius polystyrene particles and lentivirus particles.[56]

Experimentally, the measurement of mode broadening has a unique challenge in that it requires an extremely stable coupling to the resonator since a fluctuating coupling loss causes fluctuation in the resulting linewidth of the WGM. This makes the popularly used fiber taper coupling unsuitable for mode broadening measurement, and special coupling techniques, such as that based on chaos-assisted-tunneling with an intentionally deformed resonator may be required. [56]

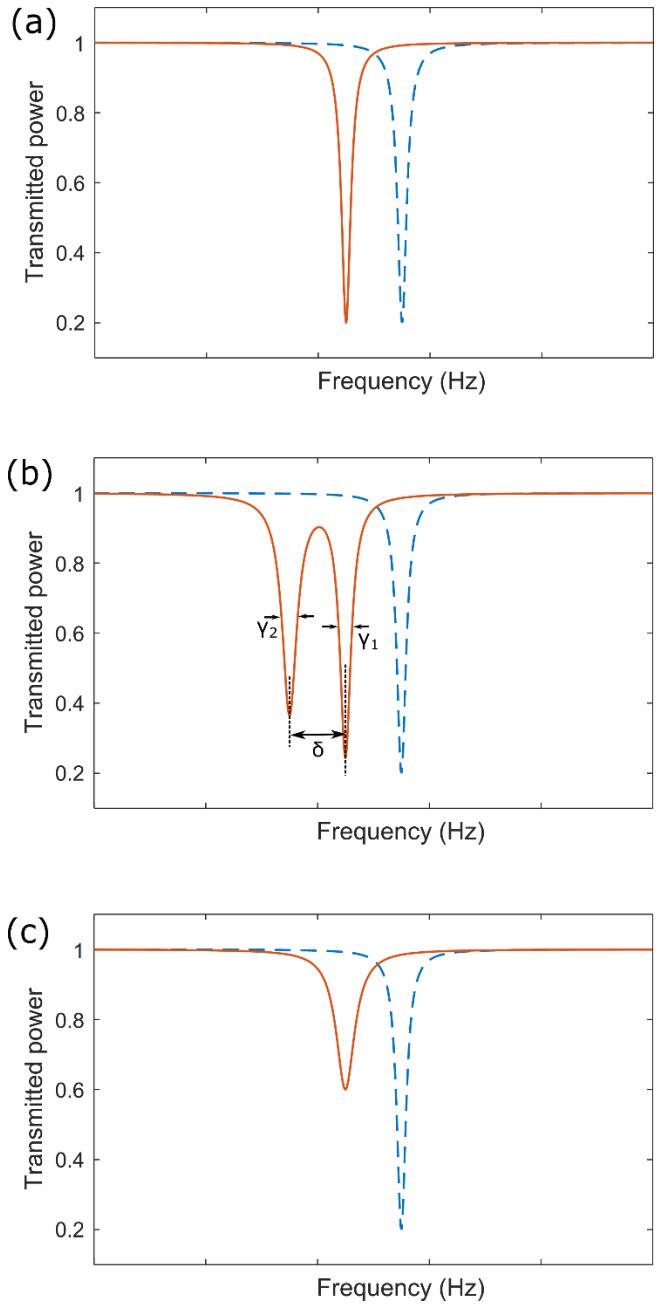

Figure 2.9. Different sensing modalities for WGM resonator. (a) Mode shift. (b) Mode splitting. (c) Mode broadening. Blue dotted curve represents the original spectrum, while red solid curve represents the spectrum after the introduction of the analyte in each case.

Chapter 3: Measurement of Hydrogel Gelation Using WGM Resonator

WGM resonators have already been proven to have an exceptional sensitivity to small particles and even single molecules. So far, the focus of WGM sensing has been on the detection of the presence of analytes. Equally important is the measurement of how the analyte molecule is dynamically changing; such changes include protein conformational changes, molecular diffusions and chemical reactions such as polymerization. In this chapter, we present the continuous monitoring of hydrogel gelation *in situ* using WGM resonators. This work does not represent any improvement in the sensitivity of WGM resonators, but it does represent one of the first works that use WGM resonators to monitor a chemical reaction and helps to point out some subtleties in such measurement. Specifically, we monitor and quantify the gelation dynamics of polyacrylamide hydrogels using WGM resonators and compare the results to an established measurement method based on rheology. Rheology measures changes in viscoelasticity, while WGM resonators measure changes in refractive index. Different gelation conditions were studied by varying the total monomer concentration and crosslinker concentration of the hydrogel precursor solution, and the resulting similarities and differences in the signal from the WGM resonator and rheology are elucidated. This work demonstrates that WGM alone or in combination with rheology can be used to investigate the gelation dynamics of hydrogels to provide insights into their gelation mechanisms. The work presented in this chapter has been published in Huang, S. H. *et al.* Whispering gallery mode resonator sensor for in situ measurements of hydrogel gelation. *Opt. Express* **26,** 51 (2018).

3.1. Background

Label-free biosensors are at the forefront of a new generation of technologies for small molecule detection. Labeling a molecule can adversely affect its chemical structure and function, and also quantitative analysis from fluorescent labels can be difficult due to photobleaching and autofluorescence.[57–59] Whispering gallery mode (WGM) resonators have emerged as a promising technology for compact and ultrasensitive optical, label-free biochemical sensing over the past two decades.[6,60–63] WGM resonators can detect, at a single-particle level, molecules such as viruses, proteins, nucleic acids, and even atomic ions.[4,5,56,64,65] Although many prior works have focused on the detection of particles and chemical moieties, WGM resonators can also have broader applications in investigating the dynamic processes that occur in the molecules of interest, such as protein conformational changes[66] and anomalous diffusion in polymers.[67] One potential application of WGM resonators that is yet to be investigated is characterizing dynamic material processes, such as the polymerization of hydrogels.

In this work, we report the first demonstration of using WGM sensors to continuously monitor a chemical reaction (i.e. gelation) in situ in a hydrogel. Specifically, we measure the gelation dynamics for polyacrylamide (PA) hydrogels using WGM sensors, which are sensitive to the changes in refractive index of the material upon gelation. PA hydrogels were chosen as a model system because their properties have been extensively studied and they are routinely used in a variety of applications including protein and DNA separation,[68] drug delivery,[69] and toxin removal.[70] The WGM measurements were validated by rheology, which, as explained in the next section, is a well-accepted method to measure hydrogel gelation by characterizing changes in viscoelasticity as gelation progresses.

3.2. Hydrogel

Hydrogels are a class of biomaterials with a broad range of applications in areas such as biochemistry and biopharmaceutics; in these fields, hydrogels are implemented in protein and nucleic acid assays,[71,72] drug delivery,[73–76] and cell culture.[77–80] The structural and chemical properties of hydrogels, including degradability, mechanical stability, and drug release mechanisms, depend heavily on the gelation conditions and dynamics.[81] Thus, measuring and understanding the gelation kinetics, efficiency and mechanism for hydrogels are important for understanding their structure-property relationships.

Due to its significance, several methods have been developed to monitor gelation. Nuclear magnetic resonance (NMR) can track changes in chemical structure as a solution polymerizes and has been used to follow gelation processes; however, it is very expensive, requires specialized equipment and is hampered by low resolution in aqueous environments leading to overlapping broad peaks.[82,83] Another common technique is the inverted tube method, which is simple but solely based on observation, and hence, prone to subjective and variable quantitative data.[84,85] Other specialized techniques to measure gelation include calorimetry, which is sensitive to heat-induced structural changes in the material upon gelation,[86] optical rotation measurements, which are sensitive to the degree of helical conformation,[87] and ultrasound, which is sensitive to the low-frequency changes in the material viscoelastic properties.[88] Rheology and micro-rheology are also commonly employed techniques to characterize the gelation of hydrogels.[89,90] In rheology, the rheometer applies an oscillating shear stress to the hydrogel while measuring its resulting strain. Through this force-based measurement, the viscosity and elastic properties of the materials are measured as the loss (G'') and storage (G') moduli, respectively. When a hydrogel precursor solution begins to polymerize, it becomes more elastic and the G' surpasses the G'';

the crossover point is termed the "gel point", indicating the formation of a critical number of crosslinks.[91] However, rheology cannot be easily implemented to study the gelation time of rapidly gelling or mechanically weak materials that could be disrupted by external stresses.[92] In general, there is no universal method capable of measuring gelation directly for any material and any gelation kinetics; hence, new and improved methods for gelation measurements are sought after. WGM resonators can serve well for this purpose, as it is based on an optical measurement that is fundamentally different from the traditional methods. WGM resonators can measure fast dynamics with high sensitivity, potentially on the order of micro- to nano-seconds, rendering them superior to many alternative methods.

3.2.1. Hydrogel Preparation

We studied the gelation kinetics of PA gels fabricated through the co-polymerization of various concentrations and ratios of acrylamide monomer and bis-acrylamide crosslinker. The different concentrations are summarized in **Table 1** and **Table 2**. We define the following variables:[93]

$$\%T = \frac{M_{Acr} + M_{Bis}}{V_{Sol}} \times 100 \tag{3.1}$$

$$\%C = \frac{M_{Bis}}{M_{Acr} + M_{Bis}} \times 100 \tag{3.2}$$

where %T is the total percent of monomer, %C is the percent of crosslinker, M_{Acr} is the mass of acrylamide, M_{Bis} is the mass of bis-acrylamide, and V_{Sol} is the total volume of solution. The reaction is a free radical polymerization initiated by ammonium persulfate (APS) and catalyzed by tetramethylethylenediamine (TEMED) as shown in **Figure 3.1**. To vary the gelation

conditions, we first increased %T, while keeping %C constant as presented in **Table 3.1**. Next, we increased %C, while keeping %T constant as presented in **Table 3.2**.

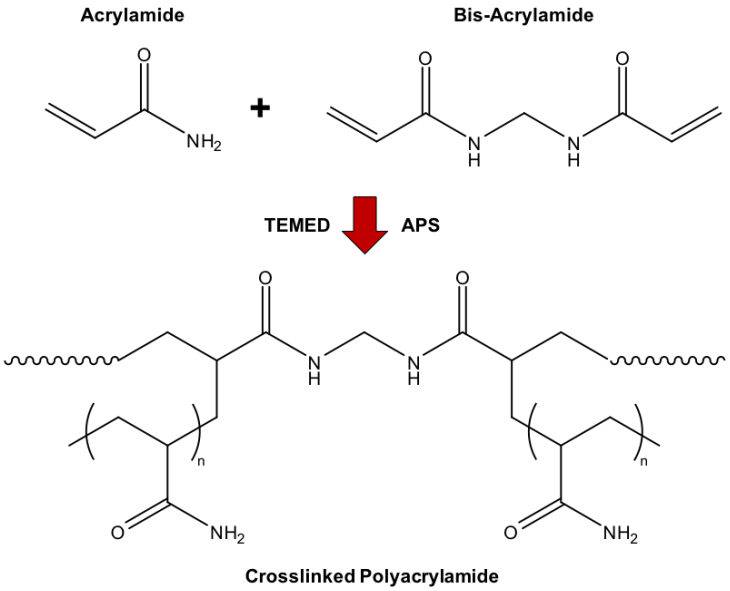

Figure 3.1. Gelation mechanism of polyacrylamide hydrogels. Ammonium persulfate (APS) acts as a free-radical initiator, while Tetramethylethylenediamine (TEMED) catalyzes the polymerization. The bis-acrylamide crosslinks the polyacrylamide chains to form a hydrogel network.

Table 3.1. Gel composition of PA precursor solution with increasing %T

Nomenclature	Acrylamide (%w/v)	Bis-acrylamide (%w/v)	%C	%T
PA-03-25	3.00	0.076	2.47	3.00
PA-05-25	4.88	0.124	2.48	5.00
PA-08-25	7.84	0.200	2.49	8.00
PA-10-25	9.76	0.248	2.48	10.00
PA-15-25	14.64	0.372	2.48	15.00

Table 3.2. Gel composition of PA precursor solutions with increasing %C

Nomenclature	Acrylamide (%w/v)	Bis-acrylamide (%w/v)	%C	%T
PA-08-01	8.00	0.010	0.125	8.00
PA-08-07	7.96	0.060	0.748	8.00
PA-08-12	7.90	0.100	1.25	8.00
PA-08-25	7.80	0.200	2.50	8.00
PA-08-37	7.70	0.300	3.75	8.00

3.2.2. Rheology

After the precursor solutions were prepared as described previously, they were pipetted onto the rheometer Peltier plate (AR 2000ex rheometer, TA Instruments, New Castle, DE). A time sweep was performed using a 20 mm parallel plate geometry and the rheometer properties were set as follows: 0.01% strain, 25°C, 1 rad/s angular frequency. The time sweep was run until saturation in the storage modulus (G') was reached.

3.3. WGM Sensor Design and Optical Characterization

To characterize the gelation, we prepared and used micro-bottle WGM resonators, as seen in the optical microscope image in **Figure 3.2**, along with the experimental setup for optical characterization. The bottle resonator was sandwiched between two glass slides, and a tunable laser scanning across a 0.12 nm spectral range around 765 nm was used to probe the WGMs of the resonator. A thermistor was placed close to the WGM resonator to investigate the contribution of temperature to the WGM signal. The thermistor was added because temperature affects the WGMs of the resonator[94] and PA gelation is an exothermic reaction [95]. Hydrogel precursor solutions were then pipetted into the gap between the two glass slides and the transmission spectrum of the bottle resonator was monitored *in situ* during hydrogel gelation.

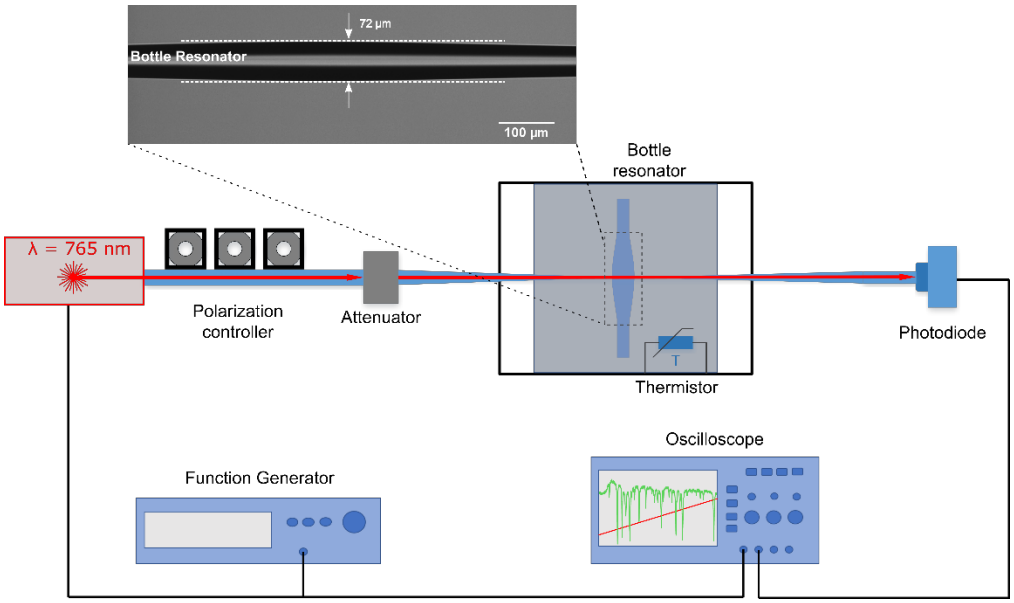

Figure 3.2. Schematic drawing of the optical characterization setup. Inset: micrograph of a typical bottle WGM resonator.

3.3.1. Bottle Resonator Fabrication

Bottle resonators were fabricated from standard silica optical fibers by tapering the fiber at two locations, creating a bulge in the center.[35,36] The tapering was done by pulling the fiber while heating it with a graphite filament. We utilized an automated glass processor (Vytran GPX3000) to finely control the shape of the resonator and the fabrication of multiple resonators with similar geometries, with a typical $Q > 10^7$ in the air. The diameter of a typical bottle resonator at its center was ~70 – 80 µm. The bottle resonator was intentionally made somewhat larger than previous ones to prevent excessive radiation loss in aqueous and gel environment.

3.3.2. Optical Characterization

The bottle WGM resonator was placed between two glass slides, with an approximately 2 mm gap between the two glass slides. A fiber taper was placed through the gap for optical coupling to

the resonator. This fiber taper was placed in gentle contact with the bottle resonator. To monitor the WGMs in the bottle resonator, an external cavity diode laser (Newport Velocity TLB-6700) was kept scanning across a 0.12 nm range around λ = 765 nm, and the transmission through the resonator was monitored using a photodiode. This wavelength was chosen rather than the commonly used 1550 nm wavelength band since at 1550 nm, the absorption loss of water is significant, leading to a lower quality factor.[96]

A cross-correlation algorithm was used to calculate the "average" wavelength shift of the WGMs present in the transmission spectrum. Cross-correlation was calculated for each successive frame of measurement and the lag that resulted in the maximum cross-correlation was taken as the wavelength shift between each successive frame, as in

$$\Delta\lambda_{shift} = \arg\max_{\lambda}((f_t \star f_{t+\Delta t})(\lambda)) \tag{3.3}$$

Here, f_t and $f_{t+\Delta t}$ are the observed transmission spectrum at time t and $t+\Delta t$, $\Delta\lambda_{shift}$ is the wavelength shift between these two frames, and $\star$ denotes cross-correlation. To calculate the wavelength shift as a function of time, the wavelength shift between each consecutive frame is added together and the cumulative wavelength shift is presented.

3.4. *In Situ* Measurement of Hydrogel Gelation

WGM sensors measure the change in refractive index of the hydrogel surrounding the resonator through its evanescent field and translate any change in the refractive index of the gel to a shift in the WGM resonance wavelength. In general, the refractive index of a polymer is influenced by several factors: formation of chemical bonds, change in gel density, and the introduction of

additional stresses and strains within the gel.[97–99] The measurement of this refractive index change can be done in many ways, including a prism-based refractive index measurement[100] and several techniques based on optical fibers,[88,98,101] but WGM sensing is expected to have one of the highest sensitivity among these techniques. Typically, the refractive index of a precursor solution increases as monomers are polymerized, and this is thought to be predominantly caused by an increase in the mass density of the gel.[88,97,98,100,101] The chemical reaction itself may also be exothermic, as is the case for PA gels, which increases the temperature of the hydrogel and in turn influences its refractive index.[102] The direction and magnitude of WGM wavelength shift upon temperature increase then depend on the thermo-optic coefficient of the gel, as well as that of the resonator.[94,103]

3.4.1. WGM Wavelength Shift Upon Hydrogel Gelation

Figure 3.3(a) shows a representative transmission spectrum of a typical bottle resonator embedded in a PA hydrogel. WGM sensing typically tracks the wavelength shift of one WGM using a peak-finding algorithm. However, continuously measuring a single WGM was found to be unreliable in the context of hydrogel measurements. We noted that the shrinkage of the PA gel during gelation could physically move the relative position of the fiber taper and the resonator, changing the coupling between the fiber taper and WGMs. Interestingly, we observed that all WGMs that appear in the transmission spectrum shifted together during hydrogel gelation, with less than 10% difference in the total wavelength shift amongst different modes, as shown in **Figure 3.3(b)**. In general, different WGMs have slightly different penetrations of the evanescent fields into the gel relative to their total mode volume, and thus, their wavelengths shift by different amounts. However, our observations suggested that for the WGMs of a bottle

resonator coupled to a fiber taper at a particular position, the difference in sensitivity among these WGMs was small.

Taking advantage of this observation, we used a cross-correlation-based algorithm to track the "average" shift of all modes present in the transmission spectrum. **Figure 3.3(b)** presents the wavelength shift of five WGMs recorded using a peak-finding algorithm in comparison to the shift obtained from the cross-correlation algorithm. As evident from the wavelength shift curves, the result obtained from the cross-correlation algorithm agreed with the wavelength shift of each individual WGM. The advantage in using the cross-correlation method as opposed to the single-mode-tracking method is in improved data reliability and repeatability. For example, in the curve for "WGM 1" in **Figure 3.3(b)**, there was a jump in an otherwise continuous curve that was caused by the difficulty in tracking the original mode due to coupling change. This effect of coupling change was circumvented by using the cross-correlation method. In addition, the cross-correlation method also worked for the sometimes non-ideal, Fano-resonance-like lineshapes of the WGMs,[104,105] which could be difficult to analyze using the single-mode-tracking method.

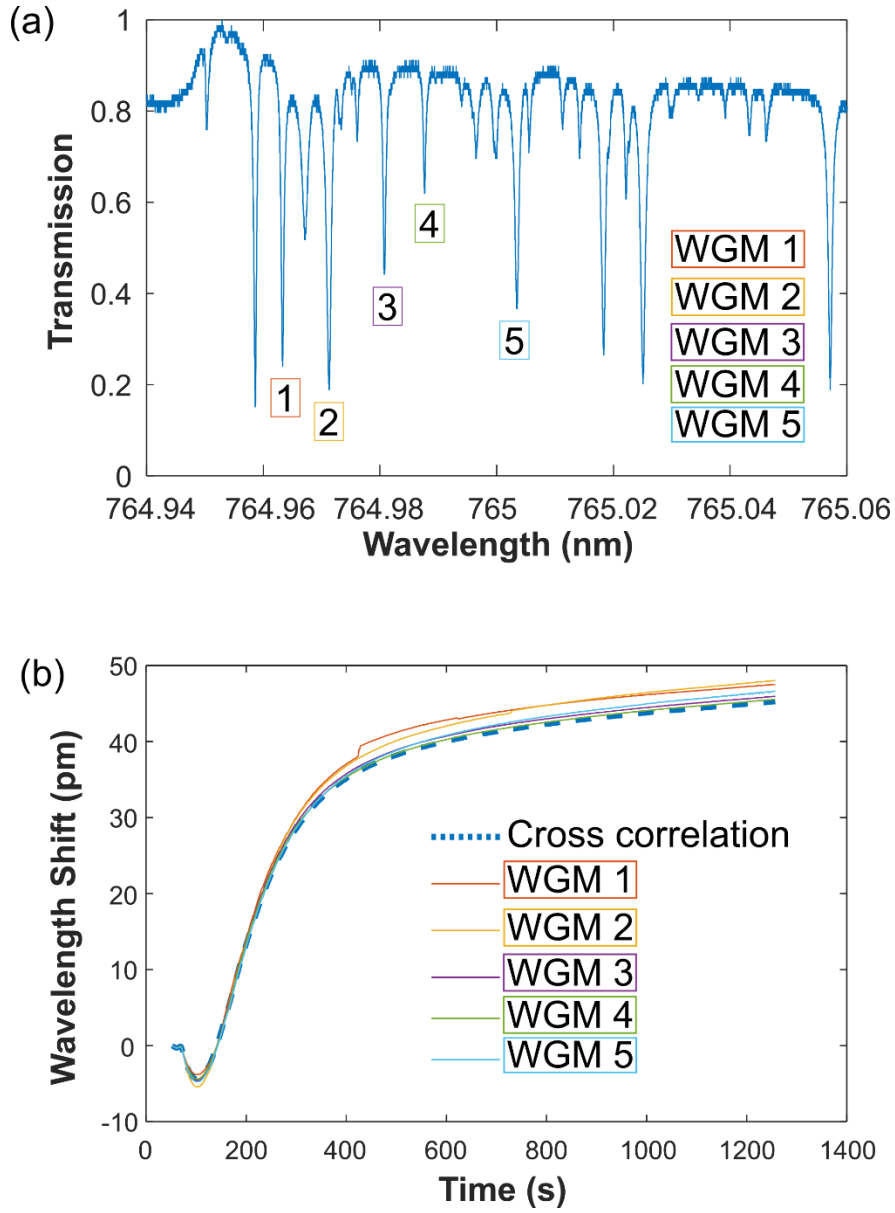

Figure 3.3. Mode shift of WGMs in a bottle resonator. (a) Transmission spectrum of a bottle resonator embedded in a PA-08-37 gel. (b) Wavelength shift of five different WGMs, which are indicated in (a), compared with the wavelength shift obtained from a cross-correlation method.

As expected from the exothermic nature of the PA polymerization reaction,[95] we found that there was significant temperature increase during PA gelation, as shown in **Figure 3.4**. The

temperature typically increased by ~2 – 3 °C during the initial phase of gelation (it is important to note that the temperature increase is dependent on monomer concentration), followed by a gradual cooling to room temperature. We suggest that this change in temperature was responsible for a small blue shift at the onset of gelation as described later. To validate the WGM measurements, we used rheology to follow PA hydrogel gelation and compared gelation measurements from both methods. This result is shown in **Figure 3.5.** WGM sensing measures the refractive index of the gel, while rheology measures the gel's storage modulus (G') and loss modulus (G''), rendering it sensitive to changes in PA viscoelasticity upon gelation. Thus, the origin of the signal for the WGM sensing and rheology are fundamentally different. Despite this difference, the overall pattern of the gelation curve obtained with the two methods agreed well; both showed an initial lag followed by rapid gelation and eventual saturation, which is typical for PA gelation.[106] In order to obtain quantitative measures for the gelation kinetics of each gel composition, we calculated two parameters: the gelation time and total change in the measured signal (resonance wavelength shift for WGM or storage modulus for rheology). These parameters were found from fitting the experimental gelation curve to Hill equations:[106]

$$G'(t) = G'_{\infty} \frac{1}{1 + (\frac{t_{gelation}}{t})^{m}} \tag{3.4}$$

$$\Delta\lambda(t) = \Delta\lambda_{\infty} \frac{1}{1 + (\frac{t_{gelation}}{t})^{m}} \tag{3.5}$$

where G'_{∞} and $\Delta\lambda_{\infty}$ are the final steady-state storage modulus and resonance wavelength shift, respectively; $t_{gelation}$ is the gelation half-time, and this value was taken as the measure of the characteristic gelation time for a particular gel. Finally, *m* is the Hill coefficient, related to the slope of the gelation curve at gelation half-time. Note that in contrast to the elastic modulus measured by rheology, the total resonance wavelength shift of the WGM sensor corresponded to refractive index change, which is thought to predominantly result from the change in the density of the gel.[107]

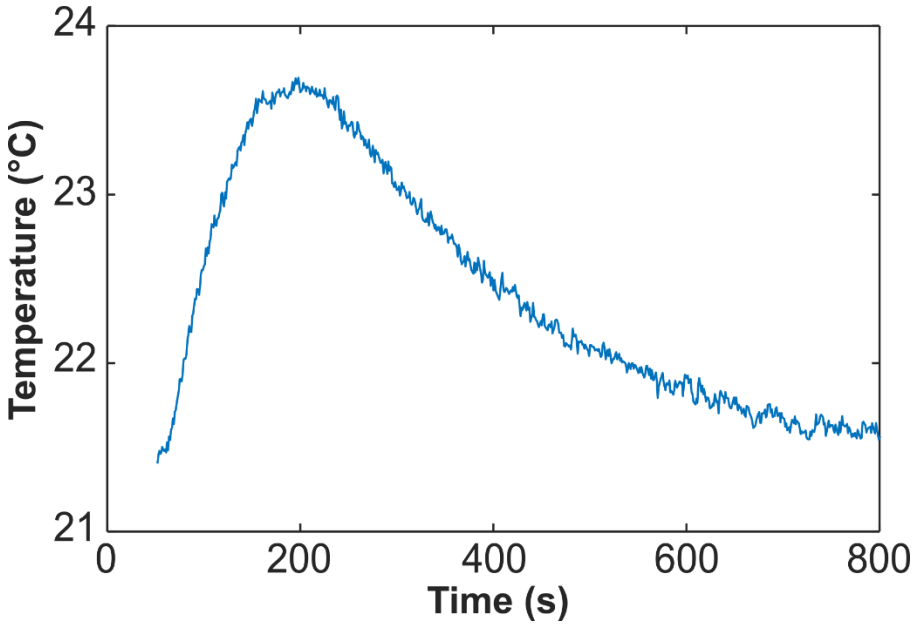

Figure 3.4. Temperature change within the gel measured by a thermistor.

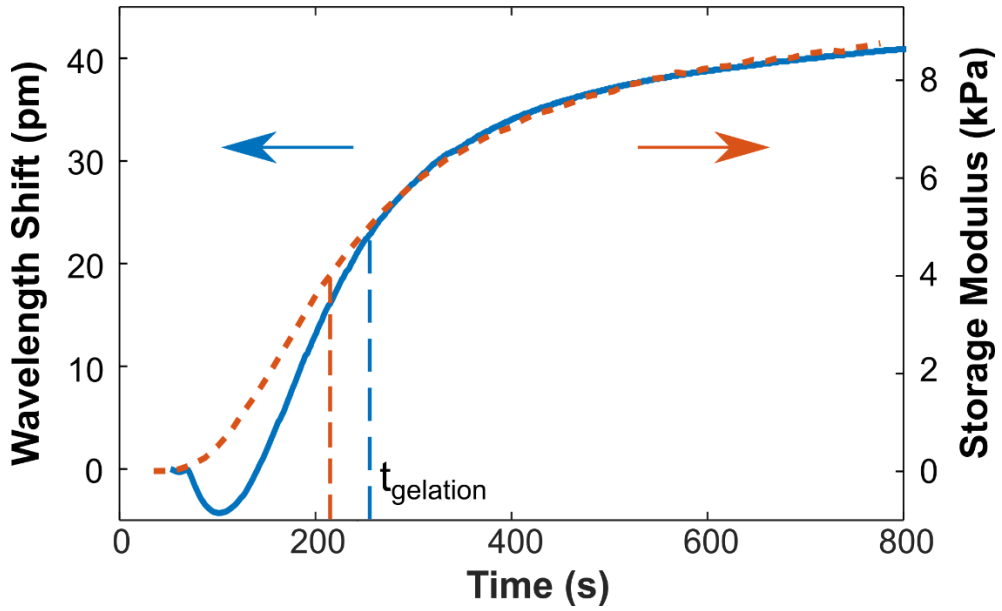

Figure 3.5. Wavelength shift during gelation (blue, solid curve) measured by a WGM resonator, and storage modulus change during gelation (red, dotted curve) measured by rheology. The gelation times ($t_{gelation}$), for both the WGM curve and the rheology curve, are indicated in the figure.

We noted from **Figure 3.5** that for the WGM measurements, there was a small blue-shift (dip) at the onset of gelation, while for the rheology measurement no such dip was observed. We suggest that this blue-shift measured with WGM was a result of an increase in temperature during gelation. Similar trends in the curing of polymers have been previously observed in PA gels using an ultrasound technique[88] and in resin systems using optical fiber-based techniques.[98,101] Note that silica (the bottle resonator) has a positive thermo-optic coefficient,[94] so a red-shift could be expected in WGM wavelength upon temperature increase. However, heat from the exothermic polymerization reaction was generated in the PA gel surrounding the resonator and needs to diffuse into the silica micro-bottle from outside. We assumed that the thermo-optic coefficient of the curing PA gel was dominated by that of water,[108] so the PA gel itself had a negative thermo-optic coefficient. Since the evanescent field of the WGM penetrates into the gel

surrounding the resonator, the final wavelength shift of the resonator depends on the contribution from both the silica resonator itself, as well as that of the surrounding gel. We suggest that upon heat generation in the PA gel, the gel heated up first without transferring the heat fast enough to the silica resonator, which resulted in a blue-shift in the WGM wavelength initially. Eventually, the silica resonator heated up sufficiently to exhibit an overall red-shift. However, further work is still necessary to confirm the exact origin of this initial blue-shift.

3.4.2. WGM Sensing and Rheology with Different Hydrogel Composition

To further validate the suitability of the WGM resonator technique to measure hydrogel gelation, we varied PA gelation kinetics by changing total monomer concentration (%T) and crosslinker concentration (%C) and compared the changes in gelation time and total signal change, as measured by WGM sensing and rheology. The results for varying %T is presented in **Figure 3.6**, while that for varying %C is presented in **Figure 3.7**. All results were reported as mean values ± standard deviation of triplicates performed in three independent experiments. The two methods to measure gelation time were compared using a two-tailed Student's t-test. Differences were considered significant when $p < 0.05$.

Overall, WGM appeared to measure a slightly shorter gelation time than rheology, albeit the difference was only significant for one gel composition (PA-08-25). This difference in measured gelation times could be due to the differential changes in hydrogel density (indirectly leading to refractive index change) and modulus with the progression of the gelation reaction. For PA gels, the first step of gelation is the formation of micro-gel particles, which do not substantially contribute to the gel elasticity but contribute to gel density, followed by the formation of crosslinks between the micro-gel particles, which contribute to both gel elasticity and density.[106]

We suggest that the formation of these micro-gel particles resulted in an earlier density change measured by WGM and a later elasticity change measured by rheology.

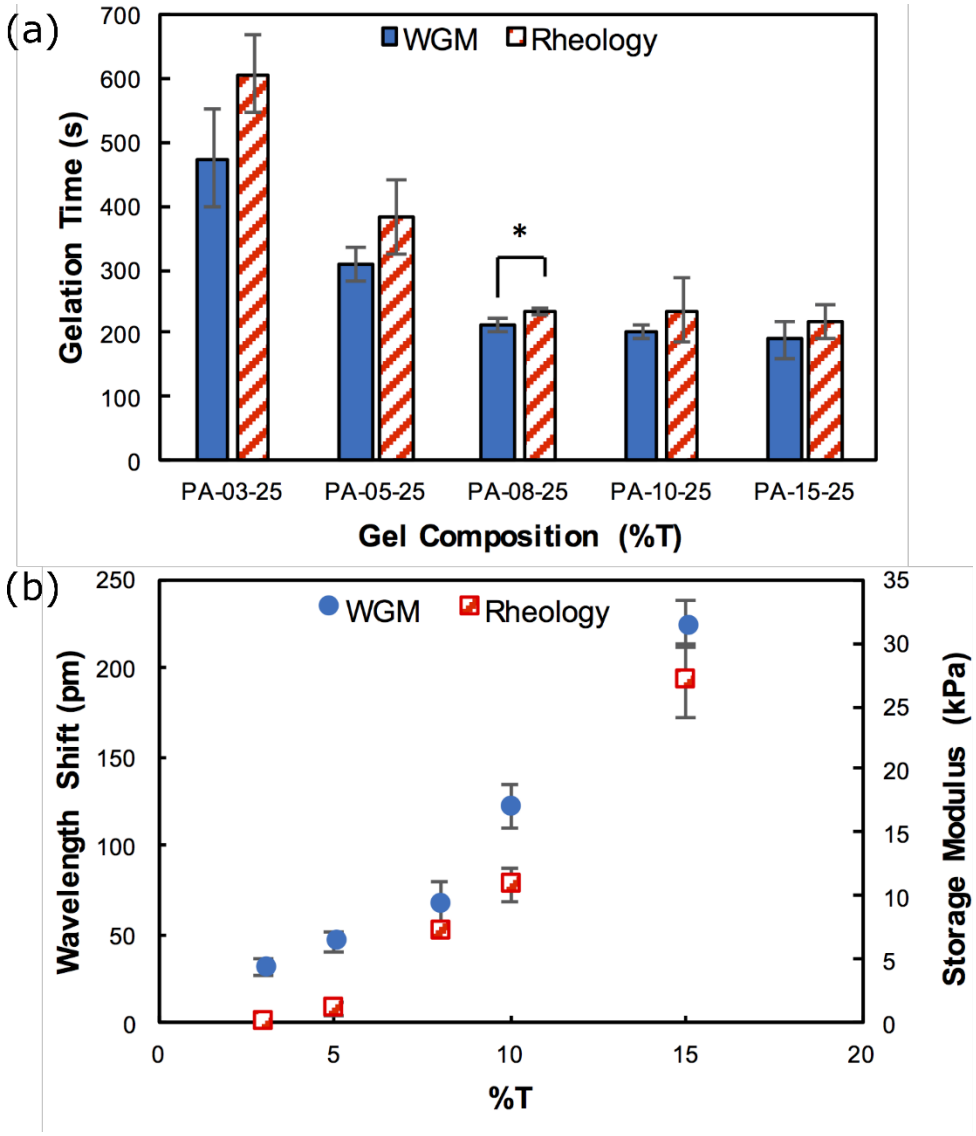

Figure 3.6. Gelation kinetics of PA hydrogels prepared with varying amounts of total monomer concentration (%T). (a) Gelation times for different gel composition. (b) Steady-state resonance wavelength shift and storage modulus for different gel composition.

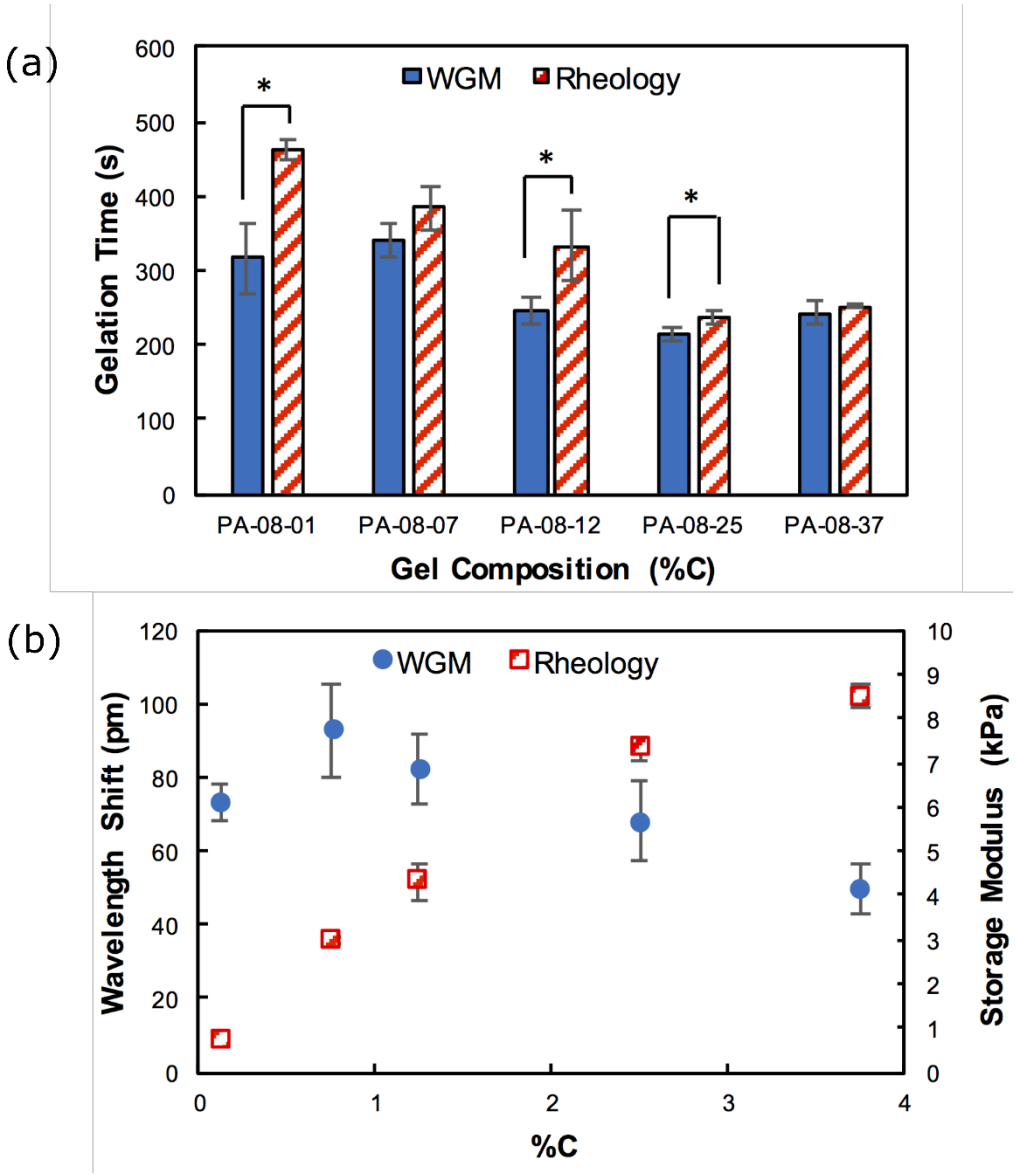

Figure 3.7. Gelation kinetics of PA hydrogels prepared with varying amounts bis-acrylamide (%C). (a) Gelation times for different gel composition. (b) Steady-state resonance wavelength shift and storage modulus for different gel composition.

Both the final steady-state WGM wavelength shift and storage modulus increased as %T increased, as shown in **Figure 3.6**. This suggested that as %T increased, a stiffer PA gel was formed (a higher storage modulus as measured by rheology) with a greater density (i.e. higher refractive index). The decrease in gelation time and increase in storage modulus of PA hydrogels with increasing %T was expected.[80,109,110]

As for variation in %C, it has been shown that an increase in %C leads to a decrease in the gelation time of PA hydrogels, albeit to a lesser extent than an increase in %T.[111,112] As expected, in **Figure 3.7** we observed a small but significant decrease in PA gelation time with an increase in %C.

An increase in the storage modulus was observed from rheology as %C was increased, which was expected because %C is directly correlated to hydrogel stiffness.[80,110,113] However, unlike the storage modulus, the WGM wavelength shift was essentially uncorrelated with %C change. This can be interpreted as the following; although %T affects both the density and elasticity of the hydrogel, %C predominantly affects the hydrogel elasticity due to the formation of additional crosslinks,[106] while having little influence on its density. Our results highlight the similarities and differences in the signal obtained from WGM and rheology and demonstrate that the two techniques provide complementary information on hydrogel gelation and the underlying changes in hydrogel properties.

3.5. Conclusion

In conclusion, we developed a novel WGM sensing technique to characterize hydrogel gelation. The WGM wavelength shift was linked to the density and refractive index changes of the hydrogel as gelation progressed. This novel method was validated by rheology, which measures

changes in hydrogel elasticity upon gelation. Both WGM sensing and rheology characterized gelation, but with slight differences; for instance, a small blue shift was observed at the onset of gelation with WGM sensing but not with rheology, likely attributed to the different sensitivity to temperature changes between the two methods. Estimates of gelation time through rheology appeared slightly higher compared to estimates through WGM, especially at low %C and %T, due to the different dependence of hydrogel microstructure, density, and crosslinking on monomer and/or crosslinker concentration. Our study shows that WGM alone or in combination with rheology can be used to investigate the gelation dynamics of other hydrogels and provide insight into their gelation mechanisms.

Chapter 4: Surface-Enhanced Raman Scattering using WGM Resonator

The sensing modalities discussed so far, whether mode shift, mode splitting, or mode broadening, relied on the detection of an analyte from its refractive index or polarizability. This enables the detection of analyte with an excellent limit of detection, and in the case of mode-splitting, allows for the measurement of particle size if the particle's refractive index is known.[50] However, none of the techniques discussed so far offer any specificity to the detection.; although we can determine when and whether something binds to the resonator, we cannot know what it is that has been bound to the resonator. One way to add specificity to the detection is to use Raman spectroscopy, in which the chemical composition of a material is determined through its molecular vibration. This chapter discusses the use of WGM-resonator-based Raman spectroscopy for improved sensing specificity. As it turns out, WGM resonators can enhance the strength of Raman signal due to cavity resonance effect, much like the popularly used surface-enhanced Raman spectroscopy (SERS).[114] This effect has been studied through experimental observations and theoretical calculations, and a Raman enhancement factor of 1.4×10^4 is demonstrated in this work. The work presented in this chapter has been accepted for publication in Huang, S. H. *et al.* Surface-enhanced Raman scattering on dielectric microspheres with whispering gallery mode resonance, *Photonics Research* **6,** 2 (2018).

4.1. Introduction

WGM microresonators, such as microspheres and microtoroids, have attracted much interest for their potential application in label-free sensing of biomolecules, nanoparticles, and chemicals.[6,63] These resonators have ultra-high quality (Q) factors and small mode volumes, allowing for

greatly enhanced light-matter interaction and very high sensitivity to adsorbed analytes. Label-free, single particle level sensitivity to virus particles, proteins, nucleic acids, and even single ions has been demonstrated.[2–4,56,64,115,116] Currently, the sensing schemes are based on observing the change in the transmission spectrum of the resonator, appearing as either shift, splitting, or broadening of the resonance mode.[2,50,56] In essence, all of these sensing schemes measure the polarizability of the analyte, and WGM resonator sensors lack specificity beyond distinguishing entities with different polarizabilities. Although sensing specificity can be added to the system by surface functionalization, a complementary method to WGM sensing that can provide molecular fingerprints of the analyte without functionalization is desirable.

Raman spectroscopy is a widespread analytical technique that can be used for material identification without labeling or functionalization. Raman scattering is typically a weak process, but the introduction of surface-enhanced Raman scattering (SERS) has greatly improved the detection limit of Raman spectroscopy. In SERS, the analyte is placed on nanostructured metallic surfaces or metallic nanoparticles, typically made of coinage metals such as Au, Ag, and Cu, and the plasmonic "hotspots" produced by these metallic structures are used to enhance the Raman signal. Large enhancement factor on the order of $10^{10} – 10^{12}$ has been reported from SERS, making Raman detection of single molecules possible.[117–119]

Large field enhancement, however, is not unique to plasmonic structures alone. Recently, the use of dielectric and semiconductor micro/nanostructures as SERS substrate has been receiving increasing attention.[120–133] These dielectric and semiconductor substrates, typically made of SiO_2, Si, or TiO_2, have several advantages over metallic SERS substrates. Dielectric SERS substrates are more stable under high-temperature and harsh electrochemical conditions,[127,133] leading to a more repeatable SERS enhancement. Dielectrics also have reduced perturbation of the analyte

both chemically and thermally.[134,135] In particular, the local heating of metallic nanostructures upon optical pumping can be very significant,[136] which can adversely affect both the SERS substrate[137] and the analyte.[135] It has been shown that in dielectric nanostructures this heating can be negligible.[121]

Dielectric SERS substrates can come in many forms, with microspheres or 2D/3D arrays of microspheres as one of the most popular ones. However, the exact mechanism for Raman enhancement in these dielectric microspheres is still not completely understood, due to the complexity that arises from the interplay between many mechanisms that are involved.[120] Several enhancement mechanisms have been identified so far, with the most studied electromagnetic effects being photonic nanojets and WGM resonances, often also called morphology-dependent resonances in this context. Photonic nanojets are non-evanescent and non-resonant beams of light with enhanced field intensity, which are formed on the shadow-side of the microspheres when the microspheres are illuminated from above. An example of photonic nanojet is presented in **Figure 4.1**. Due to the focusing of pump light at the nanojet, Raman signal from a sample under the microsphere is enhanced, typically by approximately a factor of 10 – 100.[122–126] WGM resonances in these microspheres, on the other hand, are theoretically predicted to have Raman enhancement up to 10^8, comparable to metallic SERS substrates,[138,139] but experimental demonstrations of Raman enhancement from WGMs in dielectric microspheres has been very limited and inconclusive so far.[123,127,128] Other Raman enhancement mechanisms identified in arrays of microspheres and inverse opal structures include Fabry-Perot effects,[123] photonic bandgap effects,[129] and directional antenna effects.[130] Also, chemical enhancement attributed to charge transfer complexes is often observed from semiconductor substrates, such as TiO_2 and ZnO.[131,132]

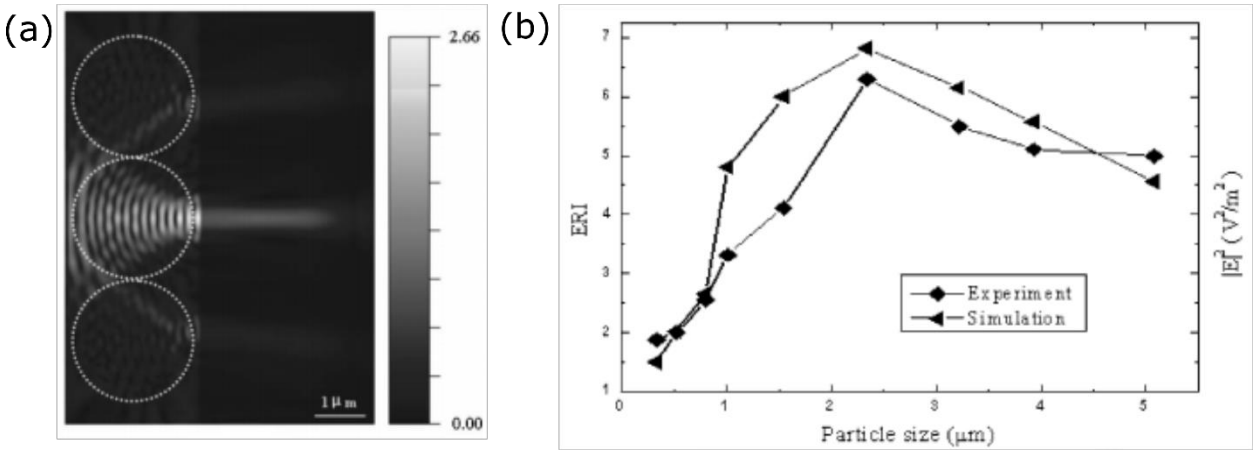

Figure 4.1. Photonic nanojet. (a) Simulation showing the electric field distribution in a photonic nanojet and (b) its corresponding Enhancement of Raman Intensity (ERI). Reprinted from Ref. 126.

The difficulty in studying WGM enhancement mechanism in microspheres mainly arises from the inefficiency in pumping the WGMs with conventional micro-Raman spectroscopy setup, which is often designed for conventional Raman signal or SERS signal from metallic substrates.[119] In dielectric microspheres, the linewidth of a typical WGM resonance is much narrower than that of plasmonic resonances in metallic nanostructures. In addition, these narrow WGMs often shift by more than their linewidths upon analyte adsorption or photothermal heating due to the pump light. Thus, although a fixed-wavelength excitation laser is suitable for pumping the broad plasmonic resonances, pumping the narrow and fluctuating WGMs poses a significant challenge. Further, since the dielectric microspheres that support WGMs are larger than the wavelength of excitation light, phase matching between the excitation beam and the WGMs can no longer be ignored, as in the case for plasmonic resonances from metallic nanoparticles. This leads to an inefficient coupling of light from free-space beam to WGMs even

when the wavelengths are matched. Inefficient coupling to WGMs from these factors often results in the effect of WGM enhancement being masked by other phenomena.

In this work, we study the WGM Raman enhancement mechanism by pumping a single silica microsphere through tapered fiber coupler using a narrow-linewidth tunable laser. Tapered fiber couplers can couple more than 99% of the pump light into a single WGM in ideal conditions[140] and therefore have been routinely used for experiments with WGM resonator based sensors and microlasers.[115,141] By using a tapered fiber coupler to pump a single microsphere, we also avoid other electromagnetic effects in microspheres such as photonic nanojets. In addition, the use of a silica microsphere excludes the contribution of chemical enhancement. Thus, the entire Raman enhancement can be attributed to WGM mechanism. From our result, we observed a clear enhancement of Raman scattering and modified Raman emission spectra due to WGMs. Our work demonstrates that significant Raman enhancement is possible using the same platform as that for WGM sensors, allowing for the two techniques to complement each other; Raman spectroscopy provides added molecular specificity to WGM-resonator-based sensors, while the WGM resonator enhances the strength of Raman signal.

4.2. Experiment Method

4.2.1. Fabrication of Silica Microsphere

Silica microspheres were fabricated on a silicon chip, with each microsphere supported by a silicon "pillar."[30,31,142] The fabrication of this type of microsphere is similar to that of microtoroid and has been discussed in Chapter 2 of this dissertation. An SEM image of the microsphere used for this experiment is provided in **Figure 4.2**.

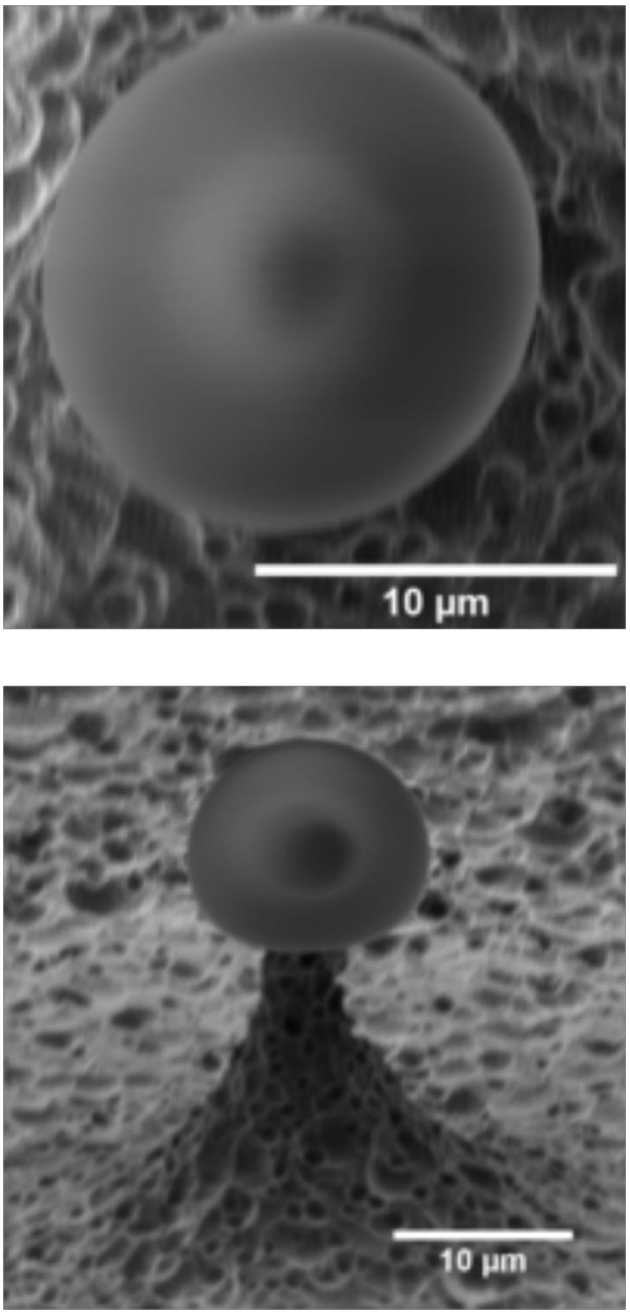

Figure 4.2 SEM image of a typical on-chip microsphere used in this experiment. Top: top view and bottom: side view of the same microsphere resonator.

4.2.2. Optical Setup

We used an in-house built Raman spectrometry setup to collect the Raman emission from the microsphere, the schematic drawing of which is shown in **Figure 4.3**. A fiber-coupled external cavity tunable laser (765 nm – 781 nm) was used to excite the WGM resonances. As the pump light travels through the fiber, it excites Raman scattering from the silica fiber, which can interfere with the Raman signal from the microsphere; an 800 nm short pass filter was used to remove this Raman signal generated in the optical fiber. After this filter, the pump light propagates through a tapered fiber which was coupled with the microsphere. Finally, the transmitted light through the tapered fiber coupler was measured using a photodiode to monitor the coupling of the pump light to WGMs in the microsphere.

The Raman emission from the microsphere was collected from the top by a long working distance objective (NA = 0.55). The objective was also used for imaging the microsphere resonator. In order to separate the Raman emission collection path from the imaging path, an 805 nm dichroic mirror was used. An 800 nm long pass filter was used to remove the Rayleigh scattered pump laser, after which the Raman emission spectrum was recorded using a grating spectrometer.

A free-space excitation path was included in the setup to compare the tapered fiber excitation with conventional free-space excitation of Raman scattering. The same tunable laser was used for excitation; this laser was coupled to free space through a collimator and a beam expander was used to adjust its beam size. A cleanup filter was used to remove the Raman emission generated in the fiber. The pump laser was focused on the microsphere through the same objective that was used for imaging.

For pumping with tapered fiber coupler, the chip with microsphere was mounted vertically on its side and the light scattered from the WGMs was collected with the optical axis of the collection objective in the equatorial plane of the microsphere. Since most of the light from the microsphere is scattered in the equatorial plane due to radiation loss, this collection scheme is more efficient than collecting light scattered perpendicular to the equatorial plane. For free-space pumping, the chip was placed horizontally so that the pump light was incident on the microsphere from the top.

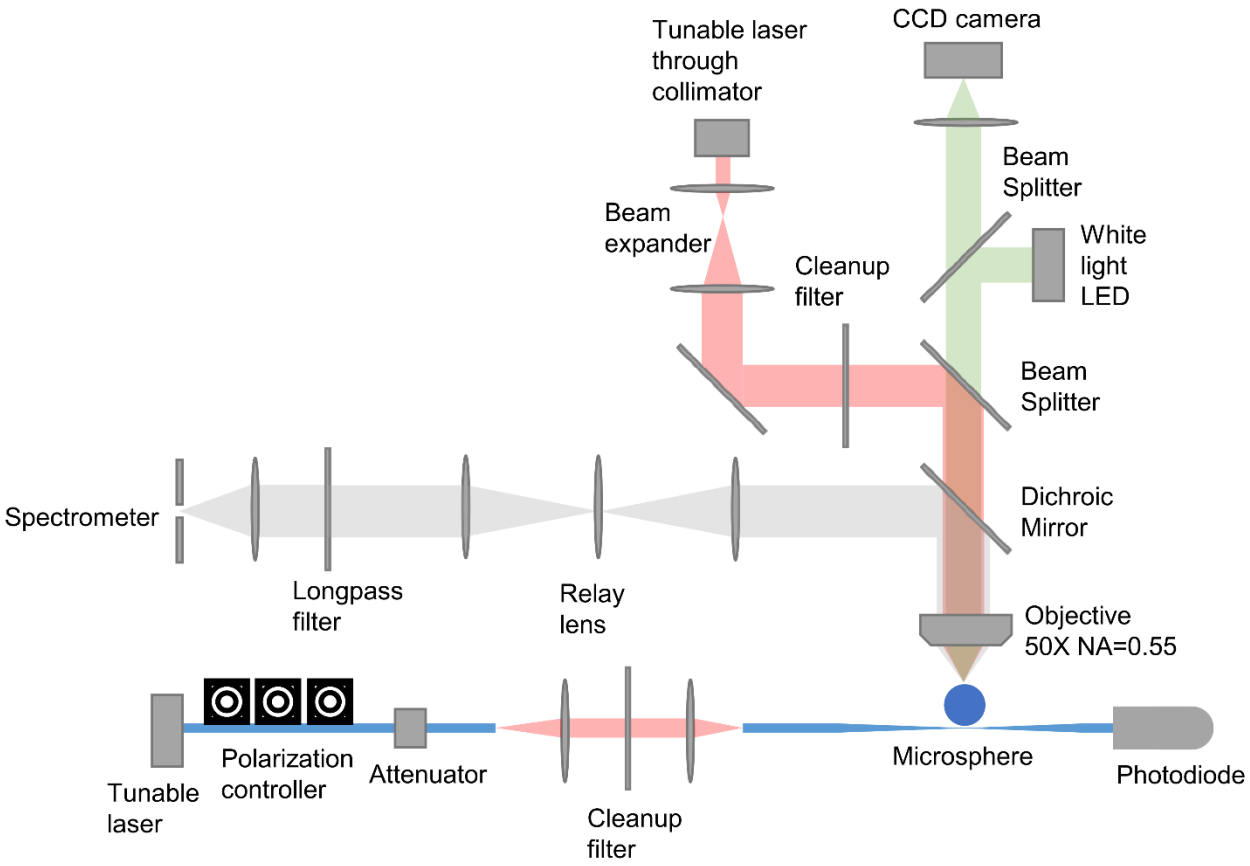

Figure 4.3. Schematics of the optical setup for Raman spectroscopy.

4.2.3. Rhodamine 6G Coating

To study the microsphere's Raman enhancement for surface-adsorbed molecules, we coated the surface of the microsphere with rhodamine 6G and studies the enhancement of its Raman scattering. 1 μL of 5 mg/mL rhodamine 6G solution in ethanol was dropped onto the chip with the microsphere and was dried in the air.[127] The resonance wavelength of the pump WGM was measured before and after rhodamine 6G coating. From the shift in the WGM's resonance wavelength, we estimated the thickness of rhodamine 6G on the microsphere to be 3.4 nm. The thickness of the rhodamine 6G layer on the substrate was estimated to be 200 nm based on the amount of rhodamine 6G deposited and was confirmed with an SEM measurement (**Figure 4.4**). This large difference in the amount of analyte being pumped is important in calculating the enhancement factor, and being able to measure the amount of rhodamine 6G molecules on the microsphere through WGM resonance wavelength shift is a significant advantage in our system.

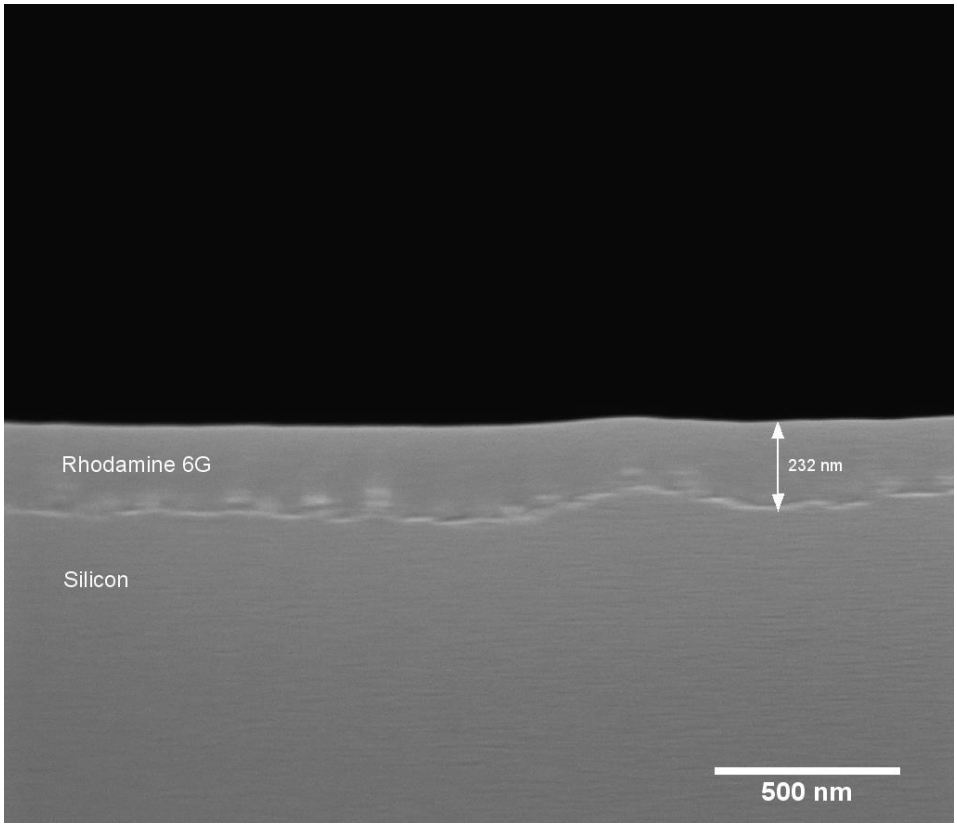

Figure 4.4. SEM image of rhodamine 6G on a silicon substrate. There was some variation in the thickness of rhodamine 6G due to the surface roughness of silicon created by XeF_2 etching, but 200 nm was a reasonable approximation for the thickness of rhodamine 6G.

4.3. Results and Discussions

4.3.1. Raman Lasing in Silica Microsphere

Raman lasing in silica microsphere and microtoroid resonators is a well-known effect,[32,141] but the occurrence of Raman laser is detrimental to our work in Raman spectroscopy in two ways. First, the contribution from significant stimulated emission makes our estimate of Raman enhancement factor highly inaccurate. Second, any Raman laser in the microsphere may cause cascaded Raman lasing which acts as secondary pumps that distort the measured Raman spectrum. To ensure that there is no contribution from Raman lasing, we first characterized the

lasing threshold in our microspheres, the result of which is shown in **Figure 4.5**. The Raman lasing threshold was identified to be around 200 μW; for the subsequent experiments, the pump power was kept to below 100 μW to avoid contribution from stimulated Raman scattering. The inset of **Figure 4.5** shows the sub-threshold portion of the Stokes light intensity; this part has a linear dependence on pump power, as expected from spontaneous Raman scattering.

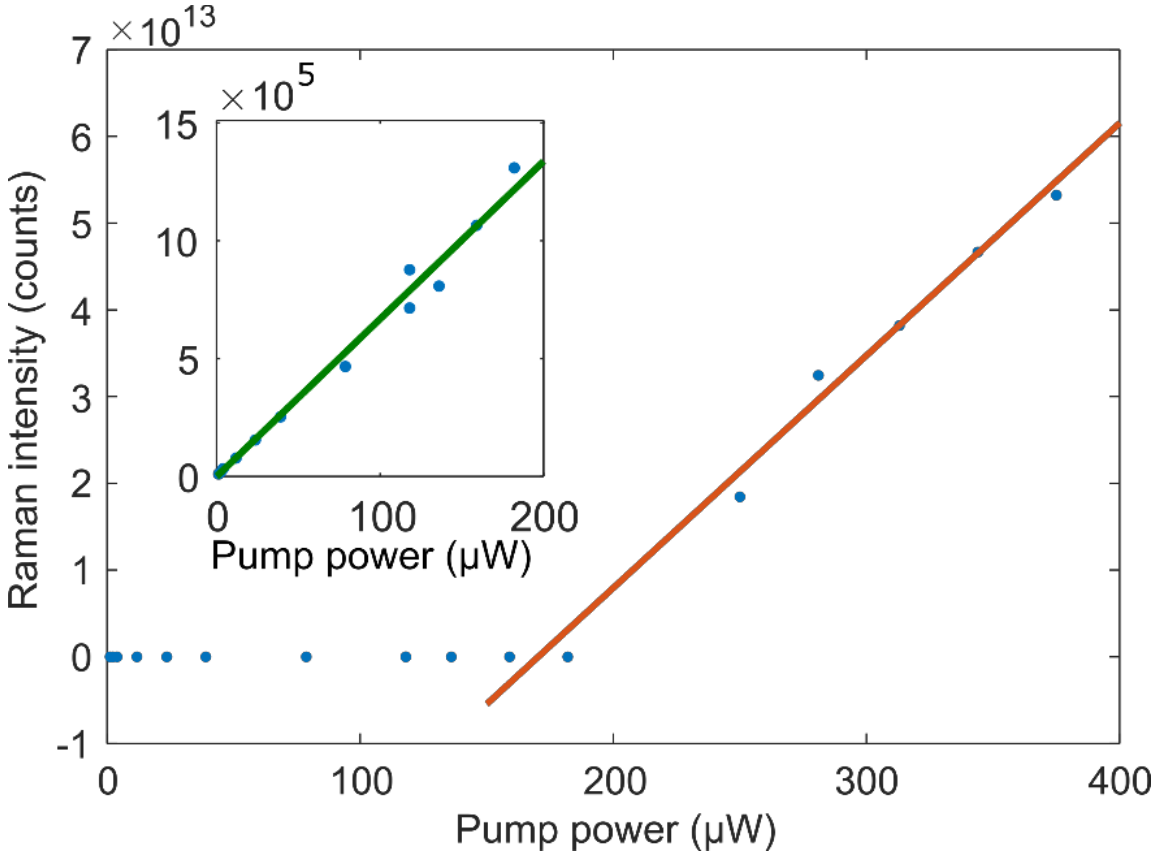

Figure 4.5. Raman lasing and thermal effects in silica microspheres. (a) Raman intensity dependence on pump power for a bare silica microsphere. The inset shows the linear dependence of Raman intensity vs pump power in the spontaneous Raman emission regime.

4.3.2. Thermal Effects in Microsphere Resonator

Thermal drift and/or thermal nonlinearity are another effect that needs to be considered before the collection of Raman spectra. A microsphere with a diameter of 13.8 μm and a WGM at 767.54 nm with an intrinsic Q factor of 2 x 10^7 was used for this measurement (**Figure 4.6**). The resonance mode is split into two due to the coupling of clockwise and counterclockwise traveling wave modes. At high power, there was strong thermal broadening in the observed transmission spectrum of the WGM, as presented in **Figure 4.6 (b)**. This broadening arises due to the shift in the resonance wavelength caused by the heat generated by the pump light and several picometers of resonance wavelength shift is observed regularly even for modest pump power (few tens of μW).[143] This suggests that without a tunable laser and active monitoring of the WGM, it is very difficult to couple a high-intensity pump light efficiently into the WGM, since as soon as the pump light is coupled in, the WGM shifts, reducing its spectral overlap with the pump light. In collecting the Raman scattered light, we keep the pump light scanning across the WGM during Raman signal collection and calculate from the transmission spectrum the fraction of pump power coupled into the resonator on average (typically 0.2 - 0.5, for more details see section 4.4.1); this fraction is accounted for when we compare the Raman intensity from different spectra. Although the pump efficiency is not ideal, we find that this method results in a stable and quantifiable coupling of the pump power into the WGM over the spectrometer's integration time.

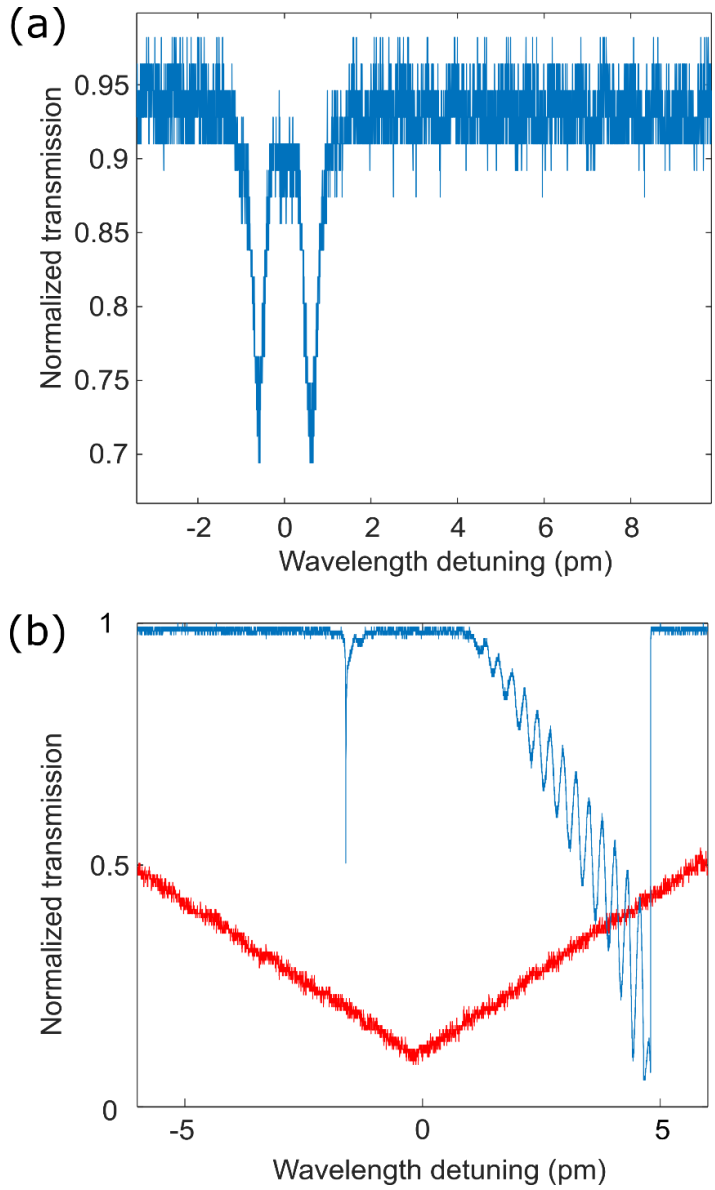

Figure 4.6. Thermal effects in microsphere WGM resonator. (a) Measured transmission spectrum through the fiber taper coupler around a typical WGM resonance. (b) Transmission spectrum (blue curve) of the same modes at a higher power typically used for Raman pumping, with significant thermal broadening. The red triangular waveform corresponds to the scanning of the pump laser wavelength; the left half corresponds to a decreasing pump wavelength while the right half corresponds to an increasing pump wavelength. The oscillation seen in the thermally broadened WGM is due to interference effect from reflection at fiber ends, which is unrelated to the WGM resonance.

4.3.3. Raman Spectra of a Bare Silica Microsphere

We first excited Raman scattering in a bare silica microsphere to characterize the effect of WGM resonance on silica Raman scattering. **Figure 4.7** presents the observed Raman emission from the silica microsphere with pump light on resonance with a WGM. The spectrum consists of a broad background that corresponds to the Raman features of bulk silica, as well as numerous sharp peaks. These sharp peaks are the result of the modified density of states from WGM resonance (*i.e.* the Purcell effect); each of these peaks corresponds to a WGM of the microsphere resonator, with a periodicity that agrees with the calculated free spectral range. Due to slight eccentricity of the microsphere, we have eccentricity-induced splitting and the WGMs appear in several "groups" of closely spaced modes.[32] The WGM peaks correspond to the Raman emission from silica that is first emitted into the WGMs and then scattered to free space to be collected by the objective. On the other hand, the broad background corresponds to the Raman emission that is not coupled to WGMs but instead emitted directly into free space. As a result, there is a notable spatial variation in the Raman emission from the silica microsphere, as shown in **Figure 4.8**; the WGM peaks are much more prominent at the two edges of the resonator than at the center of the resonator, indicating that these peaks correspond to the light lost from the WGMs due to the perturbed total internal reflection from the curvature of the microsphere. Also, this emission pattern indicates that the emission from the two sides of the resonator is approximately equal. This confirms that Raman scattering has equal intensity in the forward scattering and backward scattering directions.

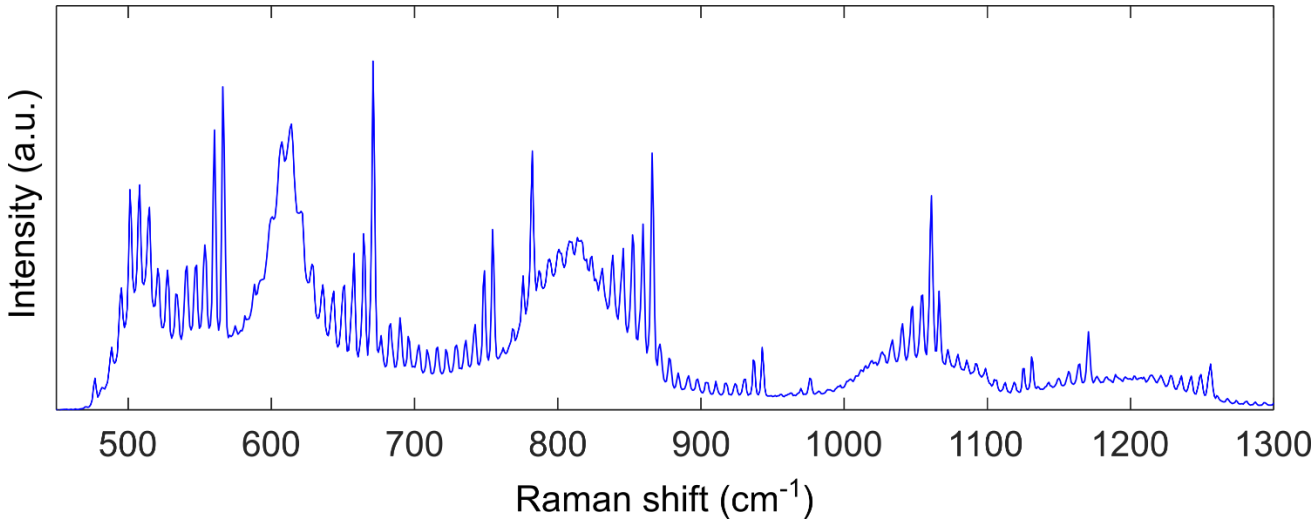

Figure 4.7. Integrated Raman spectrum from a 13.8 μm diameter bare silica microsphere.

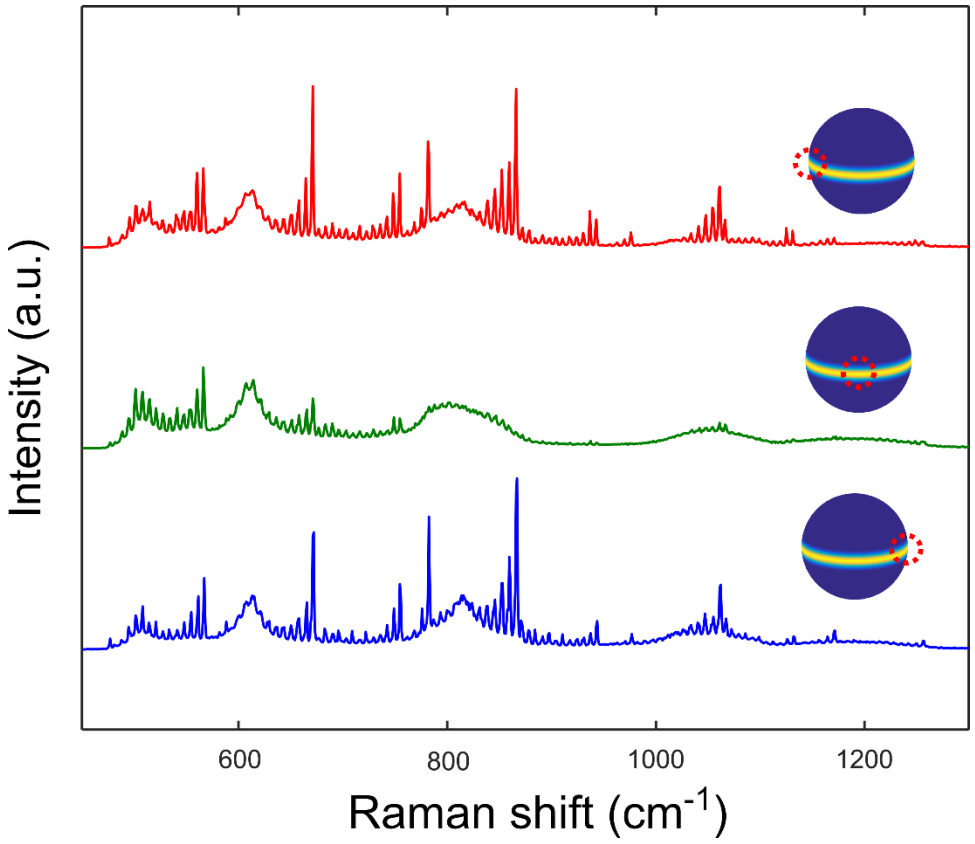

Figure 4.8. Raman spectra from different positions in the microsphere. The red dotted circles in the inset indicate the positions from which the spectra were collected.

With this silica microsphere resonator, we have investigated the dependence of Raman intensity on the wavelength detuning of the pump from a resonance (**Figure 4.9**). There is a large enhancement in the collected Raman signal when the pump is on-resonance with a WGM. This enhancement can be mostly attributed to the power enhancement of the pump light in the resonator. At critical coupling, the power enhancement is[144]

$$B = \frac{P_{cavity}}{P_{incident}} = \frac{1}{2\pi}\frac{\Delta\lambda_{FSR}}{\Delta\lambda_{FWHM}}\frac{1}{1+\left(\frac{\Delta\lambda}{\Delta\lambda_{FWHM}}\right)^2} \quad (4.1)$$

where $\Delta\lambda$ is the wavelength detuning of the pump light, $\Delta\lambda_{FSR}$ is the free spectral range of the optical cavity and $\Delta\lambda_{\mathrm{FWHM}}$ is the linewidth of the optical mode. For the resonator that we used, we have $\Delta\lambda_{FSR} = 10.5$ nm and $\Delta\lambda_{\mathrm{FWHM}} = 0.12$ pm, resulting in $B = 1.4 \times 10^4$ at zero detuning. To compare this value to the one obtained in our experiment, we note that at the detuning of $\Delta\lambda = \left(\frac{1}{2\pi}\Delta\lambda_{\mathrm{FWHM}}\Delta\lambda_{FSR}\right)^{\frac{1}{2}} = 0.014\ nm$ we have $P_{cavity} = P_{incident}$. Thus, by taking the ratio of the peak Raman intensity at zero-detuning and at 0.014 nm detuning, we obtain the experimentally measured Raman enhancement to be 4.9×10^3, in good agreement with the theoretically predicted value. The discrepancy between the two can be attributed to the non-ideal pumping at zero detuning and the contribution of background light in the Raman spectra for detuned pump, where the Raman signal is very low.

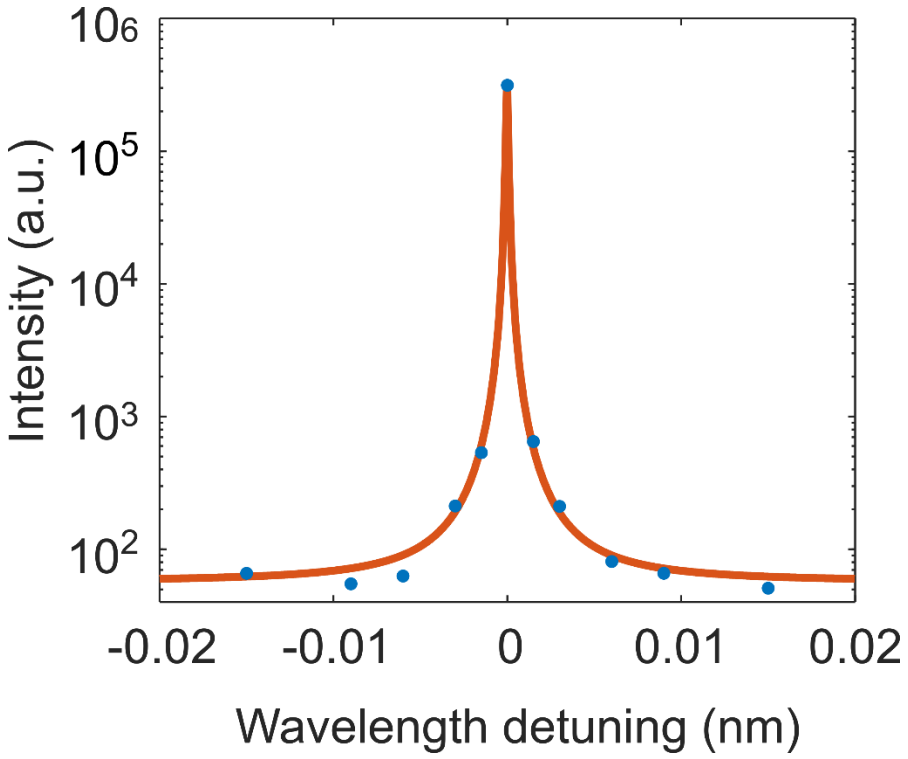

Figure 4.9. Measured Raman intensity dependence on pump detuning. The red curve shows a Lorentzian fit to the experimental data.

In calculating the theoretical enhancement factor above, we have ignored the contribution from the Purcell effect, which clearly modifies the Raman spectrum and causes the sharp peaks to appear. Since the Raman spectrum of silica is very broad and spans over several free spectral ranges, we expect little enhancement in the total power of the emitted Stokes light due to the Purcell effect.[7,139] However, within the linewidth of a particular WGM, the Purcell enhancement in the Raman spectral density is significant. The enhancement in Raman spectral density can be estimated by integrating the background-subtracted intensity within a WGM peak, dividing it by the linewidth of the WGM, and comparing the result to the silica background Raman intensity. It is important to note here that the width of WGM peaks in the Raman spectrum is limited by the

spectrometer and is not the true linewidth; instead, we assume the linewidth of the Stokes WGM to be the same as the pump mode, at $\Delta\lambda_{\mathrm{FWHM}} = 0.12\ pm$. From this, we estimate the spectral density enhancement within a WGM due to the Purcell effect to be 6.8×10^3.

4.3.4. Raman Spectrum of a Rhodamine 6G Coated Silica Microsphere

Next, we studied the enhancement of Raman signal from Rhodamine 6G molecules coated on the surface of a silica microsphere. We compared the Raman spectra from rhodamine 6G excited in three different ways. The first is the excitation of rhodamine 6G on a microsphere that is resonantly pumped through a tapered fiber coupler, as described previously for the bare silica microsphere. The second is the excitation of rhodamine 6G on the substrate near the microsphere with a free-space Gaussian beam, with an estimated beam diameter of 7 μm. This measurement serves as a control where no Raman enhancement due to the microsphere is present. The third is the free-space beam excitation of the rhodamine 6G on the microsphere, which serves as a comparison to previously published results on microsphere-based Raman enhancement with conventional micro-Raman setups.[123–127] The excitation beam is directed onto the rhodamine 6G coated microsphere from the top in this third case.

The observed Raman spectra for rhodamine 6G on the microsphere is presented in **Figure 4.10**. Another microsphere with a diameter of 17.3 μm was used for this measurement. The pump wavelength was 769 nm for pumping with tapered fiber coupler and 770 nm for free-space pumping. The modified Raman emission due to the Purcell effect is only visible for the microsphere pumped by the fiber taper. This can be attributed to the higher WGM coupling efficiency from the tapered fiber pumping; the Stokes light only couples to a WGM when the Raman scatterer has spatial overlap with the Stokes WGM, and this coupling is more efficient when the pump light is also in a WGM. For the peak at 1510 cm^{-1}, there are two sharp peaks

from tapered fiber pumping, but only one broad peak, which corresponds to the bulk Raman spectrum, from free-space pumping of the microsphere or the substrate. This can be attributed to the modified Raman emission in the presence of optical cavity; two WGMs overlap with the Raman peak at 1510 cm^{-1}, and there is a selective enhancement of Raman scattering at the resonance wavelengths of these two WGMs, leading to what looks like two peaks. By comparing the integrated area of the rhodamine 6G peak at 1510 cm^{-1} over a spectral band of 24 cm^{-1}, we find the Raman intensity from tapered fiber pumped microsphere to be larger than the Raman intensity from rhodamine 6G on the substrate by a factor of 928. Similarly, we find the Raman intensity for free-space pumped microsphere to be 7 times larger than the Raman intensity from rhodamine 6G on the substrate, which is in agreement with previously published results.[122–125] Free-space pumping is expected to have little coupling to WGMs, and the enhancement in Raman intensity from free-space pumping of the microsphere is expected to be mostly due to the photonic nanojet effect. Our results clearly show that the enhancement from WGMs can be much higher than that from photonic nanojet.

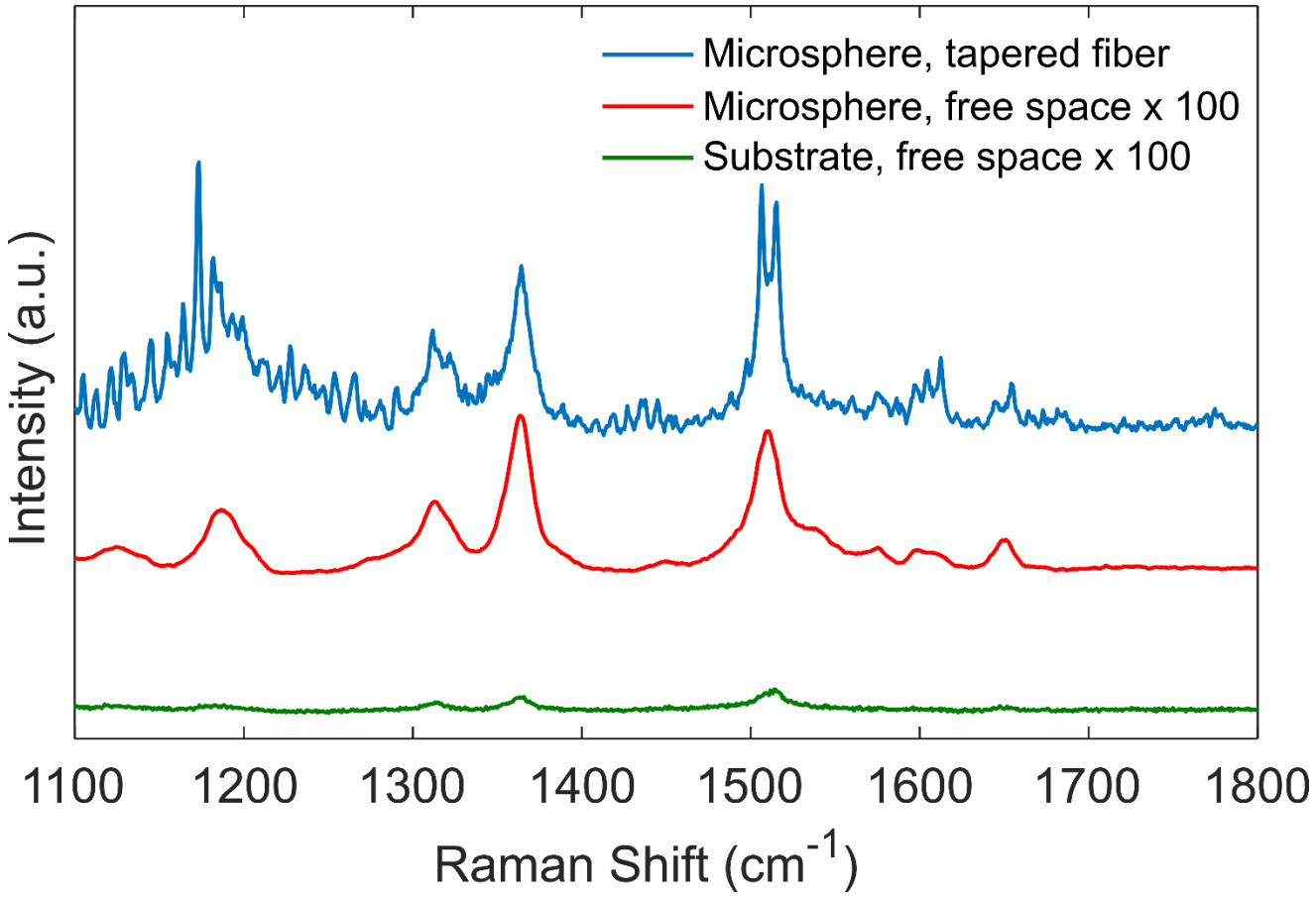

Figure 4.10. Raman enhancement of rhodamine 6G through the silica microsphere. The curves correspond to background subtracted Raman spectra of rhodamine 6G for tapered fiber coupler excitation (blue), free-space excitation on a microsphere (red), and free-space excitation on the substrate (green). The spectra for free-space excitation on the microsphere and substrate are scaled by 100 times for visibility.

4.4. Theoretical Estimate of Raman Enhancement from Microsphere

From the spectra in **Figure 4.10**, we can identify two mechanisms for the Raman enhancement: the pump enhancement which uniformly increases the Raman intensity at all Stokes wavelengths and the Purcell enhancement which results in enhancement at Stokes wavelengths matching

WGMs only, resulting in Raman spectra modified by sharp resonance peaks. The total Raman enhancement can be approximated as $F_{total} = F_{pump} \times (1 + F_{Purcell})$. This is analogous to the electromagnetic mechanism in SERS, in which, approximately a factor of $[|E_{local}(\omega_{pump})|/|E_0(\omega_{pump})|]^2$ is attributed to pump enhancement and another factor of $[|E_{local}(\omega_{Stokes})|/|E_0(\omega_{Stokes})|]^2$ is attributed to radiation enhancement resulting in a total of $[|E_{local}(\omega_{pump})|/|E_0(\omega_{pump})|]^4$ enhancement when the Stokes shift is small.[117,119] In what follows we consider these two enhancement mechanisms in silica microsphere separately and provide a theoretical estimate of the enhancement factors due to each mechanism. We follow the theoretical analysis in recent works on the Purcell enhanced Raman scattering in Fabry-Perot optical microcavities.[145–148]

4.4.1. Pump Enhancement Factor

The pump enhancement factor for molecules adsorbed on the surface of a microsphere can be calculated from the power enhancement factor discussed previously, with correction terms that account for the local electric field strength at the surface of the microsphere, the thickness of rhodamine 6G on the microsphere and that on the substrate, and the reduced pump efficiency due to laser scanning. In the pump enhancement factor (F_{pump}), we include these factors that affect the effective pump intensity leading to a spectrally uniform scaling of the Raman intensity, *i.e.* the factors that do not distort the shape of the original spectrum. In what follows in this section these factors will be discussed in more details.

For a single Raman scatterer, the power of the Raman scattered light can be expressed as $P_{Raman} = \sigma_{Raman} S_{local}$, where σ_{Raman} is the Raman cross section and S_{local} is the local power density [149]. Note that here we consider the "total" Raman cross section instead of the differential

Raman cross-section and ignore its direction-dependence for simplicity. For multiple scatterers, the total Raman scattered power is the sum of the scattered power from each. For our experiment with rhodamine 6G, we have $P_{Raman} = \rho_N \sigma_{Raman} \int_{R6G} S_{local} dV$, where ρ_N is the number density of rhodamine 6G molecules and the integration is on the volume of rhodamine 6G only. In the case of WGM pumping of the microsphere, the integral $\int_{R6G} S_{local} dV$ can be written as $\int_{R6G} S_{local} dV = \frac{V_{R6G,WGM}}{A_{WGM}} P_{in} \frac{1}{2\pi} \frac{\Delta\lambda_{FSR}}{\Delta\lambda_{FWHM}} \eta_{pump}$, where $V_{R6G,WGM} = \int_{R6G} \frac{\epsilon_p(\mathbf{r})|E_p(\mathbf{r})|^2}{\max(\epsilon_p(\mathbf{r})|E_p(\mathbf{r})|^2)} d^3\mathbf{r}$, with the integral on the volume of rhodamine 6G only, $A_{WGM} = \int \frac{\epsilon_p(\mathbf{r})|E_p(\mathbf{r})|^2}{\max(\epsilon_p(\mathbf{r})|E_p(\mathbf{r})|^2)} d^2\mathbf{r}$, with the integral on the cross section of the WGM in the microsphere, P_{in} is the incident power, the factor $\frac{1}{2\pi} \frac{\Delta\lambda_{FSR}}{\Delta\lambda_{FWHM}}$ is the power enhancement factor from resonance at zero detuning and critical coupling, and the factor η_{pump} accounts for the time dependent detuning of the scanning laser. Thus we obtain $P_{Raman,WGM} = \rho_N \sigma_{Raman} \frac{V_{R6G,WGM}}{A_{WGM}} P_{in} \frac{1}{2\pi} \frac{\Delta\lambda_{FSR}}{\Delta\lambda_{FWHM}} \eta_{pump}$. Note that the product $\rho_N V_{R6G,WGM}$ can be considered as the effective number of molecules excited by the WGM and we use this term later to compare the number of molecules excited by WGM pumping and free-space pumping.

For free-space pumping, we start from $P_{Raman} = \rho_N \sigma_{Raman} \int_{R6G} S_{local} dV$ again but use the free-space beam profile for S_{local}, assuming a Gaussian beam profile for the free-space pump light. We obtain $P_{Raman,fs} = \rho_N \sigma_{Raman} \frac{V_{R6G,fs}}{A_{fs}} P_{in}$, where $A_{fs} = \int \frac{\epsilon(\boldsymbol{r})|E(\boldsymbol{r})|^2}{\max(\epsilon(\boldsymbol{r})|E(\boldsymbol{r})|^2)} d^2\boldsymbol{r}$ at the beam waist and $V_{R6G,fs} = tA_{fs}$, t being the thickness of the rhodamine 6G film on the substrate. Note

that the ratio $\frac{V_{R6G,fs}}{A_{fs}}$ is simply t but we write in this form to compare to the result from WGM pumping of the microsphere.

The pump enhancement factor (F_{pump}) is the ratio between the collected Raman-scattered light intensity with WGM pumping to that with free-space pumping, without considering the Purcell effect. From the result above, ignoring the difference in collection efficiency between WGM pumping and free-space pumping, this ratio can be written as

$$F_{pump} = \frac{P_{Raman,WGM}}{P_{Raman,fs}}$$

$$= \frac{V_{R6G,WGM}}{V_{R6G,fs}} \frac{A_{fs}}{A_{WGM}} \frac{1}{2\pi} \frac{\Delta\lambda_{FSR}}{\Delta\lambda_{FWHM}} \eta_{pump} \quad (4.2)$$

For the silica microsphere that we used to collect the rhodamine 6G Raman spectrum, we have D = 17.3 μm, λ_{pump} = 769.30 nm, and n = 1.45. By considering the resonator to be a perfect sphere (ignoring eccentricity) and using the analytical equation for spherical resonators, we identify that the pump mode corresponds to a TE mode with mode numbers n = 1, l = 95, and m = 95, where n, l, and m are the radial, polar, and azimuthal mode number respectively. This mode has a mode volume of 42.5 μm^3 and a mode cross-section of $A_{WGM} = 0.817$ μm^2.[150] By considering the rhodamine 6G coverage to be a 3.4 nm thin film on the microsphere surface, we estimate the effective volume of rhodamine 6G to be $V_{R6G,WGM} = 0.056\ \mu m^3$. The free spectral range for this microsphere at the pump wavelength was calculated as $\Delta\lambda_{FSR} = \frac{\lambda_{pump}^2 \tan^{-1}(n^2-1)^{1/2}}{2\pi R(n^2-1)^{1/2}} = 8.4$ nm.[7] The linewidth was measured experimentally to be $\Delta\lambda_{FWHM} = 0.18\ pm$, which corresponds to Q = 4.3 x 10^6.

The term η_{pump} was estimated by monitoring the transmission through the tapered fiber coupler. η_{pump} was calculated as $\eta_{pump} = 1 - \frac{1}{T}\int_{t=0}^{t=T} \frac{P_{coupeld}}{P_{uncoupled}} dt$, where $P_{uncoupled}$ is the transmitted power through tapered fiber coupler without the microsphere coupled, and $\frac{1}{T}\int_{t=0}^{t=T} P_{coupled}\, dt$ is the time averaged transmission through the tapered fiber coupler with the microsphere at critical coupling, as the pump laser wavelength is scanned with a triangle wave with period T. This factor represents the fraction of incident power coupled into the microsphere on average, and it accounts for the changing wavelength detuning as the pump laser is scanned across the resonance mode, as well as any thermal shift in the resonance mode that changes the detuning. To demonstrate the validity of using η_{pump} as a correction factor, we recorded several different Raman spectra as we change the wavelength scan range of the pump laser, which leads to different η_{pump}. The emitted Raman intensity was proportional to η_{pump} as expected (**Figure 4.11**).

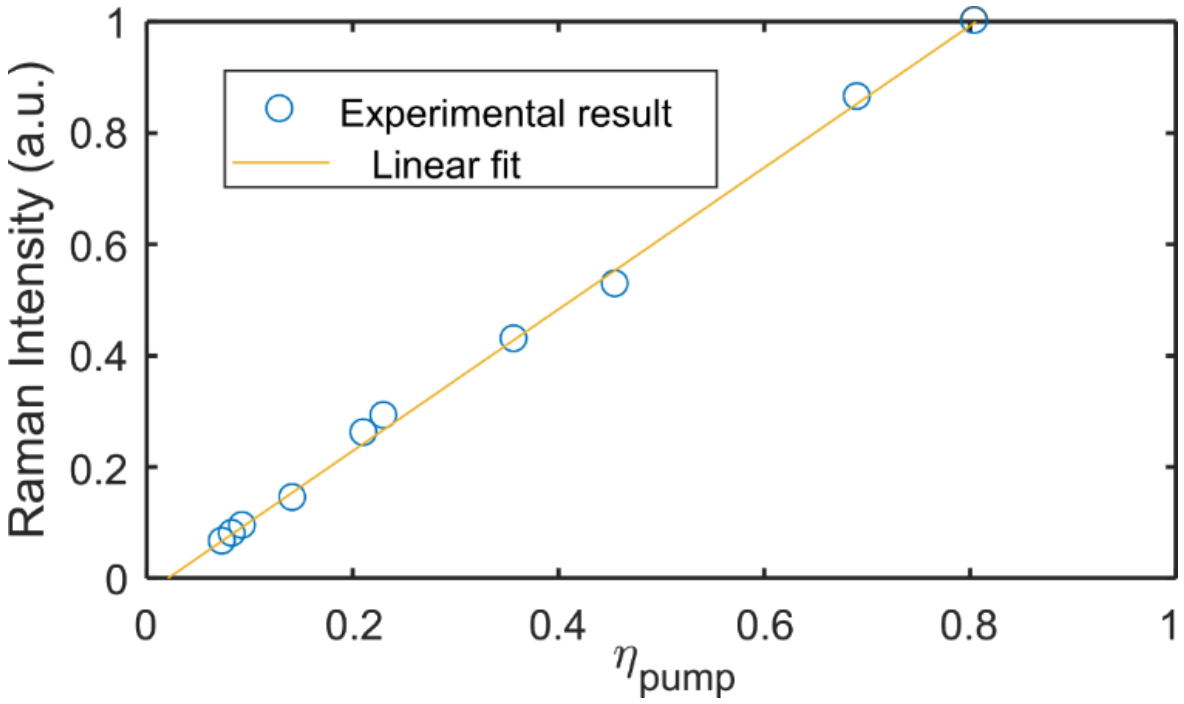

Figure 4.11. Dependence of Raman intensity on η_{pump}. The wavelength scanning range of the pump laser was changed to obtain different η_{pump}.

For free-space pumping, the pump beam waist size was estimated to be w_0 = 3.5 μm in radius. This results in an effective excitation area of $A_{fs} = \frac{1}{2}\pi w_0^2 = 20\ \mu m^2$. The effective excitation volume is found from $V_{R6G,fs} = A_{fs} \times t$, where t = 200 nm is the estimated thickness of rhodamine 6G film on the substrate, resulting in $V_{R6G,fs} = 4\ \mu m^3$. Note that in calculating the Raman scattered light intensity we take the ratio $\frac{V_{R6G,fs}}{A_{fs}}$ and A_{fs} cancels out from the final expression; thus an accurate estimation of the beam size is not important in the final result.

From our experiment with the Raman spectrum shown in **Figure 4.10**, we obtained $V_{R6G,WGM} = 0.056\ \mu m^3$, $V_{R6G,fs} = 4\ \mu m^3$, $A_{WGM} = 0.817\ \mu m^2$, $A_{fs} = 20\ \mu m^2$, $\Delta\lambda_{FSR} = 8.4$ nm, $\Delta\lambda_{\mathrm{FWHM}} = 0.18\ pm$, and $\eta_{pump} = 0.47$. This results in $F_{pump} = 1204$.

4.4.2. Purcell Enhancement Factor

In addition to pump enhancement, Raman emission is also enhanced by the increased density of state due to resonance, characterized by the Purcell factor. Whereas the pump enhancement results in a uniform enhancement of the entire Raman spectrum, the Purcell enhancement only enhances the Raman spectral density within the linewidth of a WGM and thus is highly non-uniform, introducing sharp peaks in the Raman spectra. The Purcell enhancement factor, however, is calculated for the enhancement of total Raman intensity for a particular Raman peak, and thus is much smaller than the enhancement of Raman spectral density within each WGM linewidth. The ideal Purcell factor is often written as $F_{Purcell,0} = \frac{3}{4\pi^2}\lambda_s^3\frac{Q_c}{V_s}$, where Q_c is the cavity Q factor and V_s is the mode volume of the Stokes WGM.[151,152] However, there are several corrections required in applying this Purcell factor to our experiment, and these correction factors will be discussed in detail in this subsection.

The Purcell factor, in its most simplified form, is often written as $C = \frac{3}{4\pi^2}\lambda_s^3\frac{Q_s}{V_s}$, where λ_s, Q_s, and V_s are the resonance wavelength, Q factor, and mode volume of the Stokes WGM. When written this way, the Purcell factor represents the ratio of the emission rate into an optical cavity with unity refractive index to the emission ratio into free space. In our experiment, we need to compare the emission into a WGM with effective index n to the emission into free space and this results in an additional factor of $\frac{1}{n^2}$ from the dependence of emitter-field coupling on refractive

index of the medium.[153] Throughout our work, the refractive index of silica was taken to be 1.45 and the effective index of the WGMs were taken as equal to the bulk refractive index of silica as an approximation.

For an emitter with emission linewidth comparable or larger than the linewidth of the cavity resonance, the Purcell factor no longer depends only on the *Q*-factor of the cavity resonance, but rather it depends on both the cavity linewidth and the linewidth of the emission peak.[145] In the case of Raman scattering, the expression for the Purcell factor is modified by replacing Q_s with Q_{eff}, where Q_{eff} is defined as $Q_{eff} = \frac{Q_s Q_R}{Q_s + Q_R}$. Here Q_s is the *Q*- factor of the Stokes WGM and $Q_R = \frac{\lambda_s}{\Delta\lambda_R}$, where $\Delta\lambda_R$ is the linewidth of the Raman peak. When the linewidth of the Raman peak is much larger than the linewidth of cavity resonance, as in our case, Q_{eff} is well approximated by Q_R. From the measured spectrum, we find that the linewidth of the 1510 cm^{-1} peak, appearing at $\lambda_s = 870\ nm$, is $\Delta\lambda_R = 1.36\ nm$. Thus, we obtain $Q_{eff} = 640$.

The mode volume of the WGM was calculated from analytical expressions. There were two WGMs observed to overlap with the Raman peak at 1510 cm^{-1}, observed at $\lambda_s = 870\ nm$. The exact mode numbers of these two WGMs are not clear. However, for a spherical resonator with R = 8.65 μm and n = 1.45, an optical mode with mode numbers *n* =1, *l* = 83, and *m* = 83 and TE polarization exists at 874.35 nm and we assume that this mode at 874.35 nm well approximates the spatial distribution and mode volume of both observed WGMs at 870 nm. The mode volume was calculated to be $V_s = 49.1\ \mu m^3$.[150]

η_E accounts for the reduced optical field strength at the surface of the microsphere (where the rhodamine 6G dyes are) compared with the maximum field strength within the silica

microsphere, as well as the spatial overlap between the pump WGM and the Stokes WGM. When there is a single emitter in the cavity not located at the maximum of the cavity field, the ideal Purcell factor is modified by $\frac{|E_S(\boldsymbol{r})|^2}{\max(|E_S(\boldsymbol{r})|^2)}$, where $E_s(\boldsymbol{r})$ is the electric field of the Stokes mode.[145,147] For multiple emitters at different locations with different pump power at each emitter, a weighted average of $\frac{|E_S(\boldsymbol{r})|^2}{\max(|E_S(\boldsymbol{r})|^2)}$ is taken, where the weight is the pump power at each emitter. Thus η_E can be obtained as $\eta_E = \frac{\int_{R6G}|E_p(\boldsymbol{r})|^2 \frac{|E_S(r)|^2}{\max(|E_S(r)|^2)} d^3\boldsymbol{r}}{\int_{R6G}|E_p(\boldsymbol{r})|^2 d^3\boldsymbol{r}}$, where E_p is the electric field of the pump mode and the integration is on the volume of rhodamine 6G only.[145] For the pump WGM with n =1, l = 95, and m = 95 at 769.10 nm and the Stokes WGM with n =1, l = 83, and m = 83 at 874.35 nm, we calculate η_E to be 0.1709.

η_λ accounts for any detuning between the Raman peak and the Stokes WGM, as well as more than one WGM overlapping with the Raman peak.[147] In calculating Q_{eff} we have assumed that there is exactly one WGM at the center of the Lorentzian Raman peak; any discrepancy between the experimental spectrum and this ideal case is accounted by η_λ. For a single WGM overlapping with the Raman peak, $\eta_\lambda$is equal to the intensity of the Raman peak at the WGM resonance wavelength relative to the maximum intensity of the Raman peak. For more than one overlapping WGMs, the sum of η_λ for each WGM is taken as the total η_λ. For the spectrum obtained in our experiment (**Figure 4.10**), the two WGMs are symmetrically located on the two sides of the Raman peak, with each of them contributing 0.79, and thus overall, $\eta_\lambda = 1.58$.

η_Ω accounts for the difference in the collection efficiencies between the Stokes light emitted directly into free space and the Stokes light emitted into a WGM and then scattered into free space. Although in both cases the Stokes light is collected with the same NA = 0.55 objective

lens, the collection efficiencies are different since these two emissions have different angular divergence. Light emitted directly into free space has a dipolar emission pattern, while the emission from WGMs are on the equatorial plane of the microsphere, tangential to the edge of the microsphere and with a small angular divergence in the polar direction. Since both the dipolar emission and the emission from WGMs are uniform over 2π radians in the azimuthal direction in the far field, for comparison we can ignore the azimuthal dependence and only consider the difference in emission pattern in the polar direction. For the emission from WGM, we approximate the angular divergence in the polar direction to be equal to that of a Gaussian beam with waist size equal to the size of the WGM cross section; we calculate the angular divergence to be 0.31 radians. The objective lens has NA = 0.55, corresponding to a collection angle of 0.58 radians. Thus, almost all the emission from WGM is collected by the objective. On the other hand, only 66% of the dipolar emission falls within the collection angle of the objective. Thus, η_Ω, defined as the ratio of the collection efficiency of the WGM emission to that of the dipolar emission, is calculated as 1/0.66 = 1.5.

Further, a factor of 2 goes into the expression for $F_{Purcell}$ due to the two-fold degeneracy of optical modes in the microsphere, from having both clockwise and counterclockwise modes. Another factor of 0.5 goes into the expression due to the coupling to the tapered fiber coupler; we assume critical coupling to the tapered fiber at Stokes wavelength, in which case half of the light emitted into the WGM is lost to the tapered fiber and the other half is emitted into free space (and a fraction of this light is collected by the objective).

By considering all the factors mentioned above, we obtain the Purcell enhancement in our experiment as:

$$F_{Purcell} = \frac{3}{4\pi^2}\frac{\lambda_s^3}{{n_s}^2}\frac{Q_{eff}}{V_s}\eta_\lambda\eta_E\eta_\Omega \times 2 \times 0.5 \quad (4.3)$$

We evaluate the Purcell enhancement factor for the Raman spectrum presented in **Figure 4.10**, with $\lambda_s = 0.8743\ \mu m$, $n_s = 1.45$, $Q_{eff} = 640$, $V_s = 49.1\ \mu m^3$, $\eta_\lambda = 1.58$, $\eta_E = 0.17$, and $\eta_\Omega = 1.5$ to obtain $F_{Purcell} = 0.127$.

4.4.3. Comparison to Experimental Results

To compare the theoretical results to the experiment, we performed curve fitting to the experimentally obtained Raman spectra to estimate the contribution of the Purcell enhancement in the total Raman enhancement. This is possible since the Purcell enhancement appears as sharp lines that are clearly distinguishable from the bulk Raman spectrum. However, to determine the Purcell enhancement accurately we need a Raman spectrum corresponding to only that of rhodamine 6G, without any background contribution from silica.

In order to obtain such a spectrum, we noted that as we pump the rhodamine 6G coated microsphere the Raman peaks of rhodamine 6G gradually decreased in intensity and eventually disappeared (**Figure 4.12**). With WGM pumping, this occurred even for a relatively small pump power of 37 μW. On the other hand, for free-space excitation, no such change in Raman intensity was observed even for pump power greater than 1 mW. We believe the decrease in Raman intensity is due to photobleaching, even though we are not pumping at the absorption peak of rhodamine 6G. This photobleaching effect was only observed for WGM pumping since pump enhancement due to WGM greatly increases the local pump power for the rhodamine 6G molecules. This photobleaching effect was used to obtain an accurate Raman spectrum corresponding to that of rhodamine 6G only (without silica Raman peaks) by taking the difference between the measured spectrum before and after photobleaching (**Figure 4.13**). This

method results in a more accurate removal of silica Raman scattering than background subtraction through curve fitting, which is crucial for an accurate estimation of the Raman enhancement factor.

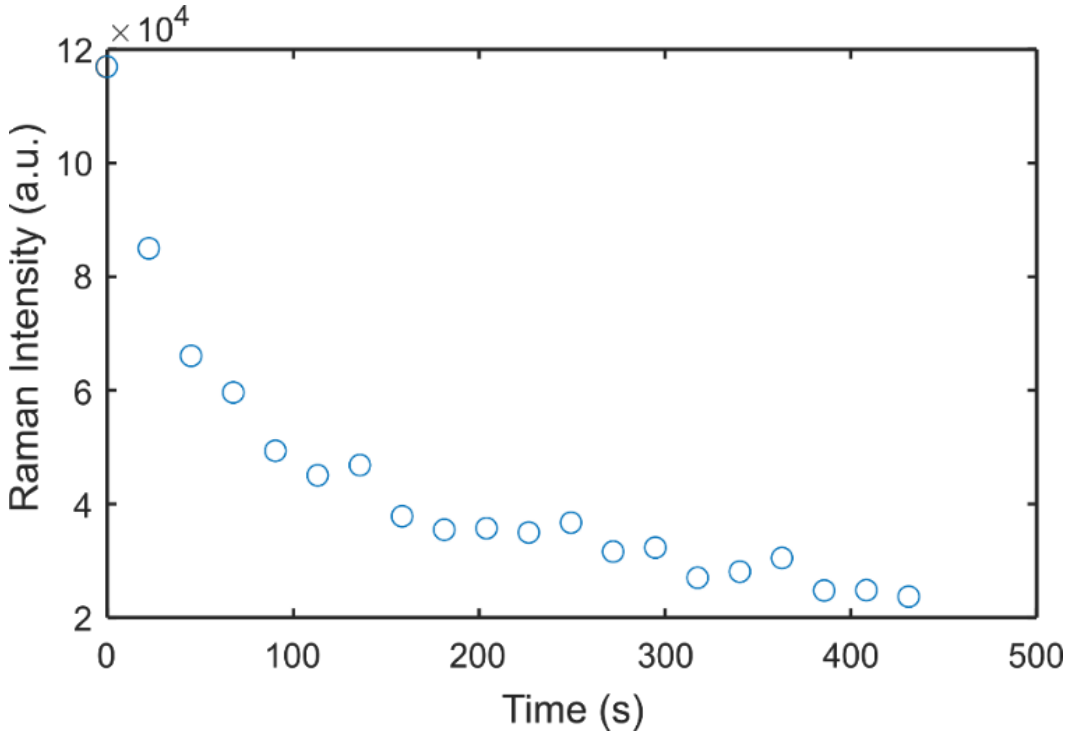

Figure 4.12. Change in Raman intensity as rhodamine 6G photobleaches. The pump power was 37 μW, coupled to the microsphere WGM through a tapered fiber.

This difference spectra between before and after photobleaching was used for curve fitting to determine the contribution of Purcell enhancement experimentally. In performing the curve fitting, the bulk Raman peak was assumed to have a Lorentzian lineshape, whereas the two WGMs have spectrometer-limited linewidth and were fitted with Gaussians. By comparing the integrated areas of the bulk Raman peak and the two WGM peaks, we estimated the Purcell

enhancement to be 0.134. This measured Purcell enhancement is in very good agreement with the theoretically calculated value of 0.127. Further, we can also calculate the experimentally measured F_{pump} to be 818. This is also in good agreement with the theoretically calculated value of 1204.

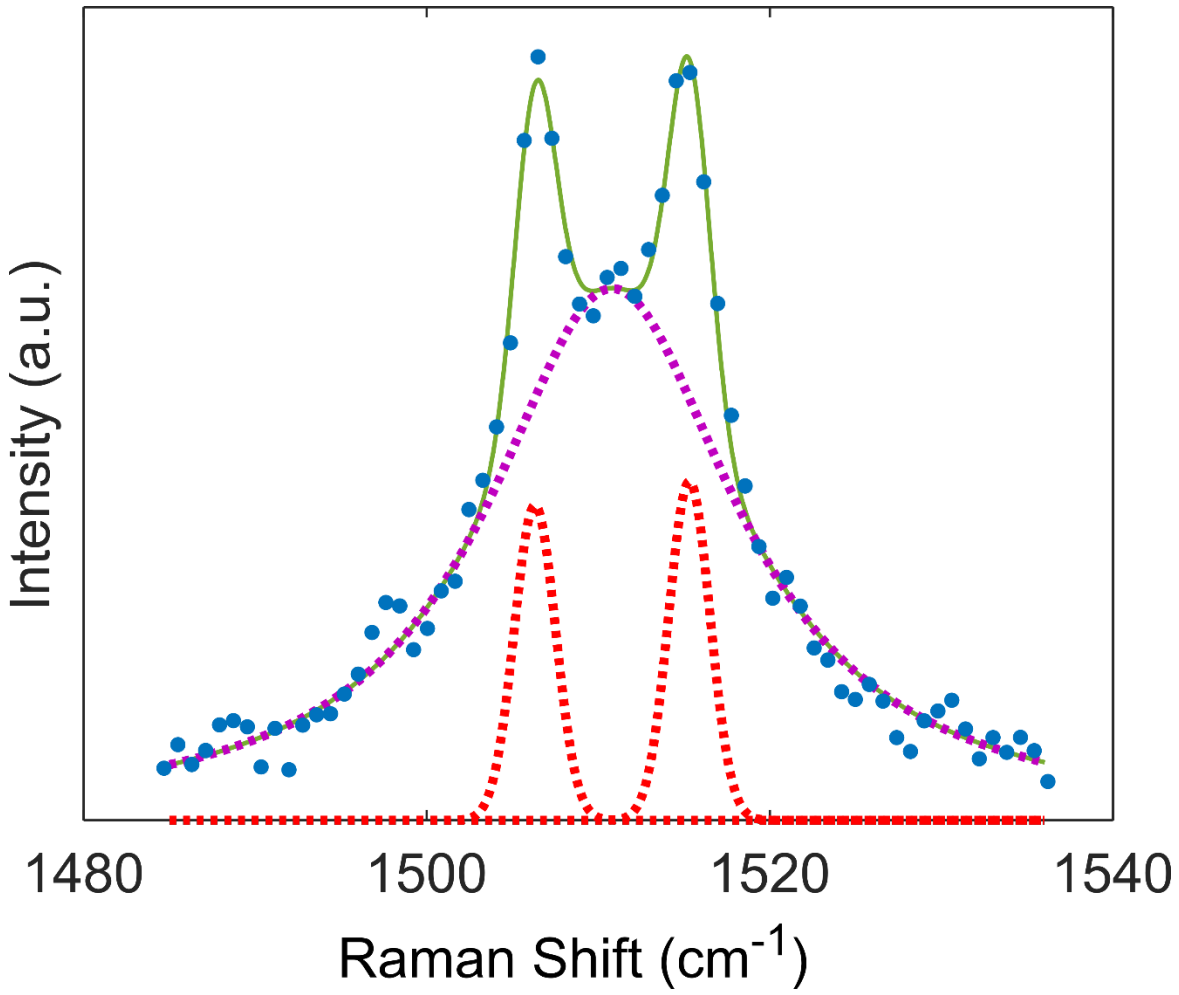

Figure 4.13. Raman spectrum of rhodamine 6G around the 1510 cm^{-1} peak, obtained by subtracting the spectrum after photobleaching from the spectrum before photobleaching. The solid green curve is a fit to the data points. The spectrum is fitted as sum of a Lorentzian Raman peak (purple dotted curve) and two Gaussian WGM peaks (red dotted curve).

4.4.4. Total Raman Enhancement Factor

Finally, the Raman enhancement factor of the silica microsphere as a SERS substrate is evaluated as

$$EF = \frac{I_{SERS}/N_{SERS}}{I_0/N_0} \tag{4.4}$$

where I_{SERS} and I_0 are the Raman signal intensity in the SERS and non-SERS spectra, and N_{SERS} and N_0 are the effective number of molecules being excited in the SERS and non-SERS measurement.[118] The ratio $\frac{N_{SERS}}{N_0}$ can be estimated by considering the effective volume of rhodamine 6G that is pumped in each case. We have defined $V_{R6G,WGM}$ and $V_{R6G,fs}$ previously to calculate the pump enhancement factor. These can be considered as the effective volume of rhodamine 6G being excited under each pumping scheme, with each differential volume of rhodamine 6G being normalized by the local pump power. $V_{R6G,WGM}$ and $V_{R6G,fs}$ corresponds to the volume of rhodamine 6G required at the electric field maximum that would result in the same Raman intensity as the actual experiment. However, for the case of WGM pumping, the field maximum used for normalization was the maximum in the entire WGM modal distribution, which is located inside the silica sphere and cannot be reached by rhodamine 6G molecules. To be realistic, here, we must instead normalize by the field maximum on the surface of the microsphere instead. Thus, the ratio $\frac{N_{SERS}}{N_0}$ can be obtained as

$$\frac{N_{SERS}}{N_0} = \frac{V_{R6G,WGM} \times \frac{max(|E_p(r)|^2)}{\underset{surface}{max}(|E_p(r)|^2)}}{V_{R6G,fs}} = 0.065 \tag{4.5}$$

For our experiment, $\frac{I_{SERS}}{I_0} = F_{total} = 928$ and the ratio $\frac{N_{SERS}}{N_0} = 0.065$, and we obtain EF = 1.4 × 10^4. Within this, a minor factor of 1.134 can be attributed to the Purcell enhancement, with the remaining 1.2 × 10^4 attributed to pump enhancement.

4.5. Conclusion

In conclusion, we have measured the enhanced Raman emission of silica and rhodamine 6G due to WGM resonances in silica microspheres. Our use of tapered fiber coupler allows us to couple pump light to the WGMs with high efficiency, leading to a higher enhancement factor than it is possible with free-space pumping. We estimated the Raman enhancement factor as 1.4 × 10^4, with most of the enhancement originating from the pump enhancement and a small factor of 1.134 from the Purcell enhancement. These experimentally measured results are in good agreement with theoretical calculations.

The experimentally observed Raman enhancement factor in this work is, to the best of our knowledge, the largest reported from dielectric microspheres so far, but still several orders lower than it is predicted in theory,[138,139] which can be as high as 10^8. The most important factor that leads to this smaller experimentally measured enhancement factor is the large linewidth of the rhodamine 6G Raman peak, with $\Delta\lambda_R = 18\ cm^{-1}$, compared with that of the Stokes WGM, with linewidth on the order of 0.01 cm^{-1}. Since the Raman peak linewidth is different for different molecules, this factor is often not included in theoretical calculations of the enhancement factor, making the enhancement factor predicted from theory larger than what is attainable for common Raman probes. On the other hand, for some gas phase molecules such as CO_2, the Raman peaks can be much narrower and comparable to WGMs in linewidth.[146] These molecules would result in a much larger enhancement factor from WGMs, predominantly due to an increase in Purcell

enhancement. Also, cavity resonance scanning techniques similar to those demonstrated for Fabry-Perot cavities may allow us to obtain a higher Purcell enhancement by scanning the Stokes WGM across the Raman peak.[146–148]

An interesting question to consider here is whether dielectric microspheres, as SERS substrates, have the potential to detect single-molecule Raman spectra. Despite earlier works that have taken single-molecule SERS as an indication for extremely high enhancement factors, it has been recently demonstrated that when Raman probes with large cross-section such as rhodamine 6G are pumped at their molecular resonance, a single-molecule EF as low as 10^6 is sufficient to observe single molecule SERS.[154] Considering this result, we believe that single-molecule SERS is attainable with dielectric microspheres with some optimization. First, we note that without any rhodamine 6G coating, Q factor above 10^7 is easily achievable with bare silica microspheres. For single-molecule studies, the perturbation to the WGM would be minimal and we don't expect any lowering of the Q factor from that of a bare silica microsphere. The increased Q factor alone would increase the EF by more than an order of magnitude. Also, for single molecules there is no inhomogeneous broadening,[155] leading to a narrower Raman peak and an increased Purcell enhancement from WGMs. Together with further optimization in the size and refractive index of the microsphere, we believe that a single-molecule EF of 10^6 is very realistic for dielectric microspheres supporting WGMs. Although challenges such as the suppression of Raman lasing remains, the demonstration of single-molecule SERS from dielectric microspheres would allow for the probing of molecular dynamics and interactions at previously unattainable level of details.

A unique advantage of our system, not fully exploited in this work, is the ability to quantitatively measure the number of molecules adsorbed onto the microsphere from resonance wavelength shift and collect the Raman spectra from the same molecules. Wavelength shift provides another

measurement of the number of molecules being excited, independent from Raman spectroscopy. This allows for a more accurate quantification of the enhanced Raman spectra. On the other hand, molecular identification through Raman spectroscopy adds otherwise unavailable specificity to the WGM sensing method. This combination of two detection methods can potentially be much more powerful in chemical and biological sensing compared with each method used alone.

Chapter 5: Future Outlook

This chapter describes on-going and possible future works on chemical and bio-sensing using WGM resonators. In particular, an on-going project on sensing small molecules with mesoporous silica WGM resonator is described in section 5.1 This work is still incomplete and what is presented here should be considered as a preliminary result. In section 5.2, possible future directions on WGM resonator sensing is discussed.

5.1. Mesoporous Silica WGM Resonator for Sensing Applications

5.1.1. Introduction

Whispering gallery mode microresonators have been demonstrated to be a sensitive platform for nanoparticle and biomolecule detection. However, due to the resonators sensitivity to various factors that can be considered as "noise", such as temperature and pressure drift, highly sensitive sensing has been limited to single-particle and single-molecule detection based on either step-changes or spikes in the resonance wavelength, for which slow drifts due to temperature can be ignored. For the measurement of a low concentration of small molecules over a relatively long period of time, thermal drift becomes comparable to the signal from the analyte, and this makes the reliable detection of an analyte difficult.

We can also consider the rather small active sensing area/volume of WGM resonator to be one of its limitation for sensing applications. In a typical WGM resonator, only a small portion of the circulating field interacts with an analyte bound on the surface of the resonator as evanescent field. Since typically the analyte can only adsorb on the external surface of the resonator, the number of binding sites can become a limiting factor for detection of small molecules at low

concentration. For hybrid WGM-plasmonic resonators,[3–5] although the plasmonic hot spot greatly enhances the field strength and sensitivity to any analyte at the hotspot, only analyte molecules at the small plasmonic hotspot can be detected and thus the active sensing volume is reduced even further. Such a system is well suited to study the kinetics of single-molecule interactions but is less suited to measure, for example, the total concentration of the analyte in the solution.

To overcome these limitations of WGM resonator sensors, we propose the use of mesoporous silica, instead of the typically used dense silica, as the building-material for WGM resonators. Mesoporous silica, in nanoparticle and thin film forms, has ordered, uniformly sized pores ranging from 2-50nm.[156,157] Due to their high surface area on the order of 1000 m^2/g and high pore volume up to 2.5 cm^3/g, popular mesoporous silica materials such as MCM-41 and SBA-15 has found wide applications in catalysis, drug delivery, and contaminant removal.[156–161] For optical applications, these materials have been doped with fluorescent molecules and were used as sensors as well as lasers.[162–165] Mesoporous silica is ideally suited as the building material for WGM resonator based sensors because of their high surface area and the possibility for the analyte to enter the resonator and interact with not only the evanescent field but also the stronger optical field inside the resonator.

5.1.2. Fabrication

The recipe for mesoporous silica sol-gel synthesis is adapted from Alberius *et al*.[166] Mesoporous silica is made from the surfactant templated self-assembly of the triblock copolymer Pluronic F127. 0.74g of Pluronic F127, 2.3g of ethanol, 1.08g of water with pH = 1, adjusted with HCl, and 2.08g of TEOS are mixed and stirred for 1h using a magnetic stirrer at room temperature. This sol is then aged for 1 days. After 1 day, the sol is dropped onto a piece of standard single

mode fiber (125 μm silica fiber, with the polymer jacket stripped) using a micropipette. The sol dries and condenses on the optical fiber, forming droplets in the shape of micro-bottle resonators. These micro-bottles are then calcined at 500°C for 5 h in a tube furnace, with 1°C/min ramp rate for the removal of templating surfactant. Note that there is significant cracking of the sol-gel silica upon calcination, and the yield on crack-free micro-bottle resonators is quite low. This is still a problem to be addressed.

5.1.3. Characterization

Optical Characterization

A microscope image of the mesoporous silica micro-bottle resonator in water is presented in **Figure 5.1**. In the air, it was observed that the resonance wavelength continuously fluctuates in the range of several hundred picometers, presumably due to the fluctuation of moisture in the air around the resonator. This high sensitivity of resonance modes to ambient humidity is an indication of the presence of mesopores in the micro-bottle, but nevertheless, this fluctuation makes stable measurement difficult in the air. When submerged in water, however, the WGMs become much more stable, and a typical transmission spectrum for this resonator is presented in **Figure 5.2**. Typical Q-factor for a mesoporous silica micro-bottle resonator in water is around $Q = 10^5 \sim 10^6$, which is not much lower than that of a dense silica bottle-resonator made by tapering optical fiber. This suggests that the mesopores are small enough that they do not significantly increase the intrinsic loss of the resonator by scattering.

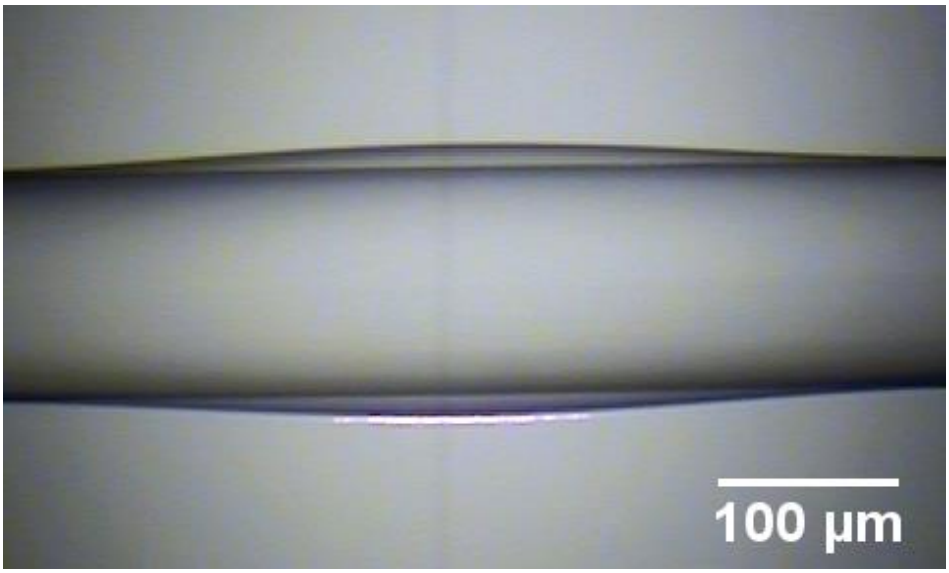

Figure 5.1. Optical micrograph of mesoporous silica micro-bottle resonator in water. The red light visible at the bottom corresponds to that from a WGM supported in the bottle resonator.

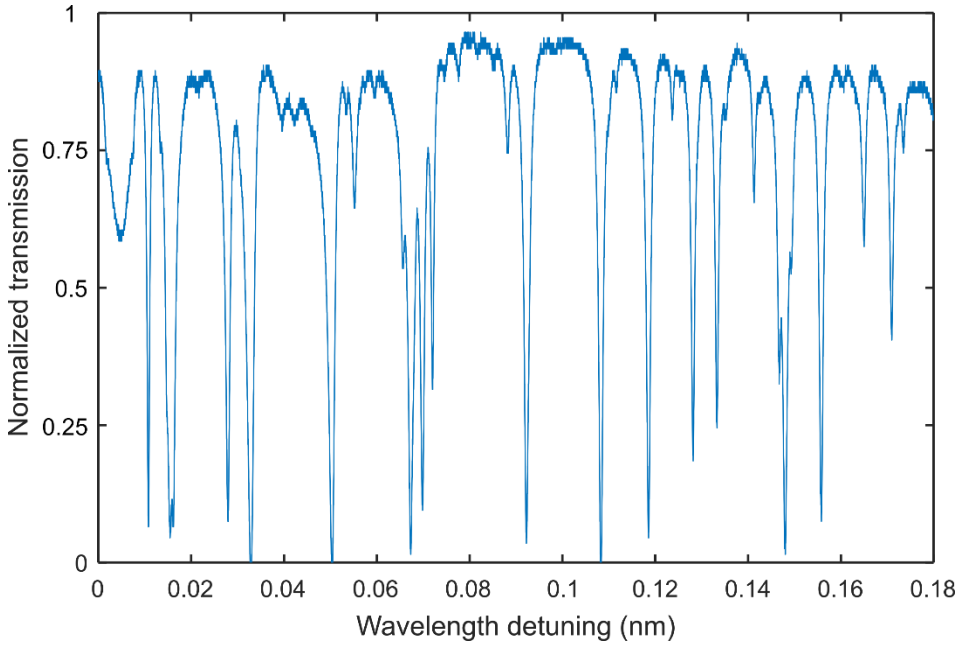

Figure 5.2. Typical transmission spectrum for a mesoporous silica micro-bottle resonator in water, showing numerous WGMs in the scanned range.

STEM

Scanning transmission electron microscopy (STEM) images of the mesoporous silica were taken by spin-coating the same sol-gel on a silicon wafer and scraping the mesoporous silica off by a razer blade after calcination. These STEM images are presented in **Figure 5.3**. From the STEM images, the presence of mesopores with pore size around 8 nm is visible.

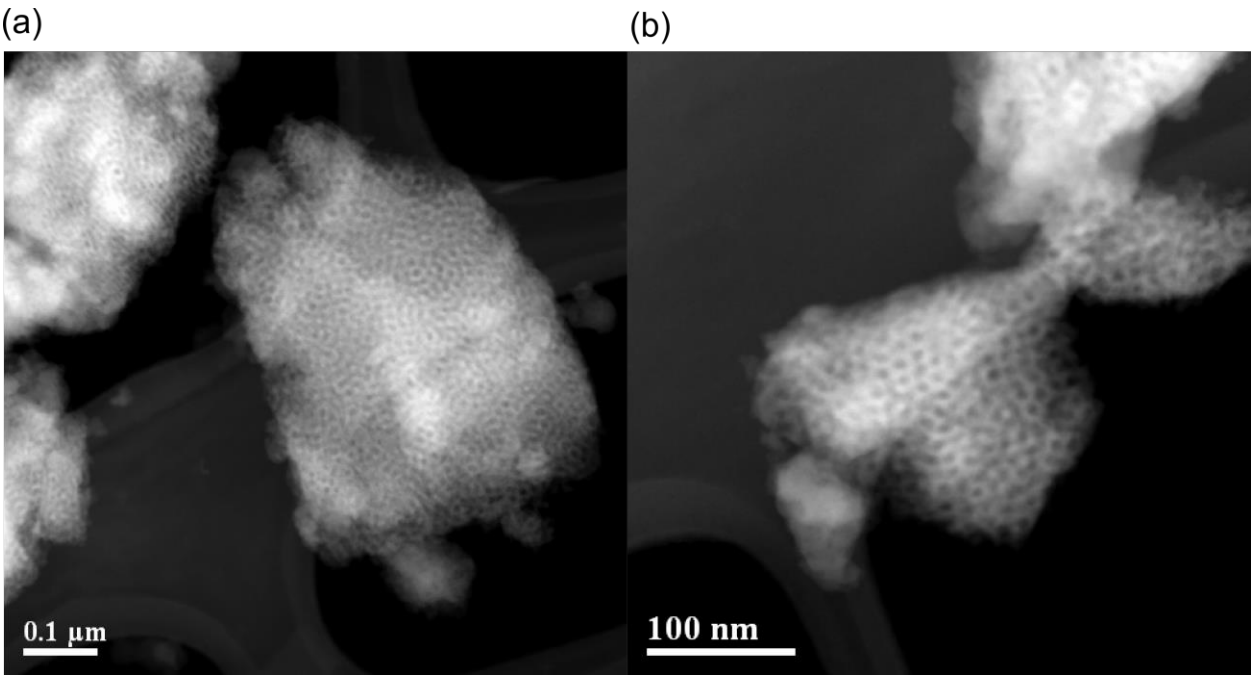

Figure 5.3. STEM images of mesoporous silica

Ellipsometry

Ellipsometry measurement of the mesoporous silica thin film spin-coated on a silicon wafer is presented in **Figure 5.4**. The result was fitted with Bruggeman effective media approximation

model based on a mixture of silica and void. From this model, a void fraction of 28.8% was obtained, corresponding to the volume of mesopores.

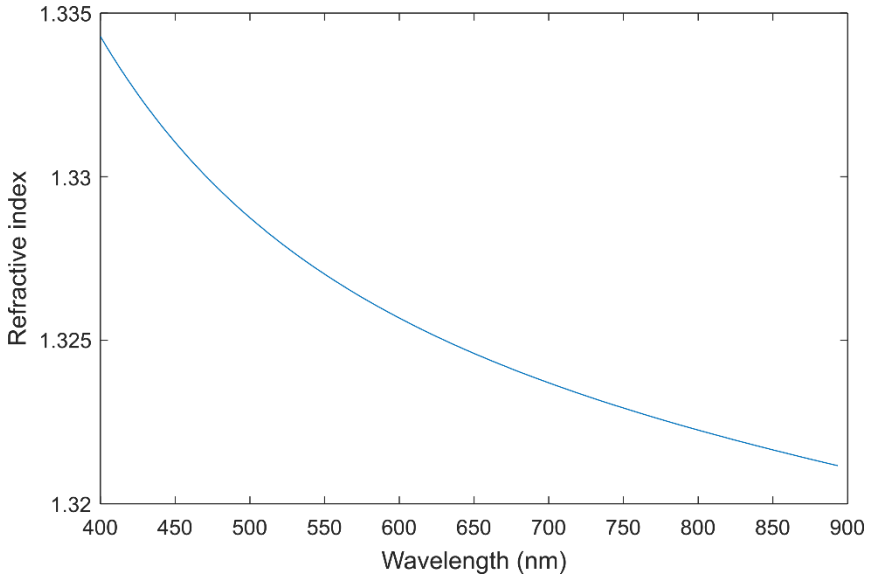

Figure 5.4. Measurement of refractive index of mesoporous silica through ellipsometry.

5.1.4. Sensing using Mesoporous Silica Micro-Bottle Resonator

To demonstrate the sensing capability of mesoporous silica bottle resonator, the resonator was immersed in 400 µL of distilled water and the transmission spectrum of the resonator was continuously monitored at $\lambda = 770nm$, with 0.18 nm scanning range. After 500 s of measurement in distilled water, 100 µL of 30 µM basic fuchsin in DI water was added to the measurement chamber through micropipette and gently mixed. Basic fuchsin was chosen as a model molecule to study the resonance shift because it is a small molecule that can diffuse into the mesopores, it is a cationic dye that binds well to silica surface, and it has a bright red color which can be seen easily through microscope. The ensuing shift in resonance wavelength was

monitored until 9000s. At the same time, the resonator was imaged using an optical microscope to monitor its staining by the fuchsin dye. The result is presented in **Figure 5.5**.

From **Figure 5.5**, we note that there is a large wavelength shift exceeding 1 nm. Such large shift is much more than it is expected from a regular, dense silica WGM resonator and is thought to be due to the large surface area of mesoporous silica. However, the overall shift is very slow; even after 9000s, the shift has not saturated yet. Such slow adsorption rate for mesoporous silica has been reported from drug loading and release studies,[167] but a slow adsorption rate is not ideal for sensing applications where we want a fast sensor response. From the microscope images, it is evident that there is a significant staining of mesoporous silica by the fuchsin dye as the experiment progresses. We note that the solution surrounding the resonator contains fuchsin dye as well, but the resonator is colored much more than the surrounding, suggesting that mesoporous silica can concentrate the analyte on the resonator by surface adsorption. For a regular, dense silica WGM resonator such staining is not visible at all, and the capability to concentrate the analyte beyond its level in solution is a clear advantage of using mesoporous silica resonator.

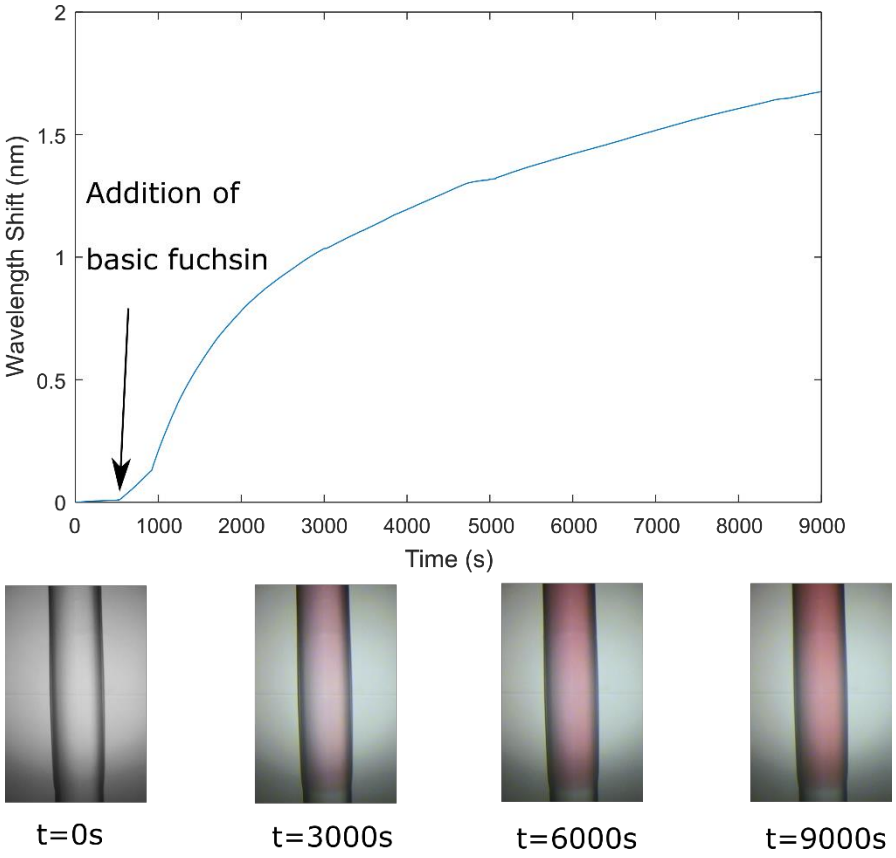

Figure 5.5. Resonance shift of mesoporous silica micro-bottle resonator upon the addition of 30 μM basic fuchsin. The four microscope images at the bottom are the images of the micro-bottle resonator at different times. The gradual staining of mesoporous silica by the red fuchsin dye is clear from these images.

5.1.5. Current Challenges

Although we have demonstrated the fabrication of mesoporous silica micro-bottle resonator with excellent optical qualities, there are still several challenges for its use in sensing applications. First, as discussed previously, there is significant cracking of the resonator during calcination, which leads to low yield. Lowering the calcination temperature to, for example, 200°C, prevents much of this cracking, but this results in the incomplete removal of the surfactant template. For

resonators fabricated with lower calcination temperature, a continuous blue-shift in the resonance spectrum was observed when the resonator was immersed in water; this may be due to the dissolution of the remaining surfactant into water. Thus, an optimization of the fabrication process is still required. Also, the slow rate of analyte adsorption and loading into the mesoporous silica is another problem. This may be related to the pore accessibility from outside and pore interconnectivity inside mesoporous silica. Indeed, it was noted with dye staining experiment that sometimes, the dye staining starts from the two edges of the micro-bottle (where the micro-bottle is the thinnest) and gradually move towards the center. Such non-uniform staining pattern suggests that different part of the micro-bottle may have different pore accessibility. This problem can potentially be solved by changing the sol-gel recipe; the pore structure is dictated by the amount of Pluronic F127 surfactant. Otherwise, we may be able to use the initial slope of the resonance mode shift as the sensing signal instead of waiting for the resonance shift to saturate.

5.2. Prospects on WGM Resonator Sensing

In the past two decades, researchers had made impressive progress on the sensitivity of WGM-resonator-based sensors. Now we have demonstrations of single-particle level detections of proteins, nucleic acids, and even atomic ions. Further research in WGM resonators may achieve even higher sensitivity (such as single hydrogen atom, perhaps), but from the perspective of chemical and bio-sensing, the sensitivity achieved today is already sufficient for most applications. What is lacking, however, is the robustness of the WGM sensor and its integration with peripheral devices that are needed for sensing.

Efficient yet robust coupling to WGM resonators is perhaps the greatest challenge to sensor stability and robustness. Tapered fiber couplers, which are still the most popular coupling scheme today, is mechanically too unstable and fragile for sensing applications. Other coupling schemes such as prism[4] or chaos-assisted tunneling[56] have already been shown to improve the robustness of coupling. Another method to improve the stability of coupling is to embed the resonator and fiber taper coupler in a polymer matrix,[168] but this method limits the accessibility of molecules to the resonator surface and is not well-suited for chemical and bio-sensing applications. I believe the most promising coupling scheme may be waveguide coupling to a WGM resonator made on the same chip, currently used for ring resonators. Today, ring resonators have limited Q-factor due to defects during fabrication, but as the fabrication technology improves, this may prove to be the most convenient platform for practical applications.

Efficient sample delivery for improved signal amplitude relative to the sensor's response to changing ambient conditions such as temperature and pressure poses another challenges. In terms of bio-sensing, the incorporation of a micro-fluidic system can be expected to speed up analyte delivery to the resonator, as well as maintaining a stable ambient environment for the resonator. The use of mesoporous silica resonator mentioned in the previous section, or other methods to concentrate the analyte of interest on the resonator, can improve the sample capturing ability of the resonator, and hence increase the intensity of the desired signal over "noise" that comes from the ambient environment.

Lastly, system integration with peripheral devices, such as lasers and photodetectors, is crucial for the use of WGM resonator sensors outside of laboratory environments. Today, an experiment with WGM resonator typically involves a tunable laser, photodiode, function generator,

oscilloscope or other data acquisition hardware, and various fiber components. Because of these peripheral devices, it is difficult to take the resonator outside of laboratory setting for applications that require mobility. A system that shrinks these peripheral devices onto a phone-sized platform has already been demonstrated,[169] which is highly promising for expanding WGM sensors for applications that were not possible previously. In the future, I envision a multiplexed array of WGM sensors, all controlled by a mobile system for light input and output. Such a system can work together as a sensor network, which provides much more data than a single resonator alone.

References

1. Vollmer, F. *et al.* Protein detection by optical shift of a resonant microcavity. *Appl. Phys. Lett.* **80,** 4057 (2002).

2. Vollmer, F., Arnold, S. & Keng, D. Single virus detection from the reactive shift of a whispering-gallery mode. *Proc. Natl. Acad. Sci. U. S. A.* **105,** 20701–4 (2008).

3. Dantham, V. R. *et al.* Label-free detection of single protein using a nanoplasmonic-photonic hybrid microcavity. *Nano Lett.* **13,** 3347–3351 (2013).

4. Baaske, M. D., Foreman, M. R. & Vollmer, F. Single-molecule nucleic acid interactions monitored on a label-free microcavity biosensor platform. *Nat. Nanotechnol.* **9,** 933–939 (2014).

5. Baaske, M. D. & Vollmer, F. Optical observation of single atomic ions interacting with plasmonic nanorods in aqueous solution. *Nat. Photonics* **10,** 733–739 (2016).

6. Vollmer, F. & Arnold, S. Whispering-gallery-mode biosensing: label-free detection down to single molecules. *Nat. Methods* **5,** 591–596 (2008).

7. Symes, R., Sayera, R. M. & Reid, J. P. Cavity enhanced droplet spectroscopy: Principles, perspectives and prospects. *Phys. Chem. Chem. Phys.* **6,** 474–487 (2004).

8. Yi, K. J., Wang, H., Lu, Y. F. & Yang, Z. Y. Enhanced Raman scattering by self-assembled silica spherical microparticles. *J. Appl. Phys.* **101,** (2007).

9. Mie, G. Beiträge zur Optik trüber Medien, speziell kolloidaler Metallösungen. *Ann. Phys.*

330, 377–445 (1908).

10. Gorodetsky, M., Savchenkov, A. & Ilchenko, V. Ultimate Q of optical microsphere resonators. *Opt. Lett.* **21,** 453–455 (1996).

11. Spillane, S. M. *et al.* Ultrahigh-Q toroidal microresonators for cavity quantum electrodynamics. *Phys. Rev. A - At. Mol. Opt. Phys.* **71,** 1–10 (2005).

12. Balac, S. & Féron, P. *Whispering gallery modes volume computation in optical micro-spheres*.

13. Chiasera, A. *et al.* Spherical whispering-gallery-mode microresonators. *Laser Photonics Rev.* **4,** 457–482 (2010).

14. Knight, J. C., Cheung, G., Jacques, F. & Birks, T. a. Phase-matched excitation of whispering-gallery-mode resonances by a fiber taper. *Opt. Lett.* **22,** 1129–31 (1997).

15. Ward, J. M. *et al.* Heat-and-pull rig for fiber taper fabrication. *Rev. Sci. Instrum.* **77,** 83105 (2006).

16. Spillane, S., Kippenberg, T., Painter, O. & Vahala, K. Ideality in a Fiber-Taper-Coupled Microresonator System for Application to Cavity Quantum Electrodynamics. *Phys. Rev. Lett.* **91,** 43902 (2003).

17. Huckabay, H. A. & Dunn, R. C. Whispering gallery mode imaging for the multiplexed detection of biomarkers. *Sensors Actuators, B Chem.* **160,** 1262–1267 (2011).

18. Lutti, J., Langbein, W. & Borri, P. High Q optical resonances of polystyrene microspheres in water controlled by optical tweezers. *Appl. Phys. Lett.* **91,** 141116 (2007).

19. Hanumegowda, N. M., Stica, C. J., Patel, B. C., White, I. & Fan, X. Refractometric sensors based on microsphere resonators. *Appl. Phys. Lett.* **87,** 201107 (2005).

20. Ilchenko, V. S., Yao, X. S. & Maleki, L. Pigtailing the high-Q microsphere cavity: a simple fiber coupler for optical whispering-gallery modes. *Opt. Lett.* **24,** 723–5 (1999).

21. Gorodetsky, M. L. & Ilchenko, V. S. Optical microsphere resonators: optimal coupling to high-Q whispering gallery modes. *J. Opt. Soc. Am. B* **16,** 147 (1999).

22. Ashkin, A. & Dziedzic, J. M. Observation of resonances in the radiation pressure on dielectric spheres. *Phys. Rev. Lett.* **38,** 1351–1354 (1977).

23. Ashkin, A. & Dziedzic, J. M. Observation of optical resonances of dielectric spheres by light scattering. *Appl. Opt.* **20,** 1803 (1981).

24. QIAN, S.-X., SNOW, J. B., TZENG, H.-M. & CHANG, R. K. Lasing Droplets: Highlighting the Liquid-Air Interface by Laser Emission. *Science (80-.).* **231,** 486–488 (1986).

25. Braginsky, V. B., Gorodetsky, M. L. & Ilchenko, V. S. Quality-factor and nonlinear properties of optical whispering-gallery modes. *Phys. Lett. A* **137,** 393–397 (1989).

26. Zhang, Q., Han, Y., Wang, W., Zhang, L. & Chang, J. Preparation of fluorescent polystyrene microspheres by gradual solvent evaporation method. *Eur. Polym. J.* **45,** 550–556 (2009).

27. Liu, N., Zhao, W. & Rong, J. CO_2 -driven synthesis of monodisperse barium titanate microspheres. *J. Am. Ceram. Soc.* 1–5 (2017). doi:10.1111/jace.15339

28. Lutti, J., Langbein, W. & Borri, P. A monolithic optical sensor based on whispering-gallery modes in polystyrene microspheres. *Appl. Phys. Lett.* **93,** 151103 (2008).

29. Armani, D. K., Kippenberg, T. J., Spillane, S. M. & Vahala, K. J. Ultra-high-Q toroid microcavity on a chip. *Nature* **421,** 925–928 (2003).

30. Jiang, X. *et al.* Chip-based silica microspheres for cavity optomechanics. *Opt. Express* **23,** 27260 (2015).

31. Jager, J.-B. *et al.* High-Q silica microcavities on a chip: From microtoroid to microsphere. *Appl. Phys. Lett.* **99,** 181123 (2011).

32. Kippenberg, T. J., Spillane, S. M., Min, B. & Vahala, K. J. Theoretical and experimental study of stimulated and cascaded Raman scattering in ultrahigh-Q optical microcavities. *IEEE J. Sel. Top. Quantum Electron.* **10,** 1219–1228 (2004).

33. Sumetsky, M. Whispering-gallery-bottle microcavities : the three-dimensional etalon. *Opt. Lett.* **29,** 8–10 (2004).

34. Louyer, Y., Meschede, D. & Rauschenbeutel, A. Tunable whispering-gallery-mode resonators for cavity quantum electrodynamics. *Phys. Rev. A* **72,** 31801 (2005).

35. Pöllinger, M., O'Shea, D., Warken, F. & Rauschenbeutel, A. Ultrahigh-Q Tunable Whispering-Gallery-Mode Microresonator. *Phys. Rev. Lett.* **103,** 53901 (2009).

36. Asano, M. *et al.* Observation of optomechanical coupling in a microbottle resonator. *Laser Photonics Rev.* **10,** 603–611 (2016).

37. Grimaldi, I. A. *et al.* Polymer based planar coupling of self-assembled bottle

microresonators. *Appl. Phys. Lett.* **105,** 2012–2016 (2014).

38. Luchansky, M. S. *et al.* Characterization of the evanescent field profile and bound mass sensitivity of a label-free silicon photonic microring resonator biosensing platform. *Biosens. Bioelectron.* **26,** 1283–1291 (2010).

39. Iqbal, M., Gleeson, M. & Spaugh, B. Label-free biosensor arrays based on silicon ring resonators and high-speed optical scanning instrumentation. *IEEE J. Sel. Top. Quantum Electron.* **16,** 654–661 (2010).

40. Qavi, A. J. & Bailey, R. C. Multiplexed detection and label-free quantitation of microRNAs using arrays of silicon photonic microring resonators. *Angew. Chemie - Int. Ed.* **49,** 4608–4611 (2010).

41. White, I. M., Oveys, H. & Fan, X. Liquid-core optical ring-resonator sensors. *Opt. Lett.* **31,** 1319–21 (2006).

42. Yang, G., White, I. M. & Fan, X. An opto-fluidic ring resonator biosensor for the detection of organophosphorus pesticides. *Sensors Actuators, B Chem.* **133,** 105–112 (2008).

43. Watkins, A., Ward, J., Wu, Y. & Chormaic, S. N. Single-input spherical microbubble resonator. *Opt. Lett.* **36,** 2113–5 (2011).

44. Lee, H. *et al.* Chemically etched ultrahigh-Q wedge-resonator on a silicon chip. *Nat. Photonics* **6,** 369–373 (2012).

45. Yang, K. Y. *et al.* Broadband dispersion-engineered microresonator on a chip. *Nat.*

Photonics **10,** 316–320 (2016).

46. Yang, Q. F., Yi, X., Yang, K. Y. & Vahala, K. Counter-propagating solitons in microresonators. *Nat. Photonics* **11,** 560–564 (2017).

47. Arnold, S., Khoshsima, M., Teraoka, I., Holler, S. & Vollmer, F. Shift of whispering-gallery modes in microspheres by protein adsorption. *Opt. Lett.* **28,** 272–274 (2003).

48. Teraoka, I., Arnold, S. & Vollmer, F. Perturbation approach to resonance shifts of whispering-gallery modes in a dielectric microsphere as a probe of a surrounding medium. *J. Opt. Soc. Am. B* **20,** 1937 (2003).

49. Kim, E., Baaske, M. D. & Vollmer, F. Towards next-generation label-free biosensors: recent advances in whispering gallery mode sensors. *Lab Chip* **17,** 1190–1205 (2017).

50. Zhu, J. *et al.* On-chip single nanoparticle detection and sizing by mode splitting in an ultrahigh-Q microresonator. *Nat. Photonics* **4,** 46–49 (2009).

51. Zhu, J., Özdemir, Ş. K. Ş., He, L., Chen, D. D.-R. & Yang, L. Single virus and nanoparticle size spectrometry by whispering-gallery-mode microcavities. *Opt. Express* **19,** 16195–206 (2011).

52. He, L. *et al.* Statistics of multiple-scatterer-induced frequency splitting in whispering gallery microresonators and microlasers. *New J. Phys.* **15,** 73030 (2013).

53. Kim, W., Özdemir, S. K., Zhu, J. & Yang, L. Observation and characterization of mode splitting in microsphere resonators in aquatic environment. *Appl. Phys. Lett.* **98,** 141106 (2011).

54. Kim, W., Özdemir, Ŝ. K., Zhu, J., He, L. & Yang, L. Demonstration of mode splitting in an optical microcavity in aqueous environment. *Appl. Phys. Lett.* **97,** (2010).

55. Hu, Y. *et al.* Mode broadening induced by nanoparticles in an optical whispering-gallery microcavity. *Phys. Rev. A - At. Mol. Opt. Phys.* **90,** (2014).

56. Shao, L. *et al.* Detection of single nanoparticles and lentiviruses using microcavity resonance broadening. *Adv. Mater.* **25,** 5616–5620 (2013).

57. Betzig, E. & Chichester, R. J. Single Molecules Observed by Near-Field Scanning Optical Microscopy. *Science (80-.).* **262,** 1422–1425 (1993).

58. Shamah, S. M. & Cunningham, B. T. Label-free cell-based assays using photonic crystal optical biosensors. *Analyst* **136,** 1090–102 (2011).

59. Waters, J. C. Accuracy and precision in quantitative fluorescence microscopy. *J. Cell Biol.* **185,** 1135–1148 (2009).

60. Fan, X. *et al.* Sensitive optical biosensors for unlabeled targets: A review. *Anal. Chim. Acta* **620,** 8–26 (2008).

61. Hunt, H. K. & Armani, A. M. Label-free biological and chemical sensors. *Nanoscale* **2,** 1544–1559 (2010).

62. Luchansky, M. S. & Bailey, R. C. High-Q optical sensors for chemical and biological analysis. *Anal. Chem.* **84,** 793–821 (2012).

63. Vollmer, F. & Yang, L. Label-free detection with high-Q microcavities: a review of biosensing mechanisms for integrated devices. *Nanophotonics* **1,** 267–291 (2012).

64. Heylman, K. D. *et al.* Optical microresonators as single-particle absorption spectrometers. *Nat. Photonics* **10,** 788–795 (2016).

65. Su, J., Goldberg, A. F. & Stoltz, B. M. Label-free detection of single nanoparticles and biological molecules using microtoroid optical resonators. *Light Sci. Appl.* **5,** e16001 (2016).

66. Topolancik, J. & Vollmer, F. Photoinduced transformations in bacteriorhodopsin membrane monitored with optical microcavities. *Biophys. J.* **92,** 2223–9 (2007).

67. Foreman, M. R. & Vollmer, F. Optical tracking of anomalous diffusion kinetics in polymer microspheres. *Phys. Rev. Lett.* **114,** (2015).

68. Schägger, H. & von Jagow, G. Tricine-sodium dodecyl sulfate-polyacrylamide gel electrophoresis for the separation of proteins in the range from 1 to 100 kDa. *Anal. Biochem.* **166,** 368–379 (1987).

69. Sutar, P. B., Mishra, R. K., Pal, K. & Banthia, A. K. Development of pH sensitive polyacrylamide grafted pectin hydrogel for controlled drug delivery system. *J. Mater. Sci. Mater. Med.* **19,** 2247–2253 (2008).

70. Yang, T.-H. Recent Applications of Polyacrylamide as Biomaterials. *Recent Patents Mater. Sci.* **1,** 29–40 (2008).

71. Lee, D. C. *et al.* Monitoring plasma processing steps with a sensitive Western blot assay for the detection of the prion protein. *J. Virol. Methods* **84,** 77–89 (2000).

72. Wallis, R. S., Amir-Tahmasseb, M. & Ellner, J. J. Induction of interleukin 1 and tumor

necrosis factor by mycobacterial proteins: the monocyte western blot. *Proc. Natl. Acad. Sci. U. S. A.* **87,** 3348–52 (1990).

73. Ashley, G. W., Henise, J., Reid, R. & Santi, D. V. Hydrogel drug delivery system with predictable and tunable drug release and degradation rates. *Proc. Natl. Acad. Sci. U. S. A.* **110,** 2318–23 (2013).

74. Bhattarai, N., Gunn, J. & Zhang, M. Chitosan-based hydrogels for controlled, localized drug delivery. *Adv. Drug Deliv. Rev.* **62,** 83–99 (2010).

75. Peppas, N. A., Keys, K. B., Torres-Lugo, M. & Lowman, A. M. Poly(ethylene glycol)-containing hydrogels in drug delivery. *J. Control. Release* **62,** 81–87 (1999).

76. Zustiak, S. P. & Leach, J. B. Characterization of protein release from hydrolytically degradable poly(ethylene glycol) hydrogels. *Biotechnol. Bioeng.* **108,** 197–206 (2011).

77. Koyano, T., Minoura, N., Nagura, M. & Kobayashi, K. I. Attachment and growth of cultured fibroblast cells on PVA/chitosan- blended hydrogels. *J. Biomed. Mater. Res.* **39,** 486–490 (1998).

78. Tibbitt, M. W. & Anseth, K. S. Hydrogels as extracellular matrix mimics for 3D cell culture. *Biotechnol. Bioeng.* **103,** 655–663 (2009).

79. Von Recum, H. A. *et al.* Novel thermally reversible hydrogel as detachable cell culture substrate. *J. Biomed. Mater. Res.* **40,** 631–639 (1998).

80. Zustiak, S., Nossal, R. & Sackett, D. L. Multiwell stiffness assay for the study of cell responsiveness to cytotoxic drugs. *Biotechnol. Bioeng.* **111,** 396–403 (2014).

81. Mi, F. L., Kuan, C. Y., Shyu, S. S., Lee, S. T. & Chang, S. F. Study of gelation kinetics and chain-relaxation properties of glutaraldehyde-cross-linked chitosan gel and their effects on microspheres preparation and drug release. *Carbohydr. Polym.* **41,** 389–396 (2000).

82. Eaton, W. A., Hofrichter, J., Ross, P. D., Tschudin, R. G. & Becker, E. D. Comparison of sickle cell hemoglobin gelation kinetics measured by NMR and optical methods. *Biochem. Biophys. Res. Commun.* **69,** 538–547 (1976).

83. Mathur, A. M. & Scranton, A. B. Characterization of hydrogels using nuclear magnetic resonance spectroscopy. *Biomaterials* **17,** 547–557 (1996).

84. Acton, J. C., Hanna, M. A. & Satterlee, L. D. Heat-induced gelation and protein-protein interaction of actomyosin. *J. Food Biochem.* **5,** 101–113 (1981).

85. Coffmann, C. W. & Garcia, V. V. Functional properties and amino acid content of a protein isolate from mung bean flour. *J. Fd Technol.* **12,** 473–484 (1977).

86. Hvidt, S., Joergensen, E. B., Brown, W. & Schillen, K. Micellization and Gelation of Aqueous Solutions of a Triblock Copolymer Studied by Rheological Techniques and Scanning Calorimetry. *J. Phys. Chem.* **98,** 12320–12328 (1994).

87. Cheetham, N. W. H. & Mashimba, E. N. M. Conformational aspects of xanthan—Galactomannan gelation. Further evidence from optical-rotation studies. *Carbohydr. Polym.* **14,** 17–27 (1990).

88. Norisuye, T., Strybulevych, A., Scanlon, M. & Page, J. Ultrasonic investigation of the gelation process of poly(acrylamide) gels. *Macromol. Symp.* **242,** 208–215 (2006).

89. Djabourov, M. *et al.* Gelation of aqueous gelatin solutions . I . Structural investigation To cite this version : Gelation of aqueous investigation. *J. Phys.* **49,** 319–332 (1988).

90. Higham, A. K., Bonino, C. A., Raghavan, S. R. & Khan, S. A. Photo-activated ionic gelation of alginate hydrogel: real-time rheological monitoring of the two-step crosslinking mechanism. *Soft Matter* **10,** 4990 (2014).

91. Tung, C.-Y. M. & Dynes, P. J. Relationship between viscoelastic properties and gelation in thermosetting systems. *J. Appl. Polym. Sci.* **27,** 569–574 (1982).

92. Schultz, K. M., Baldwin, A. D., Kiick, K. L. & Furst, E. M. Gelation of Covalently Cross-Linked PEG−Heparin Hydrogels. *Macromolecules* **42,** 5310–5316 (2009).

93. Kizilay, M. Y. & Okay, O. Effect of initial monomer concentration on spatial inhomogeneity in poly(acrylamide) gels. *Macromolecules* **36,** 6856–6862 (2003).

94. Nemova, G. & Kashyap, R. Silica Bottle Resonator Sensor for Refractive Index and Temperature Measurements. *Sensors* **16,** 87 (2016).

95. Larsson, P.-O. & Mosbach, K. Immobilization of steroid-transforming microorganisms in polyacrylamide. *Methods Enzymol.* **44,** 183–190 (1976).

96. Armani, A. M., Armani, D. K., Min, B., Vahala, K. J. & Spillane, S. M. Ultra-high-Q microcavity operation in H 2O and D 2O. *Appl. Phys. Lett.* **87,** 1–3 (2005).

97. Buggy, S. J., Chehura, E., James, S. W. & Tatam, R. P. Optical fibre grating refractometers for resin cure monitoring. *J. Opt. A Pure Appl. Opt.* **9,** S60 (2007).

98. Zhang, B., Wang, D., Du, S. & Song, Y. An investigation of a fiber optic sensor in the

composite cure process. *Smart Mater. Struct.* **8,** 515–518 (1999).

99. Luo, Y. & Wang, Q. Zein-based micro- and nano-particles for drug and nutrient delivery: A review. *J. Appl. Polym. Sci.* **131,** n/a-n/a (2014).

100. Weng, L., Zhou, X., Zhang, X., Xu, J. & Zhang, L. In situ monitoring gelation process of N,N-dimethylacrylamide by refractive index technique. *Polymer (Guildf).* **43,** 6761–6765 (2002).

101. MacHavaram, V. R. *et al.* Multi-point monitoring of cross-linking reactions. *J. Appl. Polym. Sci.* **131,** 1–11 (2014).

102. Garner, B. W., Cai, T., Ghosh, S., Hu, Z. & Neogi, A. Refractive Index Change Due to Volume-Phase Transition in Polyacrylamide Gel Nanospheres for Optoelectronics and Bio-photonics. *Appl. Phys. Express* **2,** 57001 (2009).

103. Li, B. B. *et al.* On chip, high-sensitivity thermal sensor based on high- Q polydimethylsiloxane-coated microresonator. *Appl. Phys. Lett.* **96,** 251109 (2010).

104. Li, B. B. *et al.* Experimental observation of Fano resonance in a single whispering-gallery microresonator. *Appl. Phys. Lett.* **98,** (2011).

105. Wang, Y. *et al.* Coupled-mode induced transparency in a bottle whispering-gallery-mode resonator. *Opt. Lett.* **41,** 1825 (2016).

106. Calvet, D., Wong, J. Y. & Giasson, S. Rheological monitoring of polyacrylamide gelation: Importance of cross-link density and temperature. *Macromolecules* **37,** 7762–7771 (2004).

107. Giordano, M. *et al.* A fiber optic thermoset cure monitoring sensor. *Polym. Compos.* **21,**

523–530 (2000).

108. Kim, Y. H. *et al.* Thermo-optic coefficient measurement of liquids based on simultaneous temperature and refractive index sensing capability of a two-mode fiber interferometric probe. *Opt. Express* **20,** 23744 (2012).

109. Denisin, A. K. & Pruitt, B. L. Tuning the Range of Polyacrylamide Gel Stiffness for Mechanobiology Applications. *ACS Appl. Mater. Interfaces* **8,** 21893–21902 (2016).

110. Wen, J. H. *et al.* Interplay of matrix stiffness and protein tethering in stem cell differentiation. *Nat. Mater.* **13,** 979–987 (2014).

111. Kjøniksen, A.-L. & Nyström, B. Effects of polymer concentration and cross-linking density on rheology of chemically cross-linked poly (vinyl alcohol) near the gelation threshold. *Macromolecules* **29,** 5215–5222 (1996).

112. Naghash, H. J. & Okay, O. Formation and structure of polyacrylamide gels. *J. Appl. Polym. Sci.* **60,** 971–979 (1996).

113. Solon, J., Levental, I., Sengupta, K., Georges, P. C. & Janmey, P. A. Fibroblast adaptation and stiffness matching to soft elastic substrates. *Biophys. J.* **93,** 4453–4461 (2007).

114. Stiles, P. L., Dieringer, J. A., Shah, N. C. & Van Duyne, R. P. Surface-Enhanced Raman Spectroscopy. *Annu. Rev. Anal. Chem.* **1,** 601–626 (2008).

115. He, L., Ozdemir, S. K., Zhu, J., Kim, W. & Yang, L. Detecting single viruses and nanoparticles using whispering gallery microlasers. *Nat. Nanotechnol.* **6,** 428–32 (2011).

116. Baaske, M. D. & Vollmer, F. Optical observation of single atomic ions interacting with

plasmonic nanorods in aqueous solution. *Nat. Photonics* **10,** 733–739 (2016).

117. Ding, S.-Y. *et al.* Nanostructure-based plasmon-enhanced Raman spectroscopy for surface analysis of materials. *Nat. Rev. Mater.* **1,** 16021 (2016).

118. Le Ru, E. C., Blackie, E., Meyer, M. & Etchegoint, P. G. Surface enhanced raman scattering enhancement factors: A comprehensive study. *J. Phys. Chem. C* **111,** 13794–13803 (2007).

119. Stiles, P. L., Dieringer, J. A., Shah, N. C. & Van Duyne, R. P. Surface-Enhanced Raman Spectroscopy. *Annu. Rev. Anal. Chem.* **1,** 601–626 (2008).

120. Alessandri, I. & Lombardi, J. R. Enhanced Raman Scattering with Dielectrics. *Chem. Rev.* **116,** 14921–14981 (2016).

121. Caldarola, M. *et al.* Non-plasmonic nanoantennas for surface enhanced spectroscopies with ultra-low heat conversion. *Nat. Commun.* **6,** 7915 (2015).

122. Dantham, V. R., Bisht, P. B. & Namboodiri, C. K. R. Enhancement of Raman scattering by two orders of magnitude using photonic nanojet of a microsphere. *J. Appl. Phys.* **109,** 103103 (2011).

123. Alessandri, I. Enhancing Raman scattering without plasmons: unprecedented sensitivity achieved by TiO2 shell-based resonators. *J. Am. Chem. Soc.* **135,** 5541–4 (2013).

124. Alessandri, I., Bontempi, N. & Depero, L. E. Colloidal lenses as universal Raman scattering enhancers. *RSC Adv.* **4,** 38152–38158 (2014).

125. Yi, K. J., Wang, H., Lu, Y. F. & Yang, Z. Y. Enhanced Raman scattering by self-

assembled silica spherical microparticles. *J. Appl. Phys.* **101,** 63528 (2007).

126. Du, C. L., Kasim, J., You, Y. M., Shi, D. N. & Shen, Z. X. Enhancement of Raman scattering by individual dielectric microspheres. *J. Raman Spectrosc.* **42,** 145–148 (2011).

127. Anderson, M. S. Nonplasmonic surface enhanced Raman spectroscopy using silica microspheres. *Appl. Phys. Lett.* **97,** 131116 (2010).

128. Bontempi, N., Carletti, L., De Angelis, C. & Alessandri, I. Plasmon-free SERS detection of environmental CO 2 on TiO 2 surfaces. *Nanoscale* **8,** 3226–3231 (2016).

129. Qi, D., Lu, L., Wang, L. & Zhang, J. Improved SERS Sensitivity on Plasmon-Free TiO_2 Photonic Microarray by Enhancing Light-Matter Coupling. *J. Am. Chem. Soc.* **136,** 9886–9889 (2014).

130. Yan, Y. *et al.* Self-assembled dielectric microsphere array enhanced Raman scattering for large-area and ultra-long working distance confocal detection. *Opt. Express* **23,** 25854 (2015).

131. Yang, L. *et al.* Observation of Enhanced Raman Scattering for Molecules Adsorbed on TiO_2 Nanoparticles: Charge-Transfer Contribution. *J. Phys. Chem. C* **112,** 20095–20098 (2008).

132. Wang, Y. *et al.* Direct observation of surface-enhanced Raman scattering in ZnO nanocrystals. *J. Raman Spectrosc.* **40,** 1072–1077 (2009).

133. Evans, C. C., Liu, C. & Suntivich, J. TiO2 Nanophotonic Sensors for Efficient Integrated Evanescent Raman Spectroscopy. *ACS Photonics* **3,** 1662–1669 (2016).

134. Murgida, D. H. & Hildebrandt, P. Disentangling interfacial redox processes of proteins by SERR spectroscopy. *Chem. Soc. Rev.* **37,** 937–945 (2008).

135. Mahmoudi, M. *et al.* Variation of protein corona composition of gold nanoparticles following plasmonic heating. *Nano Lett.* **14,** 6–12 (2014).

136. Ward, D. R., Corley, D. A., Tour, J. M. & Natelson, D. Vibrational and electronic heating in nanoscale junctions. *Nat. Nanotechnol.* **6,** 33–38 (2010).

137. Kuhlicke, A., Schietinger, S., Matyssek, C., Busch, K. & Benson, O. In situ observation of plasmon tuning in a single gold nanoparticle during controlled melting. *Nano Lett.* **13,** 2041–2046 (2013).

138. Ausman, L. K. & Schatz, G. C. Whispering-gallery mode resonators: Surface enhanced Raman scattering without plasmons. *J. Chem. Phys.* **129,** 54704 (2008).

139. Liu, R.-S., Jin, W.-L., Yu, X.-C., Liu, Y.-C. & Xiao, Y.-F. Enhanced Raman scattering of single nanoparticles in a high-Q whispering-gallery microresonator. *Phys. Rev. A* **91,** 1–6 (2015).

140. Cai, M. & Vahala, K. Highly efficient optical power transfer to whispering-gallery modes by use of a symmetrical dual-coupling configuration. *Opt. Lett.* **25,** 260–262 (2000).

141. Özdemir, Ş. K. *et al.* Highly sensitive detection of nanoparticles with a self-referenced and self-heterodyned whispering-gallery Raman microlaser. *Proc. Natl. Acad. Sci. U. S. A.* **111,** E3836-44 (2014).

142. Tomes, M. & Carmon, T. Photonic micro-electromechanical systems vibrating at X-band

(11-GHz) rates. *Phys. Rev. Lett.* **102,** (2009).

143. Carmon, T., Yang, L. & Vahala, K. J. Dynamical thermal behavior and thermal self-stability of microcavities. *Opt. Express* **12,** 4742 (2004).

144. Gorodetsky, M. L. & Ilchenko, V. S. Optical microsphere resonators: optimal coupling to high-Q whispering-gallery modes. *J. Opt. Soc. Am. B* **16,** 147 (1999).

145. Checoury, X., Han, Z., El Kurdi, M. & Boucaud, P. Deterministic measurement of the Purcell factor in microcavities through Raman emission. *Phys. Rev. A - At. Mol. Opt. Phys.* **81,** 33832 (2010).

146. Petrak, B., Djeu, N. & Muller, A. Purcell-enhanced Raman scattering from atmospheric gases in a high-finesse microcavity. *Phys. Rev. A - At. Mol. Opt. Phys.* **89,** 1–6 (2014).

147. Kaupp, H. *et al.* Scaling laws of the cavity enhancement for nitrogen-vacancy centers in diamond. *Phys. Rev. A - At. Mol. Opt. Phys.* **88,** 53812 (2013).

148. Hümmer, T. *et al.* Cavity-enhanced Raman Microscopy of Individual Carbon Nanotubes. *Nat. Commun.* **7,** 1–7 (2016).

149. Ru, E. L. & Etchegoin, P. *Principles of Surface-Enhanced Raman Spectroscopy: and Related Plasmonic Effects*. (Elsevier Science, 2008).

150. Balac, S. & Féron, P. *Whispering gallery modes volume computation in optical micro-spheres*. [Research Report] FOTON, UMR CNRS 6082. (2014).

151. Özdemir, Ş. K., Zhu, J., He, L. & Yang, L. Estimation of Purcell factor from mode-splitting spectra in an optical microcavity. *Phys. Rev. A - At. Mol. Opt. Phys.* **83,** (2011).

152. Pelton, M. Modified spontaneous emission in nanophotonic structures. *Nat. Photonics* **9,** 427–435 (2015).

153. Scully, M. & Zubairy, M. S. *Quantum Optics*. (Cambridge University Press, 1997).

154. Darby, B. L., Etchegoin, P. G. & Le Ru, E. C. Single-molecule surface-enhanced Raman spectroscopy with nanowatt excitation. *Phys. Chem. Chem. Phys.* **16,** 23895–23899 (2014).

155. Etchegoin, P. G., Le Ru, E. C. & Meyer, M. Evidence of natural isotopic distribution from single-molecule SERS. *J. Am. Chem. Soc.* **131,** 2713–2716 (2009).

156. Stein, A., Melde, B. J. & Schroden, R. C. Hybrid Inorganic-Organic Mesoporous Silicates—Nanoscopic Reactors Coming of Age. *Adv. Mater.* **12,** 1403–1419 (2000).

157. Wan, Y. & Zhao, D. On the controllable soft-templating approach to mesoporous silicates. *Chem. Rev.* **107,** 2821–2860 (2007).

158. Zhao, D., Huo, Q., Feng, J., Chmelka, B. F. & Stucky, G. D. Nonionic triblock and star diblock copolymer and oligomeric sufactant syntheses of highly ordered, hydrothermally stable, mesoporous silica structures. *J. Am. Chem. Soc.* **120,** 6024–6036 (1998).

159. Kresge, C. T., Leonowicz, M. E., Roth, W. J., Vartuli, J. C. & Beck, J. S. Ordered mesoporous molecular sieves synthesized by a liquid-crystal template mechanism. *Nature* **359,** 710–712 (1992).

160. Xu, P., Chen, C. & Li, X. Mesoporous-silica nanofluidic channels for quick enrichment/extraction of trace pesticide molecules. *Sci. Rep.* **5,** 17171 (2015).

161. Vallet-Regí, M., Balas, F. & Arcos, D. Mesoporous materials for drug delivery. *Angew. Chemie - Int. Ed.* **46,** 7548–7558 (2007).

162. Wirnsberger, G., Scott, B. J. & Stucky, G. D. pH Sensing with mesoporous thin films. *Chem. Commun.* 119–120 (2001).

163. Yang, P. *et al.* Mirrorless lasing from mesostructured waveguides patterned by soft lithography. *Science (80-.).* **287,** 465–467 (2000).

164. Scott, B. J., Wirnsberger, G. & Stucky, G. D. Mesoporous and mesostructured materials for optical applications. *Chem. Mater.* **13,** 3140–3150 (2001).

165. Scott, B. J., Wirnsberger, G., McGehee, M. D., Chmelka, B. F. & Stucky, G. D. Dye-doped mesostructured silica as a distributed feedback laser fabricated by soft lithography. *Adv. Mater.* **13,** 1231–1234 (2001).

166. Alberius, P. C. A. *et al.* General predictive syntheses of cubic, hexagonal, and lamellar silica and titania mesostructured thin films. *Chem. Mater.* **14,** 3284–3294 (2002).

167. Wang, G. *et al.* Functionalized mesoporous materials for adsorption and release of different drug molecules: A comparative study. *J. Solid State Chem.* **182,** 1649–1660 (2009).

168. Zhao, G. *et al.* Raman lasing and Fano lineshapes in a packaged fiber-coupled whispering-gallery-mode microresonator. *Sci. Bull.* **62,** 875–878 (2017).

169. Xu, X., Jiang, X., Zhao, G. & Yang, L. Phone-sized whispering-gallery microresonator sensing system. *Opt. Express* **24,** 25905 (2016).